THE UNIVERSITY OF CHICAGO

CIRCUIT QUANTUM ELECTRODYNAMICS WITH ELECTRONS ON HELIUM

A DISSERTATION SUBMITTED TO
THE FACULTY OF THE DIVISION OF THE THE PHYSICAL SCIENCES
IN CANDIDACY FOR THE DEGREE OF
DOCTOR OF PHILOSOPHY

DEPARTMENT OF PHYSICS

BY
GE YANG

CHICAGO, ILLINOIS
MARCH 2020

To my parents, and those who passed by.

He was ambitious. And it was a good thing.

– Richard Sutton[1]

[1] private conversation, in reference to Eric Kendal.

TABLE OF CONTENTS

LIST OF FIGURES

ACKNOWLEDGMENTS

The journey that is partially covered by this thesis first started with just Dave and I. Then many others joined. This experience would not have been the same without the dedication and meticulous work from my labmate Gerwin Koolstra. I want to thank him for our friendship, for the team work, for all of the stroopwafels and beer, for the war we fought together, for the stress we endured, and for those sleepless nights amist the mesmerizing noise from the pulse tube. And thanks for always pointing out the typos I make–I'm sure you will find plenty, in this very thesis.

I also want to thank all of the people I have worked with. Seven years is a long time. When I first arrived in Chicago on the 3rd of January 2011, I didn't expect to meet so many kind people who dedicate their life to either the pursuit of science or the support of it. Here I want to thank everyone at the Argonne National Lab Center for Nano-materials. I think of your faces from time to time. There were those car rides from David and Leo, the "walk-of-shame" from Valentina, the babbling from Susane (which is not her legal name), and the perpetually stern look that Ralu wears. I feel privileged to have had those illuminating conversations, under the yellow light.

Most of our samples where fabricated at Argonne, a place that became my second home. As those emails about an expired security clearance die down, we moved our production to the Pfieffer Nano-fabrication Facility on the University of Chicago campus. I also want to thank Peter, Anna, Jung-woo and the rest of the crew. Your lively support gave me a home closer to home, a place where ideas attain their physicality.

I also want to thank the rest of my lab. You are truly an exceptional bunch. As an older (but not wiser) member of the Schuster's circuit, I witnessed in awe over the years of your productivity and brilliance. I am reminded daily of how much I still need to learn. Thank you for the inspiration and companionship.

Thanks Dave and Heather, for starting this out with me, for tolerating my mischief's

over the years, and for the push on the back when I needed it the most.

Finally, I want to thank my parents – for indulging my wander and not visiting home for the better half of the last decade. And to those who I have loved. The memory of you that I carry, gives me strength.

ABSTRACT

The quest towards precise measurement and control of quantum mechanical systems is behind many if not most of the advances in mesoscopic physics in the recent years.

This thesis follows that tradition, and describes the first realization of a hybrid circuit integrating electrons on helium (EonHe) with the circuit quantum electrodynamics (cQED) architecture. In this hybrid architecture, the quantized lateral motion of the electrons strongly couples with the transverse electric field inside a high-Q superconducting resonator, enabling sensitive detection and manipulation of the electron's in-plane motion degree of freedom. Such architecture also provide a plausible road map towards using the spin degrees of freedom of the electrons as a quantum memory.

Our hope is to establish a novel model system for quantum control and manipulation, where the uncanny similarity between the electron Hamiltonian and the strong coulomb interactions could give rise to unparalleled rich quantum phenomena. In our first experiment towards this goal, we demonstrate strong dispersive coupling between $\sim 10^5$ electrons and a superconducting co-planar waveguide resonator.

The effort of the second experiment focuses on bringing down this number to just a few electrons in an isolated trap. We replace the CPW resonator with a quarter-wavelength strip-line resonator with one side terminated by a short ("the tuning fork"). This design changes the microwave mode that is visible to the electron dipole interaction, improves the coupling strength, and opens up the geometry for more sophisticated DC controls isolating an individual electron.

The third experiment implements such DC control scheme, and manages to trap just a single electron in a small trap. This small electron trap is defined by multiple DC electrodes near the open-end of the tuning fork. The overall circuit design resembles those seen in the quantum dot community. Much effort was spent on hitting the tight space between the dispersive constraints of the cQED measurement scheme and the increasing complication of

the sample. Single or few electron spectra are measured, and we provided an upper estimate on the acoustically broadened electron linewidth, together with design changes that reduce the linewidth of the electron states.

CHAPTER 1

INTRODUCTION

Precise measurement and control of quantum mechanical systems has been the driving force behind advances in mesoscopic physics. At it's core, such control is enabled by strong coupling between the quantum mechanical system and a clean electromagnetic environment, usually in the form of a high quality factor (high-Q) cavity. The coherent phase information of the hybridized system could be read out with high fidelity via the emitted photon. The same process in reverse provides a strong handle on manipulating the state itself. Engineering simple quantum mechanical systems and its isolation from the noise environment, yet still achieving strong coupling with the measurement channel, is key.

Over the years, various such systems have been developed using either fundamental particles, or condensed matter ensembles. Amongst the former there are the earlier single atom in the cavity experiments, molecular nuclear magnetic resonance (NMR) quantum computers, and cold ions in ion traps. Amongst the latter there are silicon spin qubits, semiconductor quantum dots, diamond NV centers, and solid state superconducting qubits. These systems have demonstrated impressive controllability, and has enabled higher level quantum optics, quantum information and precision measurement experiments. The very fine sensitivity of the quantum systems towards signals in the environment enabled such systems in finding a variety of applications in timing and sensing.

When a mesoscopic number of such simple building blocks are assembled, the engineered condensed-matter ensemble are useful as quantum simulators. Notable examples include superconducting qubit lattices, slow light, and time crystal.

With these impact in mind, we set out to engineer one such quantum mechanical systems with electrons floating on the surface of superfliud helium, inside micro-channels patterned into a superconducting microwave device. We take inspirations from techniques developed in aforementioned systems, especially circuit QED and semi-conductor quantum dot, in

addition to the long and rich history of electrons on helium physics. In this introductory chapter, we will lay down these motivations in detail together with a road map. The goal is to survey the excellent properties of such hybrid architecture that could allow us to avoid the experimental difficulties encountered in other systems, and sketch out the general design of this hybrid architecture.

1.1 The Making of A Qubit

The history of modern atomic and condensed matter physics is full of parallels. The making and remaking of qubits in various different subfield is a history of application of the same physics upon different physical systems. Under this context, we could take a look at the makings of the first atomic cavity QED system. This series of work span a period of over four decades.

A water-shed moment in modern atomic physics is the invention of maser (1953), and (optical) lasers (1960). The key ingredient that made maser and lasers possible was the introduction of a high-finesse cavity. In-part inspired by Purcell's much earlier work, it was already understood at that time that a cavity is crucial in achieving the gain required for lasing.

This development is significant for two reasons: First, it established empirically the importance of a high-finesse cavity in increasing the interaction strength between atoms and cavity modes, leading to larger cooperativity despite of the small atomic dipole moment. Secondly, it provided a crucial apparatus in coherent probing and manipulation of atomic systems. It is the low-phase-noise signal generator that atomic physicists need.

It took roughly another decade or two for the laser spectroscopy and optical pumping techniques to mature. Atomic lasers have limited tuning range. It wasn't until the late 70's and the early 80's when solid state semiconductor lasers championed by Carl Wieman saw wider adoption, enabling much greater flexibility and tunability and vastly simplified

construction.

Around the same time, Haroche and colleagues set about to construct a single-atomic laser, where the large number of atoms typically involved in the lasing phenomena is reduced to one. This regime where a single atom is coupled to a cavity causing the cavity spectrum to shift near the atomic absorption line, became known as the strong coupling regime. And it is this "Holy Grail" (in Haroche's own words) that led to the first atomic qubit. The physics that studies the coupled quantum mechanical system became known as cavity quantum electrodynamics, or cavity QED.

A significant amount of effort in Haroche's experiment was spent on the development of a high Q cavity. In this case, history is amazingly parallel as the same fundamental physics later gets implemented in various different systems. Haroche's Q breakthrough benefited from the work his colleagues were doing at the French Atomic Energy Commission(CEA), who were trying to use superconducting Nb cavities to construct much more powerful particle accelerators. Thirty years later, during the development of the cooper-pair box qubits in the Schoelkopf lab at Yale, it was the addition of a high-Q superconducting resonator and the cavity-enhanced coupling that led to the break-through in qubit life-time. In another few years, Haroche's cavity would be re-introduced–the same highly polished superconducting Niobium microwave cavity (plus high-purity aluminum ones) are now called 3D cavities for 3D qubits.

The development of an atomic qubit hence went through these four major steps:

1. understanding the atom (or the cooper-pair box in solid-state quantum computing)

2. development of the instrumentation necessary for probing the atom

3. observing ensemble-induced dispersive shift

4. reach strong coupling with just one.

1.2 Cavity QED with Electrons On Helium: A Quick Sketch

Inspired by the steps that led to the first atomic qubits, and the rich physics exhibited by the circuit-QED with superconducting qubits, we set out to build a new type of quantum system where single electrons floating on the surface of super-fluid helium acts as the qubits, coupled to and controlled by a high-finesse superconducting planar wave-guide cavity.

In this section, I will motivate this particular choice of condensed-matter system, and describe our general strategy in building an electrons on helium qubit.

1.2.1 Electron Ensembles on the Surface of Helium

When sprayed onto the surface of super-fluid helium, electrons gets trapped to the interface between the super-fluid helium and the vacuum above by its image charge inside the bulk helium. The helium's polarizability is only about 5.7% larger than that of vacuum, so the induced image charge is quite small. On the other hand, Pauli's exclusion principle prevents the electron from entering the helium bath. In the end, the electrons get trapped in a weak $1/r$ potential that is normal to the helium/vacuum interface, and form states that are similar to those of a Rydberg atom, levitated well above the helium surface ($\sim 8\,\mathrm{nm}$). The energy transition is typically in the 150 GHz range.

Vapor pressure of helium is negligible when $T < 1.2\,\mathrm{K}$. Our experiments are done inside a dry fridge at 20 - 500 mK. At this temperature, there won't be any interaction between the electrons and helium gas in the vacuum. Primary loss of the electron motional state would be due to coupling with ripplons, phonons, and most importantly, charge dipole coupling between the electron and lossy DC control electrodes. For detailed discussion of relevant properties of superfluid helium and electrons on helium, refer to chapter [placeholder EonHe chapter]

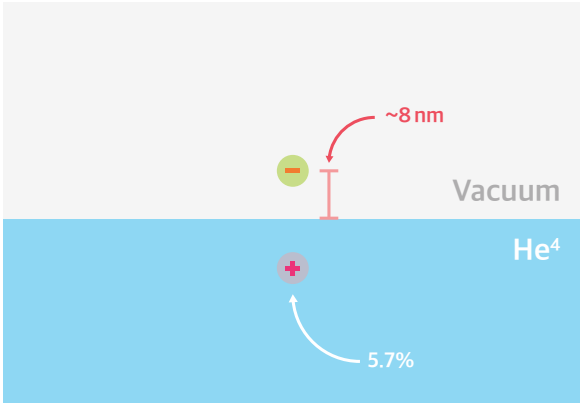

Figure 1.1: **Image Charge and Electrons on Helium.** When brought close to the interface between super-fluid helium and vacuum, the electron polarizes the helium, creating a small image charge that is approximately 5.7 % of the electron charge. Coulomb repulsion from the Helium valence electrons due to Pauli's exclusion principle creates a hard boundary condition at the interface, giving rise to a 1-D Rydberg potential normal to the super-fluid surface.

1.2.2 Dot Inside A Cavity

To create the single-electron quantum dot, we use electrodes embedded underneath super-fluid helium to create lateral confinement. This confinement provides the boundary condition needed for the electrons lateral (in-plane) motion to quantize into orbitals with energy spacing roughly in the low tens of GHz. We can tune the transition energy between nearby lateral modes by changing the DC bias potential.

Depending on the geometry of the superconducting resonator, either a single, a pair of double, or triple electrodes can be embedded under the trap. Figure 1.2 shows the schematics of a single electrode, but it could be easily extended to accommodate more sophisticated designs. In fact, the tuning-fork strip-line resonators used in Trident and Yggdrasil both have three embedded electrodes in the trap, to allow independent tuning of the overall trapping barrier height, and the center frequency.

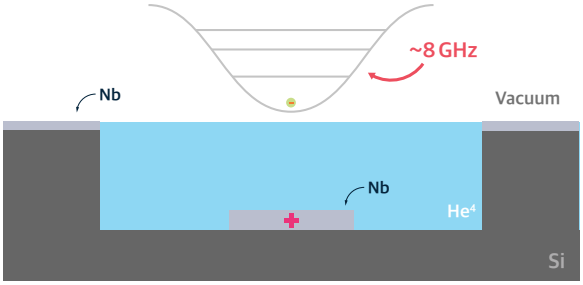

Figure 1.2: **Electron on Helium Quantum Dot Cross-section.** We plan to use 1. a micro-channel etched into the silicon substrate to stabilize the helium film thickness. 2. embedded Nb electrodes underneath the helium to create a parabolic trapping potential. In later samples, such biad electrode got split into two, so that the microwave field is in the image plane, along the induced electron dipole moment.

1.2.3 Integrating with A Cavity

A high-Q cavity is necessary for enhancing the dipole coupling between the electron and the photonic modes in the microwave environment. In addition, such cavities isolates the qubit from a noisy electromagnetic environment. Figure 1.3 shows the electric field of a typical co-planar waveguide cavity. It is possible to couple electrons on helium to 3D microwave cavities, but the reduced mode volume of superconducting planar resonators greatly enhance the cooperativity, which is necessary to reach stronger coupling.

Two types of planar resonators are used in these experiments:

1. co-planar waveguide (CPW) resonators with a DC bias in the center

2. quarter-wavelength strip-line resonators (the tuning fork) with a DC bias on the shorted end, with a electron trap located on the open end.

To integrate the single electron quantum dot with planar resonators, we want to place the dot at locations where the transverse microwave field is large in magnitude. In the tuning-fork design, we place the single-electron quantum dot at the opening end of the resonator where the microwave field is the largest. This design also provide easy access for the DC

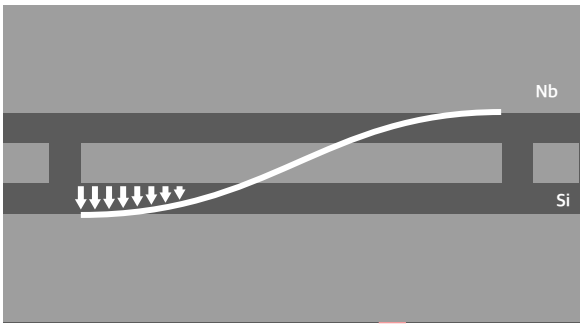

Figure 1.3: **Typical Microwave Circuit.** A typical superconducting microwave circuit takes the form of a co-planar waveguide resonator. The waveguide is terminated on each side by an open, which also acts as a capacitive coupler to the input and output ports. lightly-gray area are covered by e-beam evaporated niobium with a superconducting T_c around 8 K. Dark gray area are the exposed silicon substrate. White wave indicates the transverse electric field associated with the fundamental resonance mode. Opening on the left and right are capacitive couplers.

electrodes required to control the trap. Adding wire-bonds is crucial in reducing parasitic ground modes and maintain high-Q, even more so than integrating filter so with the DC electrodes.

1.2.4 Electron Spins as Spin Qubits

The spin-half degrees of freedom of the electron is another candidate for the qubit. The predicted theoretical spin life-time for electrons on helium is long. In addition, physically moving the electron around should not induce decoherence in the spin degree of freedom. The spin-orbit coupling between the electron spin and the isotopically pure helium 4 super-fliud is small. And the dipole coupling between the electron spins in a neighbor hood is also small due to the large distance caused by coulomb repulsion. This suggests it is possible to make a mobile electron spin memory–where gate operations occur at distinctive regions of the submerged circuit, and once loaded into the spin degree of freedom, the phase information can stay coherent for a long time unaffected by the physical transport of the carrier. This separation of spacial control of where qubit is and the quantum information inside, is a promising solution to a scalable quantum computer.

The plan for the next stage of this program is to turn on induced spin-orbit coupling between the spin degree of freedom of the electron and it's motional states, and use the spin as a quantum memory while the electron is transferred between different compartments of the circuit.

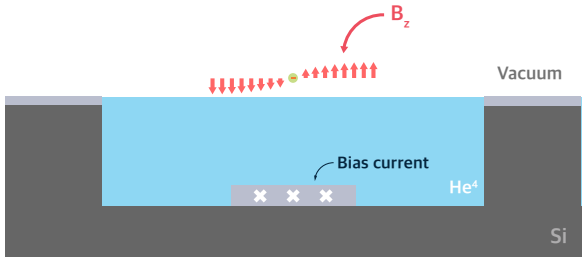

Figure 1.4: **Electrons on Helium Spin Qubit.** White crosses indicate the bias current running through the electrode on the bottom. Array of red arrows show the inhomogeneous magnetic field generated by this current bias. Only B_z (direction normal to the surface) is plotted.

1.3 Circuit QED

Here we offer a quick sketch of the Circuit QED theory. An atom can be treated as a two level system. Second-quantization allows us to re-write the Hamiltonian of the atom into the excitation and annihilation operator σ^+ and σ^- whereas the eigenstates are $|e\rangle$ and $|g\rangle$ with energy $\pm\frac{1}{2}\hbar\omega_a^2\sigma_z$. The harmonic oscillator is best described as an energy ladder $\{|i\rangle\}$, with energy levels

$$E|n\rangle = \frac{1}{2}\hbar\omega_r^2(n+\frac{1}{2}),$$

where $n = a^\dagger a$ is the index for the level.

The combined system encounters an interactive term, usually modeled by the the *Jaynes-*

Cummings hamiltonian

$$H_{\mathrm{JC}} = \frac{1}{2}\hbar\omega_r^2\left(a^\dagger a + \frac{1}{2}\right) + \frac{1}{2}\hbar\omega_a^2\sigma_z + \hbar g(a^\dagger\sigma^- + a\sigma^+).$$

In the circuit QED formalism, the atom is a non-linear circuit element, usually constructed by forming a Josephson junction between two thin superconducting wires. The junction allows the Cooper pairs to tunnel between the two superconducting wires, inducing a non-linear splitting in the energy level similar to that of the two-level atom.

todo: show the JC Hamiltonian with the circuit lumped element representations.

1.4 Decoherence in Electrons on Helium Qubits

In the case of quantum electrodynamics (QED) with electrons on helium (EonHe), the artificial atom is best modeled by the electrons as charged mass confined to a 2-dimensional surface. The dipole-dipole interaction between the electron and its neighbor is minimal at the large distance caused by the coulomb repulsion, so only the orbital state of the electrons need to be modeled.

The greatest experiment difficulty comes from the acoustic noise in the super-fluid substrate. Sensitive coupling between the helium super-fluid level and the electron energy levels created by the embedded electrodes causes dephasing in the single-electron quantum dot. At the time of writing, there are already a few thesis that came out with fairly comprehensive coverage on this topic. For the readers I would point to [11]. This thesis cover our effort building the first electron on helium ensemble coupled to a high-finesse superconducting cavity, and our effort towards a single electron quantum dot.

1.5 Overview of this Thesis

Details on circuit Quantum Electro-Dynamics has been well covered by a number of thesis at this point, so I will skip both. For an overview of circuitQED one can refer to [32, 28]. for electrons on helium physics, one can take a look at chapter 2 of [11].

Chapter 2, and 3 go into the details of the main experiments. In Chapter 2, our first experiment integrates electrons on helium with circuit QED on a DC biased superconducting co-planar waveguide resonator. $\sim 10^5$ electrons were trapped repetitively using a loading protocol, and held for a long time (> 12 hours). To understand the physics quantitatively, we developed a set of simulation tools that goes from electrostatic finite-element simulation of the sample geometry, to electrostatic configurations of the electrons, to a non-perturbative solution to the coupled electron plasmonic modes and the cavity photonic mode. These tools enabled us to reproduce the dispersive measurement results seen in experiments. And the attained agreement without many free-parameters provided a baseline for our next design.

Chapter 3 covers our effort on reducing the number of electrons coupled to the resonator. Much effort went into the simulation and verification of a quarter-wavelength, strip-line resonator design. In this design, a small EonHe quantum dot (electron trap) is placed at the opening end of the strip-line resonator ("the tuning fork") where it capacitively couples to the transverse electric field. On the electrostatic side, this design allowed us to greatly reduce the number of electrons visible to the resonator. It also changed the microwave mode that the electrons couple to to the odd, quarter wavelength fundamental mode, with a larger dipole coupling compared with the first experiment.

Multiple designs iterations occurred during this experiment. Yggdrasil adds more control to the trap by integrating a number of DC electrodes. This added DC complexity put a tighter constraint on the microwave design of the sample. Efforts were made to improve the quality factor of the superconducting resonator by reducing parasitic loss through the DC electrodes, as well as parasitic modes on the divided ground plane. The final design now

resembles those seen in the quantum dot community.

During this program of research, much of the time were spent on iterating fabrication processes for the samples, and improvements on the cryogenic experimental setup. Chapter 5 and 6 documents details of this work, with the hope of serving as a general guide for future students and experimentalists who face similar challenges as those encountered in this project.

CHAPTER 2

INTEGRATING ELECTRONS ON HELIUM WITH CIRCUIT QED

The quantized lateral motional states and the spin states of electrons trapped on the surface of superfluid helium have been proposed as basic building blocks of a scalable quantum computer. Circuit quantum electrodynamics (cQED) allows strong dipole coupling between electrons and a high-Q superconducting microwave resonator, enabling such sensitive detection and manipulation of electron degrees of freedom. Here we present the first realization of a hybrid circuit in which a large number of electrons are trapped on the surface of superfluid helium inside a coplanar waveguide resonator. The high finesse of the resonator allows us to observe large dispersive shifts that are many times the linewidth and make fast and sensitive measurements on the collective vibrational modes of the electron ensemble, as well as the superfluid helium film underneath. Furthermore, a large ensemble coupling is observed in the dispersive regime during experiment, and it shows excellent agreement with our numeric model. The coupling strength of the ensemble to the cavity is found to be ≈ 1 MHz per electron, indicating the feasibility of achieving single electron strong coupling [1].

In this chapter we design the sample and the experiment to isolate a single electron inside a trap where it is coupled to the transverse electric field of a superconducting microwave resonator.

Two sets of design constrains have to be fulfilled in order for this to happen: First of all, the electro-static trap have to have enough control to separate one electron from the bulk ensemble in the reservoir. Given the typical inter-electron spacing in a moderately bias electron crystal, this requirement determines the rough scale of the trap to be around $1 \approx 3$ microns.

[1] The bulk of this chapter is done jointly with Andrea Fragner, Gerwin Koolstra and David Schuster. The result appeared in [41] Yang, G. et al. Coupling an ensemble of electrons on superfluid helium to a superconducting circuit. *Phys. Rev. X* **6**, 011031 (2016).

Secondly, in order to observe the fine orbital absorption lines of the electrons inside the trap, the microwave resonator need to have high finesse while maintaining strong enough coupling. As it turned out, having various DC electrodes cut up the ground plane into large flaps created parasitic modes that greatly degraded the Q. In addition, having DC electrode close to the trap where the transverse MW field is strong led to leakage that also decreased the finesse of the resonator. To eliminate the parasitic modes, we wire-bond across the resonator with aluminum wires which superconducts at experiment temperature ($20 \sim 500$ mK). This provided the biggest improvements on the Q.

To further reduce MW leakage through coupling with the DC electrodes, we implemented low-pass filters with planar inductor and finger capacitors on each of the DC control line launchers. This design is similar to [25], and lead to minor improvements on the Q.

The resonator design we adopted is a differential pair quarter wavelength resonator. We call it the "tuning fork". This design is effectively a differential pair with one end terminated with a short. The voltage node on this shorted provides a natural location to add DC bias to the entire resonator.

The electron trap is located on the open end, where the electrons couple to the transverse field between the coupled pairs.

2.1 Introduction

Electrons on helium are a promising resource for quantum optics and quantum computing [19, 26, 9, 32]. They form an extremely clean two dimensional electron gas [22], as evidenced by a mobility exceeding $10^7\,\mathrm{cm}^2/\mathrm{Vs}$ [35, 34]. and the electron spin coherence time is predicted to exceed $10^3\,\mathrm{s}$ [19]. Electrons on helium have been used to study Wigner crystallization and quantum melting [40, 14, 3]. Recent experiments employ them as a powerful probe to study the topological domain structures on the surface of superfluid helium 3 [15, 16, 7]. In addition, it is now possible to build mesoscopic structures such as quantum dots with one

or a few electrons on helium, and single electron scale charge coupled devices [23, 30, 6, 37]. However, performing quantum experiments in this fascinating system has lagged behind that in semiconducting 2D electron gases, such as GaAs, as traditional measurement techniques cannot be applied to electrons on helium. In particular, it is not possible to make direct Ohmic contact to the electron gas. Additionally, the largely unscreened electron-electron Coulomb force and a hydrostatic instability of the system [13, 10] suppress the exchange interactions typically used in semiconductor spin qubits [25].

The circuit QED architecture [39, 5] offers a path to new experiments in the quantum regime as well as improving the sensitivity and bandwidth of existing measurements. In this hybrid approach, electrons are trapped above an on-chip superconducting microwave resonator. The presence of the electrons changes the effective capacitance of the cavity, resulting in a dispersive shift of the cavity resonance frequency. In the strong dispersive regime, the cavity frequency shift is larger than the cavity linewidth, and every photon measures the state of the electrons. Because the energy of a single photon in the cavity is higher than the thermal bath ($\hbar\omega > k_b T$), it is possible to conduct quantum optics experiments at the single photon level. This dispersive measurement is conceptually similar to the Sommer-Tanner technique [36], but the use of resonant superconducting circuits at microwave frequencies enables better impedance matching, resulting in faster and more sensitive measurements of small ensembles. Finally, the hybrid architecture allows one to leverage the substantial progress in superconducting circuits over the past decade [31, 8].

While in this work we study the motional coupling of the electrons, they also carry a spin degree of freedom. Ensembles of electrons on helium could also be used as a quantum memory, similar to previous work on solid-state spin ensembles [18, 33, 27, 20]. Uniquely, electrons on helium represent a mobile coherent spin system and can be dynamically arranged with gate electrodes. Finally, by engineering an artificial spin-orbit coupling it should be possible to achieve single-spin strong coupling [32, 24, 12, 38].

In this letter, we report the first implementation of a circuit QED architecture with electrons on helium. We show lithographic control and sub-nanometer measurement of the superfluid helium film thickness. Our experiment shows a strong dispersive shift due to the electrons that is many times the cavity linewidth. On average, the coupling per electron in the ensemble is about 1 MHz, suggesting single electron strong coupling should be within reach. Electrons can be held for many hours, and their normal mode frequencies and number can be controlled by adjusting the trapping potential. The resulting evolution of the dispersive shift agrees excellently with our numerical model.

2.2 Experimental Setup and detection technique

The electron on helium circuit QED setup consists of an integrated electron trap and coplanar waveguide (CPW) resonator (see Fig. 2.1a). The ground planes of the resonator are thicker than the center pin, forming a micro-capillary channel which determines and stabilizes the superfluid helium film thickness [21, 29]. The electrons are held in the resonator volume by a DC bias voltage applied to the center pin as shown in Fig. 2.1c.

The electrons are confined in both the transverse and longitudinal direction of the channel. In the transverse direction, a DC-voltage applied to the center pin creates a parabolic trapping potential (Fig. 2.1c) that confines the electron ensemble in the channel, colocated with the microwave field. In addition to the large electron trap formed by the resonator center pin, the devices also contain smaller μm-size electron traps positioned near the voltage maxima of the fundamental mode for future single-electron experiments (Fig. 2.1d). Those smaller traps were set to ground potential throughout the experiments discussed in the rest of this chapter. The input and output of the resonator (Fig. 2.1b) side of the coupler are held at 0 V to prevent electrons from leaking out the sides. Along the cavity DC bias lead, where the potential may be positive, constrictions shield the electrons ensuring that there is a potential barrier for escape.

The bare cavity resonance frequency is $\omega_0/2\pi \simeq 4.789$ GHz, loaded quality factor $Q_L \simeq 17750$ and corresponding decay rate $\kappa/2\pi \simeq 270$ kHz in the absence of any superfluid or electrons. The Q of the sample is set by the couplers, not by the internal Q of the resonator, despite the fact that the DC bias lead directly connects the center pin to a low impedance. This is possible because the connection is made at a voltage node, where radiation is minimized [4, 24]

2.3 Helium Dynamics

An important prerequisite for trapping electrons on helium in a micro-channel geometry is to establish a self-stabilized film of superfluid helium of known thickness, which can be achieved by capillary action filling of the channels from the low-lying bulk reservoir. The helium raises the effective dielectric constant of the waveguide, lowering the resonator frequency proportionally to the thickness, h.

To measure the cavity response to superfluid helium, we monitor the resonance frequency and quality factor in transmission while increasing the bulk helium reservoir level in small increments (the center pin is held at ground potential throughout this measurement). The results of such a helium filling experiment are presented in Fig. 2.2 a. Four different regimes can be clearly distinguished in the frequency shift (see Fig. 2.2 b). For small amounts of superfluid (regime I), an unsaturated van-der-Waals (vdW) film of thickness $h \sim 30$ nm forms as the liquid evenly coats the surface of the resonator and the interior of the sample cell, leading to small frequency shifts of $\Delta\omega_0(h)/2\pi \simeq -190$ kHz. Once the vdW film has saturated, the liquid film shape is determined by capillary action with a semi-circular profile $z(x) \sim x^2/2R_c(H)$ in the gap. The capillary radius $R_c(H) = \sigma/\rho g H$ is determined by the distance between the bulk helium level in the reservoir and the chip surface H, where $\sigma = 0.378 \times 10^{-3}$ N/m is the surface tension of liquid helium in vacuum, $\rho = 0.154 \times 10^{-3}$ kg/cm^3 the mass density and g the gravitational acceleration. When the radius of curvature

becomes on the order of the gap width $R_c \sim w_G$, the gap starts to fill up by capillary action and is filled completely for $R_c \gg w_G$ (regime II). Small increases in shift in the subsequent "flat" regime are due to decrease in the curvature of the helium profile. Finite element simulations show that when the channel is filled ($h = 800$ nm) the frequency shift is -8 MHz, in good agreement with the observed data. As $H \to 0$, the radius of curvature becomes on the order of the chip dimensions and eventually starts to diverge. We attribute the abrupt jump at 170 mm^3 to the formation of a thick film which spans the entire chip (regime III) and is supported by the sample holder. As $R_c \to \infty$, the superfluid film becomes sensitive to mechanical vibrations and small fluctuations in the reservoir level which manifests itself in a perceived drop in quality factor in this regime. Once the reservoir has been completely filled, the helium fills the region above the chip linearly (regime IV) until the resonator becomes insensitive at thickness $h \sim 6\,\mu$m, corresponding to a frequency shift of $\Delta\omega_0(h)/2\pi = -14.145$ MHz, again in good agreement with numerical simulations that predict a final frequency shift of -14.1 MHz. All subsequent experiments are done at the filling level indicated by the black arrow in Fig.2.2 a, which corresponds to $h \approx 647$ nm where the frequency shift is $\Delta\omega_0(h)/2\pi \simeq -7.4$ MHz, and is only slightly changed by additional fluid introduced to the reservoir.

The superfluid level in the resonator gap can be modulated in-situ by sweeping the voltage of the center pin $V_{\rm cp}$. To lowest order, the equilibrium film thickness at the center of the gap is determined by the electromechanical force on the film surface and surface tension with a quadratic voltage dependence $h(V_{\rm cp}) \approx h(0) + (V_{\rm cp}^2/16\sigma)(\varepsilon_{\rm He} - \varepsilon_0)$. Fig. 2.2 c shows measured frequency shift and quality factor as functions of center pin voltage at a reservoir level of $H \simeq 4$ mm where the gap is partly filled by capillary action. The resonance frequency shows a parabolic voltage dependence while the quality factor remains constant, as expected. The maximum observed shift at $V_{\rm cp} = +6$ V of $\Delta\omega_0/2\pi = -100$ kHz corresponds to a change in film thickness of $\Delta h \simeq 13$ nm at the center of the gap.

The slight offset of the other-wise symmetric response is not well-understood, and it is device dependent. The frequency sensitivity to level changes in the gap can be estimated from finite element electromagnetic simulations to be $\approx$ 8 kHz/nm, consistent with the overall slope and frequency shift. The stability of the capillary action film is estimated from consecutive single-shot transmission measurements (gray data points in Fig. 2.2 c), with $N = 80$ frequency measurements per voltage bias point. Slow fluctuations of the helium level are manifested in the $\delta\omega_0^{(\mathrm{rms})}/2\pi = 16$ kHz scatter of resonance frequencies (gray points in Fig. 2.2c) corresponding to helium level fluctuations of $\delta h^{(\mathrm{rms})} \approx 2.6$ nm. The demonstrated electrostatic control over the helium level can be used to dynamically reduce the fluctuations.

In summary, the microwave measurement provides a high bandwidth way to measure the helium level and its fluctuations, down to pm/$\sqrt{\mathrm{Hz}}$ level sensitivity. Using this technique, we establish a lithographically defined, stabilized superfluid helium film within the cavity-trap. In the regime of the experiment, the channel helium level is insensitive to the small differences in the amount of helium put into the sample box. The measured helium level fluctuations are relatively small and will be monitored to see if they have a significant effect on the electron coherence time through changes in the trapping potential.

2.4 Dispersive measurements of electrons in a cavity

Following uncharged superfluid measurements, we proceed to load electrons into the cavity mode volume and detect the trapped electron ensemble in transmission measurements. Electrons are generated via pulsed thermionic emission from a tungsten filament mounted in vacuum above the device and attracted towards the superfluid surface in the resonator channel by a positive trap voltage V_{cp}. After waiting for the sample to cool, the cavity transmission is monitored while tuning the center pin voltage V_{cp} (Fig. 2.3) starting from +3V. The dispersive interaction of the cavity with the trapped ensemble leads to a voltage-

dependent shift of the cavity resonance towards lower frequencies before reverting back at negative trap potentials. We observe maximum resonance shifts of up to $\Delta\omega > 10\kappa$ cavity linewidths in frequency while Q is somewhat reduced (Fig. 2.3 b). The electron-induced frequency shift reaches a maximum of $\Delta\omega_{\max}/2\pi = -2.47$ MHz at $V_{\rm cp}^{(\rm th)} = +0.91$ V with a drop in quality factor and a corresponding increase in cavity decay rate of $\Delta\kappa_{\max}/2\pi = 122$ kHz (blue curves in Fig. 2.3 c and d). These changes in the cavity resonance frequency are at least an order of magnitude larger than those caused by the electric field induced helium film thickness change without electrons. Below the threshold $V_{\rm cp}^{(\rm th)}$, the electron-induced shifts decrease gradually as electrons are lost from the trapping region. To ensure that the observed cavity response is due to the trapped electron ensemble, we performed a control experiment where the filament was fired while the center pin was biased at -1V. The voltage is then swept in the reverse direction (red curves in Fig. 2.3 c and d). The voltage dependent signal is completely absent (see Fig. 2.2 b and discussion above). The ensemble-induced cavity response has been reproduced in independent experiments using five different devices. The maximum observed resonance shifts are repeatable and generally vary between $2 - 8$ MHz based on loading conditions.

To further investigate the quantitative form of the cavity shift as a response to the number of electrons N and the bias voltage $V_{\rm cp}$, we designed a protocol to partially drain the electrons from the trap. In the following experiment at the end of the first sweep from +3V (bottom half of blue curve in Fig. 2.4), we deliberately sweep down below the $V_{\rm cp}^{(\rm th)}$ to introduce electron loss. Now with fewer electrons in the trap (top half of blue curve in Fig. 2.4), the cavity resonance shift is smaller in magnitude than before, but non-hysteretic unless another electron-loss event is triggered. For subsequent sweeps, we then set successively lower stop voltages. The final sweep (orange curve in Fig. 2.4) depletes the mode volume of all electrons as evidenced by the vanishing frequency shift on the final upward sweep. By carefully tuning the stop voltages and number of sweeps we can controllably reduce the number of electrons

as desired.

A quantitative understanding of the electron-cavity interaction requires modeling of the classical many-body interactions between electrons as well as the coupling of the resulting electron normal modes with the cavity. We develop a non-perturbative numerical model which determines the electron ensemble configuration, frequencies and coupling to the cavity. First simulated annealing is employed to find the minimal energy configuration of the electrons. The electrostatic potential used in this step is constructed using field profile data derived from the sample geometry. After obtaining the electron configurations, we solve the equations of motion of the cavity-electron coupled system in a non-perturbative way to obtain the cavity frequency shift. For a given number of electrons in the trap, this calculation is repeated for various V_{cp} to produce the corresponding frequency shift curve. Curves for various number of electrons are computed, and no fitting parameters are used in the model besides picking the closest iso-electron number curve. Fig. 2.4 shows excellent agreement between the data and our computational model. The model is described in detail in section 2.6.

Using the measured signal and our model, we can infer the electron mode frequency and coupling strength g_{rms}. The frequency of the strongest coupled mode grows proportionally to $\sqrt{V_{\mathrm{cp}}}$ and is roughly 25 GHz at $V_{\mathrm{cp}} = 0.5$ V, which shows we are well within the dispersive regime. In this regime, the cavity frequency shift is related to the RMS single electron coupling by $\Delta\omega = N g_{\mathrm{rms}}^2/(\omega_e - \omega_0)$, where ω_e is the electron motional frequency, ω_0 is the cavity frequency and N is the number of electrons. We determine both ω_e and N by comparing the data from Fig. 2.4 to simulation results (see section 2.6) and find $g_{\mathrm{rms}}/2\pi = 0.8$ MHz for a 1 μm wide electron configuration. In future trap designs, additional guard electrodes are in-place to improve trap stability at low voltage allowing access to the resonant regime. The coupling though quite large already, can be enhanced further by shrinking the dimensions of the trap.

There are two types of electron loss observed. The first, which determines the number of electrons loaded, occurs at higher V_{cp} due to hydrodynamic instability[21]. The density immediately after loading at $V_{\mathrm{cp}} = 3\mathrm{V}$ was $n \approx 2 \times 10^9\,\mathrm{cm}^{-2}$. The second type of electron loss occurs when the trap depth becomes sufficiently shallow, such that electrons can leak out of the trap. We model this phenomenologically by assuming that electrons are lost if the potential difference between ground plane and electrons is less than V_{leak}. Using V_{leak} as a single fit parameter in the molecular dynamics simulation, we find best agreement between simulation and experiment when $V_{\mathrm{leak}} = 530\,\mathrm{mV}$. The residual population for small electron numbers at small V_{cp} (orange curve in Fig. 2.4) is not well understood.

In summary, we have demonstrated the successful trapping and detection of an electron ensemble above the surface of superfluid helium in the circuit QED architecture. The measurement technique introduced here could extend traditional electrons on helium experiments to smaller ensembles and enable observation of the electron dynamics. The observation of the large dispersive shift and the good agreement with our numerical simulations indicate that it should be possible to perform cavity QED experiments in a single electron quantum dot. Though small, the fluctuations in the helium film thickness are an important source of decoherence for the electron motional states, and merit further study. Finally, the sensitivity of the device to helium thickness changes can be exploited for novel cavity optomechanics experiments with superfluid ripplons.

2.5 Numerical Simulation

The situation where many interacting electrons in an electrostatic trap couple to a microwave resonator represents an interesting physical system. Experimentally it is not possible to directly observe how electrons arrange themselves inside the trap. However, such configurations contain important information of the electrostatic and microwave properties of the system. Therefore, the goal of this chapter is to develop a set of tools that provides a complete

quantitative understanding of the classical interaction between few electrons in a trap and a microwave resonator. The first step is to start with an electrostatic simulation and solve for the equilibrium position of each individual electron in a given trapping potential.

With the electron configuration at hand, we can then calculate the dispersive shift of the cavity. We take a non-perturbative approach to directly compute the cavity frequency from the equation of motion of the electrons-cavity coupled system. The numerical results are confirmed by a simple analytic model in the low density regime. In the high density regime where our experiment lies, the simulation model agrees well with the experimental data. Using this model, we are able to derive a number of relevant quantities, such as the total number of electrons on the resonator, and the average coupling per electron.

The fabrication recipe and experimental setup can be found at the end of the document.

2.5.1 Electrostatic Simulation

The first step of our modeling effort starts with the electrostatic simulation of the trapping potential. We simulate the trapping potential for a CPW in Maxwell, a finite element simulation tool. Since the geometry does not change in the y-direction, we only extract the cross-sectional profile. This numerical potential profile is then fitted with a 14^{th} order polynomial (with only the even power terms). From this we extract the second order coefficient to construct an ideal parabolic potential for use in the molecular dynamics simulation. Our analysis shows that for the most part, the electrons stay within 500 nm from the center, where this approximation is good.

Numerically, the electrostatic potential used in the molecular dynamics simulation is

$$U(x, V_{\mathrm{cp}}) = 0.0733\, eV_{\mathrm{cp}}x^2, \tag{2.1}$$

where x is measured in μm from the center of the trap and V_{cp} is the bias voltage applied

to the center pin.

2.6 Molecular Dynamics

To solve for the equilibrium positions of the electrons in a given electrostatic potential, we use a simulation method called molecular dynamics. Molecular dynamics represents a class of deterministic, iterative algorithms that can be used to find solutions to many-body problems. For this work, we use the package HOOMD [2]. This *general-purpose* particle simulation toolkit scales on multi-core CPU and GPUs which allows us to quickly anneal up to 4000 electrons.

In a typical simulation run, we start with a fixed number of electrons n. Due to the large number of pairwise interactions that grows quadratically with n, we shrink our 12 mm long resonator from the actual length down to a $50\,\mu\text{m} \times 50\,\mu\text{m}$ box with periodic boundary conditions on each side. Simulation and experimental results can then be compared by multiplying the number of electrons in the $50\,\mu\text{m} \times 50\,\mu\text{m}$ box by $L_{\text{res}}/L_{\text{box}} \approx 243$. In the remainder of this chapter we refer to the number of electrons on the resonator as $N = 243 \cdot n$.

There is no long-range screening in our simulation. However, the Coulomb interaction is cut off at $20\,\mu\text{m}$ to prevent electrons from interacting with their own image charges across the periodic boundary condition, causing an explosion of pairwise interactions in the system.

The lowest energy electron configuration is found by annealing the system. Here the temperature of the ensemble is gradually decreased until it reaches a temperature below 1 K. Starting from a random initial electron distribution, a typical annealing procedure for $n = 1000$ ($N = 2.43 \times 10^5$) in a $50\mu\text{m} \times 50\ \mu\text{m}$ box takes 20 minutes. The simulation has two input parameters: N and V_{cp}, the second of which determines the depth of the trapping potential. We simulate several N's for the range of V_{cp} used in the experiment. Results from multiple runs with different random initial conditions were consistent.

Fig.2.6 shows equilibrium electron configurations for six different pairs of $\{N, V_{\text{cp}}\}$. The

electrons arrange themselves in rows along the y-direction, the direction perpendicular to the electrostatic trap. Increasing the trap bias voltage leads to an increase in electron density, a reduction in the number of rows, and a decrease of the overall width of the ensemble. This is depicted more clearly in Fig.2.7 for $N = 2.43 \times 10^5$. In this figure the color represents the binned electron density along x (bin size 6 nm), which was obtained by integrating the electron distribution along y. Gradual transitions from 9 rows to 4 rows can be observed as V_{cp} is swept from 0 to 4V.

2.7 Equation of motion

With the electron configurations in hand, our goal is to compute the dispersive resonance frequency shift. One approach is to calculate all the electron normal modes, and use perturbation theory to find the frequency shift. This approach is difficult, as defects in the electron Wigner crystal and the flat potential along the y-direction lead to degenerate modes. To tackle this problem, we follow a non-perturbative approach, and calculate the cavity normal mode from the equations of motion of the entire electron-cavity coupled system.

2.7.1 Electron Subsystem

To calculate the equations of motion for the electrons, we use a Lagrangian formalism. The full Lagrangian $\mathcal{L}$ consists of an electronic part $\mathcal{L}_e$, a cavity part $\mathcal{L}_c$ and an interaction energy $\mathcal{L}_{\text{coupling}}$. The electronic part is given by

$$\mathcal{L}_e = \frac{1}{2} m_e \sum_i \dot{\mathbf{r}}_i^2 - e \sum_i V_{\text{DC}}(\mathbf{r}_i) - \frac{1}{2} \frac{e^2}{4\pi\epsilon_0} \sum_i \sum_{j \neq i} \frac{1}{|\mathbf{r}_i - \mathbf{r}_j|}, \tag{2.2}$$

where $\mathbf{r}_i = (x_i, y_i)$ is the coordinate of electron i and $V_{\text{DC}}(\mathbf{r}_i)$ is the electrostatic potential that defines the static trap for the electrons. In our case $V_{\text{DC}}(\mathbf{r}) = \frac{1}{2} k_{\text{trap}} x^2$. The trap depth and thus k_{trap} are determined by the center pin bias voltage.

2.7.2 Cavity

Working in the charge basis, the cavity part of the Lagrangian is

$$\mathcal{L}_c = \frac{1}{2}L\dot{Q}^2 - \frac{Q^2}{2C}, \tag{2.3}$$

where L and C are the effective inductance and capacitance respectively.

2.7.3 Electron-Cavity Coupling

The coupling between the electrons and the cavity can be written straightforwardly as

$$\mathcal{L}_{\text{coupled}} = e\sum_i V_{\text{RF}}(\mathbf{r}_i, Q). \tag{2.4}$$

Here $V_{\text{RF}}(\mathbf{r}_i, Q)$ is the RF potential generated by the resonator. It should be emphasized that generally this potential may have a different position dependence than the electrostatic potential $V_{\text{DC}}(\mathbf{r}) = \frac{1}{2}k_{\text{trap}}x^2$. However, in this work the electrostatic potential is determined by the bias voltage on the center pin, whereas $V_{\text{RF}}(\mathbf{r}_i, Q)$ depends on the RF voltage (or rather charge) on the center pin. Since both potentials originate from the center pin, the functional dependence is the same.

To proceed with the analysis, the charge and position dependent parts are separated, such that

$$\mathcal{L}_{\text{coupled}} = \frac{eQ}{C}\sum_i U_{\text{RF}}(\mathbf{r}_i). \tag{2.5}$$

$U_{\text{RF}}(\mathbf{r}_i)$ is a dimensionless function that describes the position dependence of the microwave potential.

2.7.4 Full Equations of Motion

The equations of motion are easily obtained by calculating the derivatives with respect to x_i, y_i, Q and their time derivatives. In general

$$\frac{\mathrm{d}}{\mathrm{d}t}\frac{\partial \mathcal{L}}{\partial \dot{q}} - \frac{\partial \mathcal{L}}{\partial q} = 0, \tag{2.6}$$

which for the cavity results in:

$$L\ddot{Q} + \frac{Q}{C} + \frac{e}{C}\sum_i U_{\mathrm{RF}}(\mathbf{r}_i) = 0 \tag{2.7}$$

In a similar fashion, the equation of motion in the x-direction for electron i becomes

$$m_e\ddot{x}_i + e\frac{\partial V_{\mathrm{DC}}}{\partial x_i}(\mathbf{r}_i) + \frac{eQ}{C}\frac{\partial U_{\mathrm{RF}}}{\partial x_i}(\mathbf{r}_i) - \frac{1}{2}\frac{e^2}{4\pi\epsilon_0}\sum_{j\neq i}\frac{x_i - x_j}{|\mathbf{r}_i - \mathbf{r}_j|^3} = 0. \tag{2.8}$$

Eqs. (2.7) and (2.8) are the exact equations of motion but are also highly nonlinear. To this end the system is linearized around the equilibrium point $(x_{i,\mathrm{eq}}, y_{i,\mathrm{eq}}, Q_{\mathrm{eq}} = 0)$. This means that the equations of motion will contain terms involving $\mathbf{r}_{i,\mathrm{eq}}$. This underlines that obtaining the equilibrium electron configuration via molecular dynamics simulations is of critical importance.

At the equilibrium point the potential energy

$$\mathcal{U} = \frac{Q^2}{2C} + \frac{eQ}{C}\sum_i U_{\mathrm{RF}}(\mathbf{r}_i) + e\sum_i V_{\mathrm{DC}}(\mathbf{r}_i) + \frac{1}{2}\frac{e^2}{4\pi\epsilon_0}\sum_i\sum_{j\neq i}\frac{1}{|\mathbf{r}_i - \mathbf{r}_j|} \tag{2.9}$$

of the system is minimized, such that

$$\frac{\partial \mathcal{U}}{\partial x_i}(x_{i,\mathrm{eq}}, y_{i,\mathrm{eq}}, Q_{\mathrm{eq}}=0) = e\frac{\partial V_{\mathrm{DC}}}{\partial x_i}(\mathbf{r}_{i,\mathrm{eq}}) - \frac{1}{2}\frac{e^2}{4\pi\epsilon_0}\sum_{j\neq i}\frac{x_{i,\mathrm{eq}}-x_{j,\mathrm{eq}}}{|\mathbf{r}_{i,\mathrm{eq}}-\mathbf{r}_{j,\mathrm{eq}}|^3} = 0 \tag{2.10}$$

$$\frac{\partial \mathcal{U}}{\partial y_i}(x_{i,\mathrm{eq}}, y_{i,\mathrm{eq}}, Q_{\mathrm{eq}}=0) = e\frac{\partial V_{\mathrm{DC}}}{\partial y_i}(\mathbf{r}_{i,\mathrm{eq}}) - \frac{1}{2}\frac{e^2}{4\pi\epsilon_0}\sum_{j\neq i}\frac{y_{i,\mathrm{eq}}-y_{j,\mathrm{eq}}}{|\mathbf{r}_{i,\mathrm{eq}}-\mathbf{r}_{j,\mathrm{eq}}|^3} = 0 \tag{2.11}$$

$$\frac{\partial \mathcal{U}}{\partial Q}(x_{i,\mathrm{eq}}, y_{i,\mathrm{eq}}, Q_{\mathrm{eq}}=0) = \frac{e}{C}\sum_i U_{\mathrm{RF}}(\mathbf{r}_{i,\mathrm{eq}}) = 0 \tag{2.12}$$

Finally, Eqs. (2.7) and (2.8) can be linearized. First consider Eq.(2.7). If δQ is a small deviation from $Q_{\mathrm{eq}}=0$ and δx_i is a small deviation from $x_{i,\mathrm{eq}}$ this equation may be written as

$$L\delta\ddot{Q} + \frac{\delta Q}{C} + \frac{e}{C}\sum_i\left[U_{\mathrm{RF}}(\mathbf{r}_{i,\mathrm{eq}}) + \frac{\partial U_{\mathrm{RF}}}{\partial x_i}(\mathbf{r}_{i,\mathrm{eq}})\delta x_i + \frac{\partial U_{\mathrm{RF}}}{\partial y_i}(\mathbf{r}_{i,\mathrm{eq}})\delta y_i\right] = 0, \tag{2.13}$$

and by using Eq.(2.12) we arrive at the equation of motion for the cavity:

$$L\delta\ddot{Q} + \frac{\delta Q}{C} + \frac{e}{C}\sum_i\left[\frac{\partial U_{\mathrm{RF}}}{\partial x_i}(\mathbf{r}_{i,\mathrm{eq}})\delta x_i + \frac{\partial U_{\mathrm{RF}}}{\partial y_i}(\mathbf{r}_{i,\mathrm{eq}})\delta y_i\right] = 0,. \tag{2.14}$$

Now for the electrons we linearize Eq.(2.8). To do this, it is useful to note that (see Fig.2.8)

$$\begin{aligned}\frac{x_i-x_j}{|\mathbf{r}_i-\mathbf{r}_j|^3} &= \frac{r_{ij}\cos\theta_{ij} + (\delta x_i - \delta x_j)}{r_{ij}^3\left[\cos^2\theta_{ij}\left(1+\frac{\delta x_i-\delta x_j}{r_{ij}\cos\theta_{ij}}\right)^2 + \sin^2\theta_{ij}\left(1+\frac{\delta y_i-\delta y_j}{r_{ij}\sin\theta_{ij}}\right)^2\right]^{3/2}} \\ &= \frac{\cos\theta_{ij}}{r_{ij}^2} - \frac{1}{2}(1+3\cos(2\theta_{ij}))\frac{\delta x_i-\delta x_j}{r_{ij}^3} - \frac{3}{2}\sin(2\theta_{ij})\frac{\delta y_i-\delta y_j}{r_{ij}^3} + \mathcal{O}(\delta^2).\end{aligned} \tag{2.15}$$

Here $r_{ij} = |\mathbf{r}_{i,\mathrm{eq}} - \mathbf{r}_{j,\mathrm{eq}}|$ and θ_{ij} is the angle between $\mathbf{r}_{i,\mathrm{eq}} - \mathbf{r}_{j,\mathrm{eq}}$ and the x-axis.

The linearized version of the equation of motion then becomes

$$m_e\delta\ddot{x}_i + e\left[\frac{\partial V_{\mathrm{DC}}}{\partial x_i}(\mathbf{r}_{i,\mathrm{eq}}) + \frac{\partial^2 V_{\mathrm{DC}}}{\partial x_i^2}(\mathbf{r}_{i,\mathrm{eq}})\delta x_i + \frac{\partial^2 V_{\mathrm{DC}}}{\partial x_i \partial y_i}(\mathbf{r}_{i,\mathrm{eq}})\delta y_i\right] + \frac{e\delta Q}{C}\frac{\partial U_{\mathrm{RF}}}{\partial x_i}(\mathbf{r}_{i,\mathrm{eq}})$$
$$-\frac{1}{2}\frac{e^2}{4\pi\epsilon_0}\sum_{j\neq i}\frac{1}{r_{ij}^3}\left(r_{ij}\cos\theta_{ij} - \frac{1}{2}\left(1+3\cos(2\theta_{ij})\right)\left(\delta x_i - \delta x_j\right) - \frac{3}{2}\sin(2\theta_{ij})(\delta y_i - \delta y_j)\right) = 0 \tag{2.16}$$

Using Eq.(2.10) this can be simplified to

$$m_e\delta\ddot{x}_i + e\frac{\partial^2 V_{\mathrm{DC}}}{\partial x_i^2}(\mathbf{r}_{i,\mathrm{eq}})\delta x_i + e\frac{\partial^2 V_{\mathrm{DC}}}{\partial x_i \partial y_i}(\mathbf{r}_{i,\mathrm{eq}})\delta y_i + \frac{e}{C}\frac{\partial U_{\mathrm{RF}}}{\partial x_i}(\mathbf{r}_{i,\mathrm{eq}})\delta Q$$
$$+\frac{1}{4}\frac{e^2}{4\pi\epsilon_0}\sum_{j\neq i}\left[\left(1+3\cos(2\theta_{ij})\right)\frac{\delta x_i - \delta x_j}{r_{ij}^3} + 3\sin(2\theta_{ij})\frac{\delta y_i - \delta y_j}{r_{ij}^3}\right] = 0. \tag{2.17}$$

Finally, for the sake of transparency let

$$k_{ij}^{\pm} = \frac{1}{4}\frac{e^2}{4\pi\epsilon_0}\frac{1\pm 3\cos(2\theta_{ij})}{r_{ij}^3} \quad \text{and} \quad l_{ij} = \frac{1}{4}\frac{e^2}{4\pi\epsilon_0}\frac{3\sin(2\theta_{ij})}{r_{ij}^3} \tag{2.18}$$

such that Eq.(2.17) simplifies to the linearized equation of motion for the electrons:

$$m_e\delta\ddot{x}_i + \frac{e}{C}\frac{\partial U_{\mathrm{RF}}}{\partial x_i}(\mathbf{r}_{i,\mathrm{eq}})\delta Q + \left(e\frac{\partial^2 V_{\mathrm{DC}}}{\partial x_i^2}(\mathbf{r}_{i,\mathrm{eq}}) + \sum_{j\neq i}k_{ij}^{+}\right)\delta x_i$$
$$-\sum_{j\neq i}k_{ij}^{+}\delta x_j + \left(e\frac{\partial^2 V_{\mathrm{DC}}}{\partial x_i \partial y_i}(\mathbf{r}_{i,\mathrm{eq}}) + \sum_{j\neq i}l_{ij}\right)\delta y_i - \sum_{j\neq i}l_{ij}\delta y_j = 0. \tag{2.19}$$

Above equations show that a change in position (either in x or y) of electron j translates into an x displacement of electron i. In the y-direction the equation of motion follows in a

similar way:

$$m_e\delta\ddot{y}_i + \frac{e}{C}\frac{\partial U_{\mathrm{RF}}}{\partial y_i}(\mathbf{r}_{i,\mathrm{eq}})\delta Q + \left(e\frac{\partial^2 V_{\mathrm{DC}}}{\partial y_i^2}(\mathbf{r}_{i,\mathrm{eq}}) + \sum_{j\neq i} k_{ij}^{-}\right)\delta y_i$$
$$-\sum_{j\neq i} k_{ij}^{-}\delta y_j + \left(e\frac{\partial^2 V_{\mathrm{DC}}}{\partial x_i \partial y_i}(\mathbf{r}_{i,\mathrm{eq}}) + \sum_{j\neq i} l_{ij}\right)\delta x_i - \sum_{j\neq i} l_{ij}\delta x_j = 0. \tag{2.20}$$

The system of equations (2.14), (2.19) and (2.20) can be written in matrix form as follows:

$$\mathcal{M}\begin{pmatrix} \delta\ddot{Q} \\ \delta\ddot{x}_1 \\ \vdots \\ \delta\ddot{y}_1 \\ \vdots \end{pmatrix} = -\mathcal{K}\begin{pmatrix} \delta Q \\ \delta x_1 \\ \vdots \\ \delta y_1 \\ \vdots \end{pmatrix}, \tag{2.21}$$

where $\mathcal{K}$ and $\mathcal{M}$ are the kinetic and mass matrix of the system, respectively. The entries of both matrices can be easily read from the equations of motion:

$$\mathcal{M} = \begin{pmatrix} L & 0 & 0 & \dots & 0 & 0 & \dots \\ 0 & m_e & 0 & \dots & 0 & 0 & \dots \\ 0 & 0 & m_e & \dots & 0 & 0 & \dots \\ \vdots & \vdots & \vdots & \ddots & \vdots & \vdots & \ddots \\ 0 & 0 & 0 & \dots & m_e & 0 & \dots \\ 0 & 0 & 0 & \dots & 0 & m_e & \dots \\ \vdots & \vdots & \vdots & \ddots & \vdots & \vdots & \ddots \end{pmatrix} \tag{2.22}$$

and

$$\mathcal{K} = \begin{pmatrix} \frac{1}{C} & \frac{e}{C}\frac{\partial U_{\mathrm{RF}}}{\partial x_1}(\mathbf{r}_{1,\mathrm{eq}}) & \frac{e}{C}\frac{\partial U_{\mathrm{RF}}}{\partial x_2}(\mathbf{r}_{2,\mathrm{eq}}) & \cdots & \frac{e}{C}\frac{\partial U_{\mathrm{RF}}}{\partial y_1}(\mathbf{r}_{1,\mathrm{eq}}) & \frac{e}{C}\frac{\partial U_{\mathrm{RF}}}{\partial y_2}(\mathbf{r}_{2,\mathrm{eq}}) & \cdots \\ \frac{e}{C}\frac{\partial U_{\mathrm{RF}}}{\partial x_1}(\mathbf{r}_{1,\mathrm{eq}}) & e\frac{\partial^2 V_{\mathrm{DC}}}{\partial x_1^2}(\mathbf{r}_{1,\mathrm{eq}}) + \sum_{j\neq 1} k_{1j}^{+} & -k_{12}^{+} & \cdots & e\frac{\partial^2 V_{\mathrm{DC}}}{\partial x_1 \partial y_1}(\mathbf{r}_{1,\mathrm{eq}}) + \sum_{j\neq 1} l_{1j} & -l_{12} & \cdots \\ \frac{e}{C}\frac{\partial U_{\mathrm{RF}}}{\partial x_2}(\mathbf{r}_{2,\mathrm{eq}}) & -k_{21}^{+} & e\frac{\partial^2 V_{\mathrm{DC}}}{\partial x_2^2}(\mathbf{r}_{2,\mathrm{eq}}) + \sum_{j\neq 2} k_{2j}^{+} & \cdots & -l_{21} & e\frac{\partial^2 V_{\mathrm{DC}}}{\partial x_2 \partial y_2}(\mathbf{r}_{2,\mathrm{eq}}) + \sum_{j\neq 2} l_{2j} & \cdots \\ \vdots & \vdots & \vdots & \ddots & \vdots & \vdots & \ddots \\ \frac{e}{C}\frac{\partial U_{\mathrm{RF}}}{\partial y_1}(\mathbf{r}_{1,\mathrm{eq}}) & e\frac{\partial^2 V_{\mathrm{DC}}}{\partial x_1 \partial y_1}(\mathbf{r}_{1,\mathrm{eq}}) + \sum_{j\neq 1} l_{1j} & -l_{12} & \cdots & e\frac{\partial^2 V_{\mathrm{DC}}}{\partial y_1^2}(\mathbf{r}_{1,\mathrm{eq}}) + \sum_{j\neq 1} k_{1j}^{-} & -k_{12}^{-} & \cdots \\ \frac{e}{C}\frac{\partial U_{\mathrm{RF}}}{\partial y_2}(\mathbf{r}_{2,\mathrm{eq}}) & -l_{21} & e\frac{\partial^2 V_{\mathrm{DC}}}{\partial x_2 \partial y_2}(\mathbf{r}_{2,\mathrm{eq}}) + \sum_{j\neq 2} l_{2j} & \cdots & -k_{21}^{-} & e\frac{\partial^2 V_{\mathrm{DC}}}{\partial y_2^2}(\mathbf{r}_{2,\mathrm{eq}}) + \sum_{j\neq 2}\ k_{2j}^{-} & \cdots \\ \vdots & \vdots & \vdots & \ddots & \vdots & \vdots & \ddots \end{pmatrix}. \tag{2.23}$$

Terms in $\mathcal{M}$ and $\mathcal{K}$ that represent the cavity mode and electron-cavity coupling are shaded pink. The electron x and y motion are shaded green and blue, respectively. Lastly, terms that involve $x - y$ and $y - x$ coupling are shaded orange.

With the kinetic matrix and mass matrix, the eigenvalue problem

$$\mathcal{M}^{-1}\mathcal{K}|\eta_i\rangle = \omega_i^2|\eta_i\rangle \tag{2.24}$$

can be solved to obtain the normal modes $|\eta_i\rangle$ and corresponding frequencies ω_i. The eigenfrequency corresponding to the mode with the highest cavity participation tells us the dispersive cavity shift.

2.7.5 Constraining the Motion Along the x-axis

In the previous section the most general equations of motion for a two dimensional confined electron gas were derived. In this case, the static trap is flat in the y-direction:

$$V_{\mathrm{DC}}(\mathbf{r}_i) = \frac{1}{2}k_{\mathrm{trap}}x_i^2, \tag{2.25}$$

and U_{RF} has the same $\mathbf{r}$-dependence as V_{DC}:

$$U_{\mathrm{RF}}(\mathbf{r}_i) = \beta x_i^2. \tag{2.26}$$

Since both V_{DC} and U_{RF} do not depend on y_i the equations of motion simplify drastically. Additionally, since the trapping potential is flat along the y-direction and due to the presence of defects – either intrinsic or due to imperfect annealing – one can get modes with imaginary or zero frequency. To reduce the impact of these modes we "freeze" the modes in the y-direction, i.e. we set $\delta y_i = 0$ in what follows to simplify the equations of motion even further.

After these simplifications the matrices that govern the equations of motion read

$$\mathcal{M} = \begin{pmatrix} L & 0 & 0 & \dots \\ 0 & m_e & 0 & \dots \\ 0 & 0 & m_e & \dots \\ \vdots & \vdots & \vdots & \ddots \end{pmatrix} \tag{2.27}$$

and

$$\mathcal{K} = \begin{pmatrix} \frac{1}{C} & \frac{2e\beta x_{1,\mathrm{eq}}}{C} & \frac{2e\beta x_{2,\mathrm{eq}}}{C} & \frac{2e\beta x_{3,\mathrm{eq}}}{C} & \dots \\ \frac{2e\beta x_{1,\mathrm{eq}}}{C} & ek_{\mathrm{trap}} + \sum_{j\neq 1} k_{1j} & -k_{12} & -k_{13} & \dots \\ \frac{2e\beta x_{2,\mathrm{eq}}}{C} & -k_{21} & ek_{\mathrm{trap}} + \sum_{j\neq 2} k_{2j} & -k_{23} & \dots \\ \frac{2e\beta x_{3,\mathrm{eq}}}{C} & -k_{31} & -k_{32} & ek_{\mathrm{trap}} + \sum_{j\neq 3} k_{3j} & \dots \\ \vdots & \vdots & \vdots & \vdots & \ddots \end{pmatrix}. \tag{2.28}$$

2.8 Analytical Model of Simple Electron Configurations

With only two rows of electrons inside the channel, it is possible to find the lowest energy configuration analytically. This serves as a good comparison for our numerically simulated electron configurations. Let the transverse direction of the trap be x, then the trap is parabolic along the x direction and flat along y. If we assume no electron loss and only two rows, as we vary the trap bias, only the transverse configuration of the electrons changes. The electron density along the y axis (λ) remains constant.

In the simple geometry depicted in Fig.2.8, the force electron i exerts on its neighbor j along x is

$$F_{x,\,\text{single neighbor}} = \frac{1}{4\pi\epsilon_0}\frac{e^2}{r_{ij}^2}\frac{d}{r_{ij}}. \tag{2.29}$$

Since electron j has another neighbor to the right, the resulting force is close to $2F_{x,ee}$. If

we take into account of the next-nearest neighbor, the total force one electron experiences is

$$F_{x,\text{total}} = \gamma F_{x,\,\text{single neighbor}}, \tag{2.30}$$

where $\gamma \approx 2.08$. Depending on the electron density, γ grows from 2.08 in the sparse limit to around 2.38 in the dense limit where the ensemble transits into 3 rows.

Now to find the equilibrium configuration, we have

$$-F_{x,\text{trap}} = \gamma F_{x,\,\text{single neighbor}}. \tag{2.31}$$

Note that the x-location of the electrons is measured from the center line, therefore $x = d/2$. We can then rewrite Eq.(2.31) as

$$ek_{\text{trap}}\frac{d}{2} = \frac{\gamma e^2}{4\pi\epsilon_0}\frac{1}{(1/\lambda)^2 + d^2}\frac{d}{r_{ij}}. \tag{2.32}$$

Here k_{trap} is the curvature of the trap, which grows linearly with respect to the trapping bias voltage V_{cp}. For any bias voltage, we can now solve for d in the equilibrium configuration

$$d^2 = \left(\frac{\gamma}{k_{\text{trap}}}\frac{e}{2\pi\epsilon_0}\right)^{2/3} - (1/\lambda)^2. \tag{2.33}$$

In Fig. 2.8 we plot the width of the ensemble for different densities λ.

For simple configurations that have only $1 \sim 2$ rows, we derived the analytical solution of the electrostatic equilibrium configuration. However, as the electron density and the number of rows increase, the total number of interactive terms that need to be taken into account quickly grows to become unmanageable. More importantly, because the trapping potential is more shallow on the side than in the middle, adjacent rows of the electron ensemble are not commensurate. This means when there are more than 2 rows, the electrons cannot form a perfect crystal in a channel with parabolic transverse profile and our analytical solution

breaks down. Therefore, for more than 2 rows we calculate the equilibrium position of the electrons numerically using our molecular dynamics formalism.

2.9 Modeling Electron-Induced Cavity frequency Shift

Using the equation of motion of the constrained electron-cavity coupled system, we can now calculate the electron-induced cavity frequency shift at various bias voltages V_{cp} with different number of electrons N. First, we calculate the normal mode frequency of a simple 2-row electron ensemble, using the analytical solution to the equilibrium configuration (Eq.(2.33)). Then we compare this result with the normal mode frequency calculated from electron configurations obtained using HOOMD. The results are depicted in Fig.2.10.

In Fig.2.10a and 2.10b., we compare the x-locations of the electrons in the ensemble from HOOMD with those from the analytic model. In the analytical model, we only take into account nearest neighbor interactions, such that the geometric parameter γ in Eq.(2.33) is equal to 2.08. Clearly, this results in good agreement in the region where $V_{\text{cp}} > 1.0$V. For lower bias voltages it is energetically more favorable to form three rows instead.

Next we compare the cavity frequency shift for both cases. The cavity frequency shift is obtained by solving the equation of motion, Eq.(2.24). For the analytical model we exploit symmetry to simplify the kinetic matrix $\mathcal{K}$. Therefore, the problem reduces to diagonalizing a 2 x 2 matrix $\mathcal{M}^{-1}\mathcal{K}$, where

$$\mathcal{K} = \begin{pmatrix} \omega_0^2 L & de\beta\omega_0^2 L\sqrt{N} \\ de\beta\omega_0^2 L\sqrt{N} & ek_{\text{trap}} + 2k_{12} \end{pmatrix}. \tag{2.34}$$

Here $\omega_0 = \sqrt{1/LC}$ is the resonance frequency of the resonator and $\beta = 0.0733$ m^{-2} from Eq.(2.1).

The results are shown in Figures 2.10c and 2.10d. Again, both plots show good agreement between the analytical model and molecular dynamics simulation. The largest deviation

occurs when the bias voltage is low, where the electron configuration transits from 3 to 2 rows. As expected, the 2-row analytic model no longer describes the correct geometry in this regime.

2.9.1 Comparison with experimental data at higher densities

The electron ensembles encountered in our experiment are much more complicated than the simple cases mentioned above. However, using the molecular dynamics simulation package HOOMD [1], we are able to anneal systems far beyond the simple 2-row case, and solve for the cavity frequency shift using these configurations.

The key observations in our experiment are the smooth change of the cavity frequency shift during the bias voltage sweep, and the sharp jumps corresponding to irreversible electron loss from the trap. In our numerical model, we are able to replicate both of these phenomena by calculating the cavity frequency shift for each point in our V_{cp} sweep, and for various number of electrons N in the trap. For each curve in Fig. 2.11, we do not rescale the x or y axis nor is there any offset applied. The only free parameter is N. By comparing the simulation with the experimental data, we are able to estimate how many electrons are present for each trace in the experiment shown in the main text. The four curves that match the experimental data have $N = 0.61 \times 10^5$, $N = 1.09 \times 10^5$, $N = 1.70 \times 10^5$ and $N = 2.43 \times 10^5$.

In the experiment, an important observation is the loss of electrons from the trap. With the equilibrium positions, such a process can be simulated. Let us assume there is a leak in the trap with a threshold voltage V_{leak} that is independent of the trap bias. If the screened potential (Fig. 2.12) that an electron feels is higher than this threshold voltage, it is energetically more favorable for this electron to leak out of the trap. Hence the configuration is unstable. To determine the threshold voltage, we compute the screened potential for all electrons in each configuration. Then we find the threshold voltage that produces the best

fit to the experimental data.

The actual value of the leak voltage determines the starting point of each of the curves in Fig. 2.11. A leak voltage of 530 mV gives the best fit to the data, shown in Fig. 2.13.

2.9.2 Normal Modes And Coupling Strength

The same normal mode solution to the electron-cavity coupled system also gives access to the relevant modes in the electron subsystem. By picking the ten most strongly coupled electron modes, we can estimate the electron normal mode frequency during the voltage sweep.

In Fig.2.14a we plot the normal mode frequency of the trapped electrons. For most $V_{\rm cp}$ the electron mode frequency is tens of GHz, indicating that we are working in the dispersive limit. In this limit the cavity shift is given by $Ng_{\rm rms}^2/\Delta$, where $g_{\rm rms}$ is the rms electron-cavity coupling and Δ is the frequency difference between the electron normal mode and the cavity resonance. A closer look at the electron mode evolution for $N = 0.61 \times 10^5$ reveals an interesting feature. For this curve, the electron density is low enough to support only 1 or 2 rows of electrons. As we increase the bias voltage, the electron normal mode initially grows as $\sqrt{V_{\rm cp}}$, but rolls off as the angle θ between each electron and its nearest neighbor approaches $\pi/2$ (see Fig.2.8). At $\theta = \pi/2$ the electrons form a single row such that the coupling to the cavity vanishes. The voltage at which this happens is determined by the electron density λ and can be modeled precisely with our analytical model.

For higher N, where there are more than 2 electron rows, the electron normal modes evolve mostly as $\sqrt{V_{\rm cp}}$. Minor row-reconfigurations occur, which result in small jumps in the normal mode frequency.

Using the fact that we are in the dispersive limit, we can now look at the rms coupling per electron at different $V_{\rm cp}$ and different N. This is depicted in Fig.2.14b. In general, the coupling per electron decreases as the bias voltage increases and higher N leads to a higher overall coupling. Upon further analysis, we found that this trend is mostly due to the linear

relationship between the location of an individual electron and its coupling to the cavity. In our normal mode solution, for an electron located at a equilibrium position $x_{i,\mathrm{eq}}$, the coupling term between the electron and a single photon excitation in the cavity is

$$\frac{2e\beta x_{i,\mathrm{eq}}}{C}.$$

If we plot the rms coupling per electron as a function of the overall ensemble width, the relationship is roughly linear for constant N, while ensembles with more rows have a smaller rms coupling.

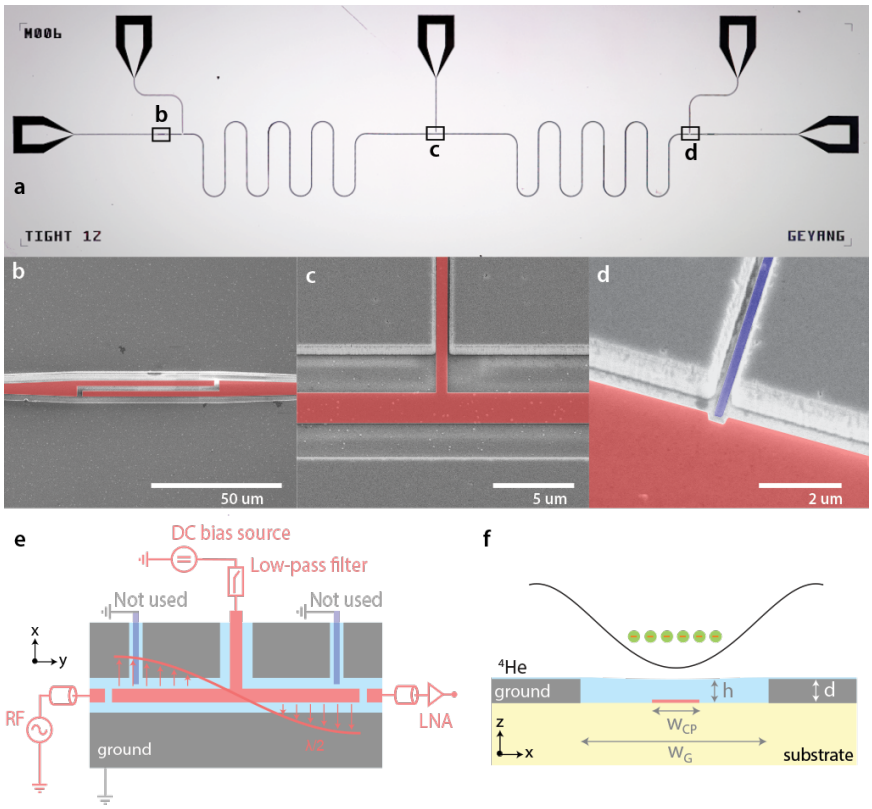

Figure 2.1: **M007 Constricted-Happiness Device, Circuit Schematic and Trap Geometry.** Device, circuit schematic and trap geometry. **a**) Optical and SEM images of a cavity-electron ensemble trap on a 2×7mm superconducting chip. The device is positioned 5.5 mm above the bottom of a cylindrical superfluid reservoir of radius $r = 3.175$ mm, mounted in a hermetically-sealed copper box at 25 mK in a dilution refrigerator. **b**) Interdigitated gap capacitors with gap width 2 μm at the cavity input. **c**) DC bias electrode connected directly to the center pin of the cavity at a node of the standing wave voltage distribution of the fundamental mode. **d**) Sub-μm-size electron trap near voltage maximum of the fundamental mode with constriction of width 500nm. **e**) Circuit schematic showing the voltage distribution of the fundamental mode (red) and the simplified measurement and control circuit connected to the center pin (pink). The cavity is measured in transmission using a low-noise amplifier and the trap potential is tuned through a DC source connected to the center pin (pink) through a low-pass filter. **f**) Cross-sectional view of the cavity waveguide gap showing the schematic trap geometry. The ground planes (gray) form a micro-channel of height $d = 800$ nm and width $w_G = 6\,\mu$m filled with superfluid ^{4}He by capillary action. A DC voltage on the submerged center pin (pink) of width $w_{CP} = 2\,\mu$m and thickness $t = 80$ nm creates a parabolic trapping potential for electrons above the surface which couple to the RF field in the cavity.

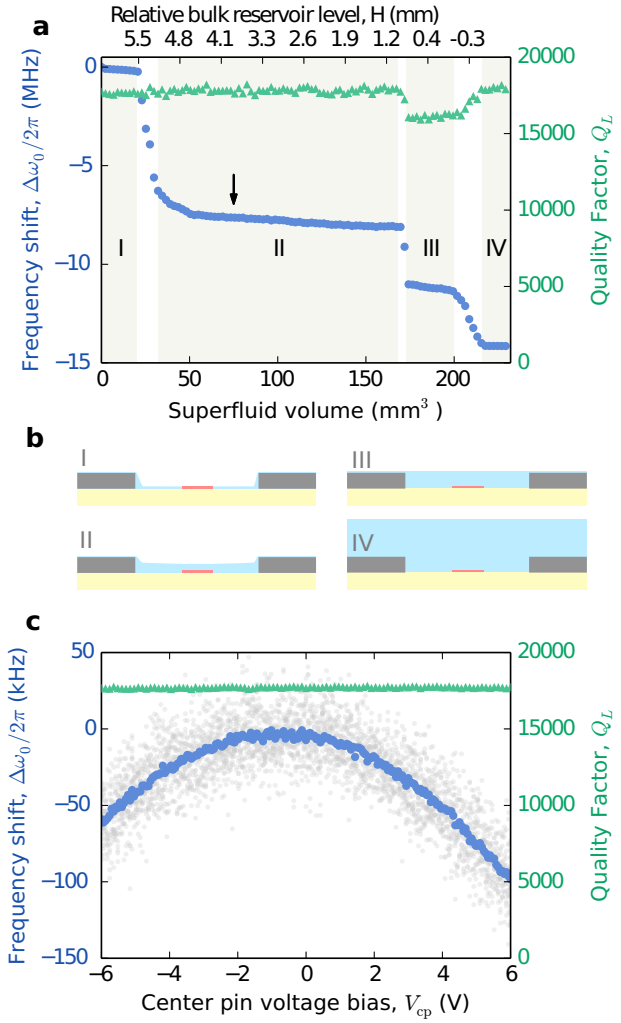

Figure 2.2: **Helium Level Meter Experiment.** Cavity response to superfluid helium. **a**, Measured resonance frequency shifts $\Delta\omega_0/2\pi$ (blue dots, left axis) and loaded quality factor Q_L (green triangles, right axis) as functions of superfluid volume supplied to the cell (bottom axis) and relative bulk helium level H in the reservoir (top axis). Each datapoint corresponds to an increase in superfluid volume of $\Delta V_{\mathrm{sf}} \sim 2.3$ mm^3 and reservoir level $\Delta H \sim 70\,\mu$m. **b**, different filling state corresponding to the different regimes in **a**. **c**, Frequency shift (blue dots, left axis) and quality factor (green triangles, right axis) as functions of center pin voltage bias V_{cp} at fixed helium level in the capillary action regime indicated by arrow in **a**. Gray dots are frequency shifts extracted from single-shot cavity transmission measurements with $N = 80$ such measurements per voltage bias point V_{cp}. The blue data points are averages over the single-shot measurements at each point.

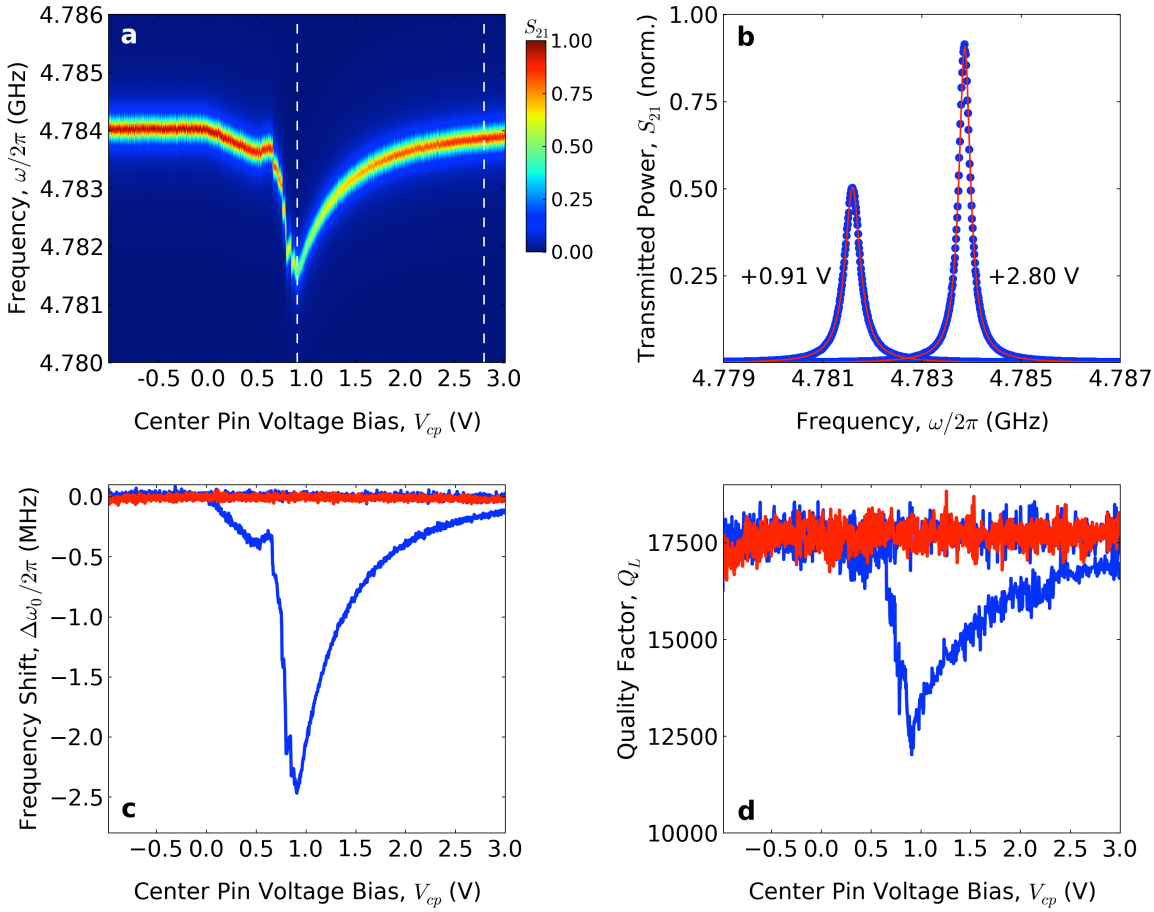

Figure 2.3: **Cavity Dispersive Measurement.** Detection of a trapped electron ensemble on super-fluid helium in a cavity transmission experiment. **a**, Normalized transmitted power through the cavity as a function of center pin trap voltage $V_{\rm cp}$. **b**, Normalized transmission spectra at $V_{\rm cp} = +0.91$ V and $+2.8$ V, showing a shift in resonance frequency and a reduction in transmitted power at the bias points indicated by the dashed vertical lines in **a**. Solid red lines are fits to Lorentzians. **c,d**, Resonance frequency (**c**) and loaded quality factor (**d**) as functions of trap bias in the presence (blue) and absence (red) of an electron ensemble. In Figs. **a** - **d**, electrons are first loaded into the cavity mode volume at an initial bias of $V_{\rm cp} = +3$V and a fixed helium level in the capillary regime with an uncharged shift of $\Delta\omega_0/2\pi = -7.58$ MHz and a reservoir level of $H \simeq 4$ mm. The blue line shows the trap voltage being swept from +3 to -1V and back in 4 mV steps, eventually depleting the trap region, while the red line shows the same sweep for an empty trap.

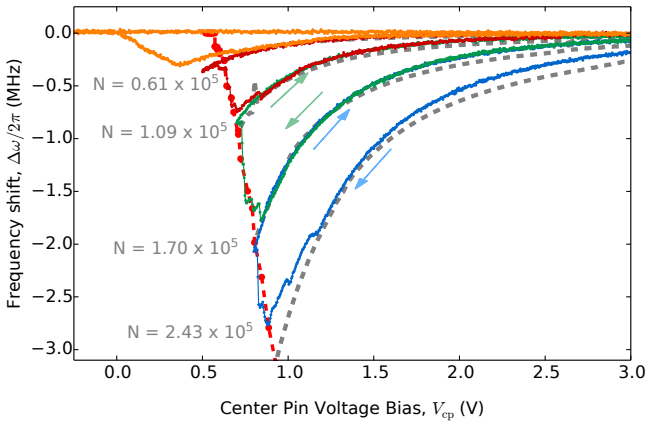

Figure 2.4: **Cavity Frequency Shift vs Trap Bias Voltage.** Measured cavity frequency shifts as a function of trap voltage bias V_{cp}. Colors indicate consecutive cycles of the voltage sweep. In each cycle V_{cp} is decreased (arrows) until electrons are irreversibly lost from the trap and then increased to the initial value of 3.0 V. Gray dashed lines in the background show frequency shifts predicted by molecular dynamics simulation. For each of the four iso-electron number curves the number of electrons in the simulation is depicted to the left. A red dotted line indicates modeled electron loss with respect to a leak voltage of 530 mV. The iso-electron number curves from the experiment terminate within a small neighborhood of this loss frontier.

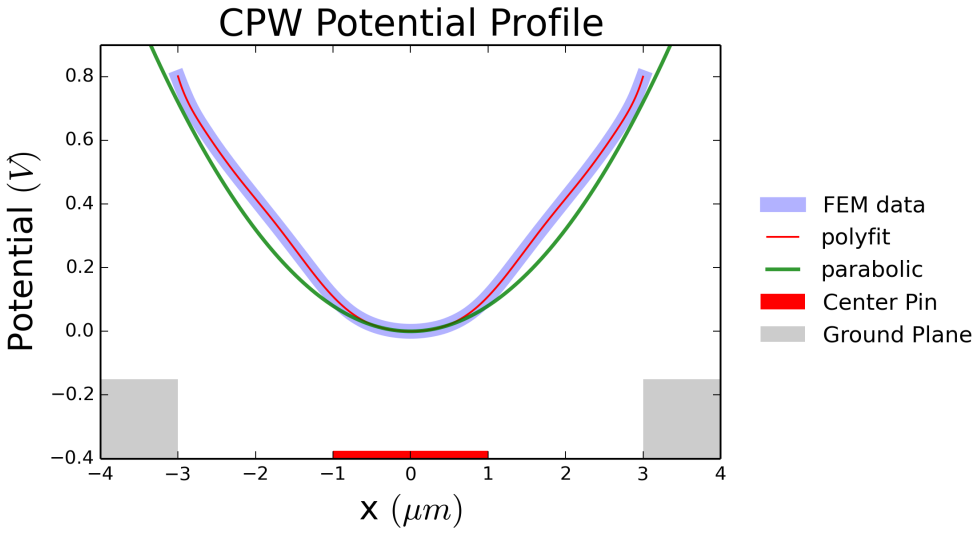

Figure 2.5: **CPW Trap Potential Profile.** Potential profile of the trap, showing the original numerical profile derived from a finite element simulation model; a polynomial fit, and a parabolic approximation using the second order term of the polynomial fit.

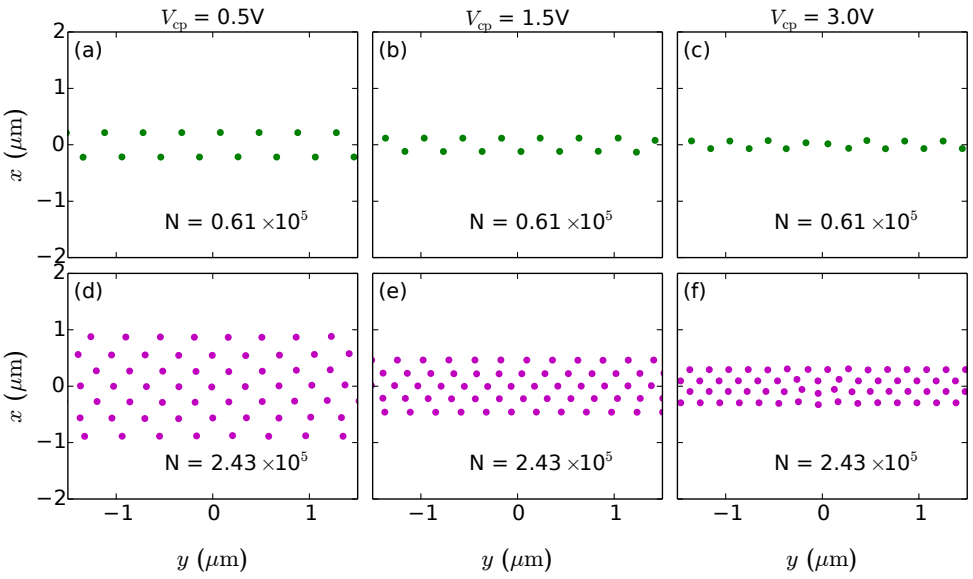

Figure 2.6: **Examples of Electron Configuration.** Examples of electron configurations obtained by molecular dynamics simulations. (a)-(c) Equilibrium electron configurations for $N = 0.61 \times 10^5$ electrons on the resonator as the bias voltage is increased from 0.5V, 1.5V to 3.0V, respectively. (d)-(f) Same as in (a)-(c) but for $N = 2.43 \times 10^5$.

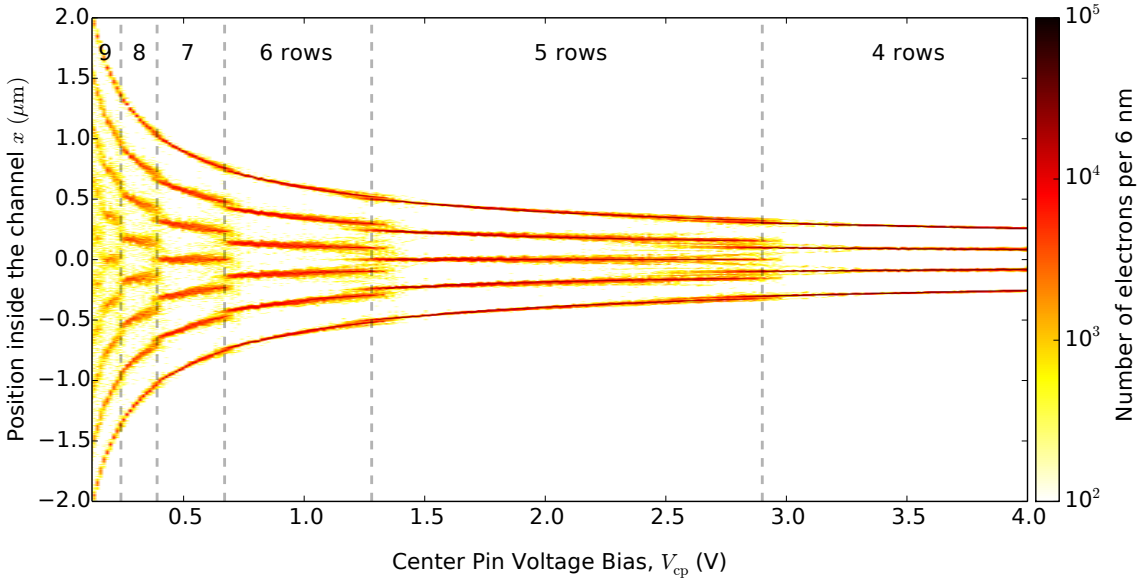

Figure 2.7: **Electron Density w.r.t. Cross-section.** Integrated electron distribution for a large number of electrons on the resonator: $N = 2.43 \cdot 10^5$. For each bias voltage the density along the x-axis was obtained by integrating the electron distribution along y. Gray dashed lines indicate transitions that lead to configurations with one fewer row.

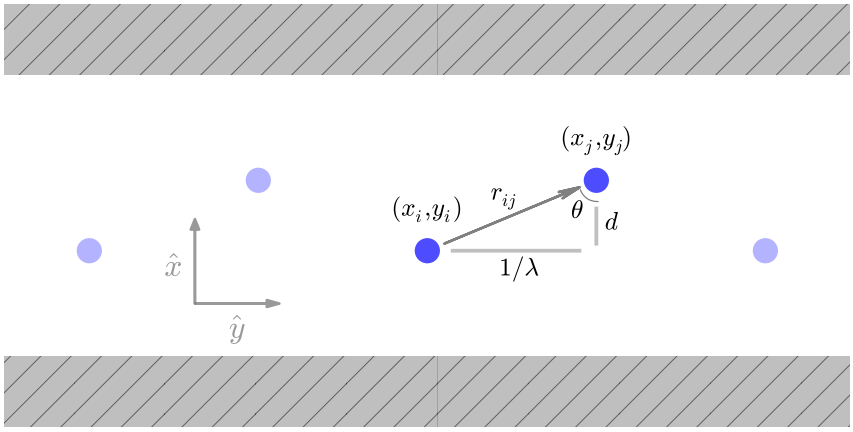

Figure 2.8: **2D Electrons On The Surface of Helium** Schematic representation of two nearby interacting electrons located at (x_i, y_i) and (x_j, y_j). The distance between the two electrons is given by $|\mathbf{r}_i - \mathbf{r}_j| = r_{ij}$. The angle between the line that connects the two charges and the x-axis is θ_{ij}. Here the trap confines electrons along the x-axis. The electron spacing along the y-direction is $\frac{1}{\lambda}$ and finally the row spacing is d. Note that this figure is not to scale.

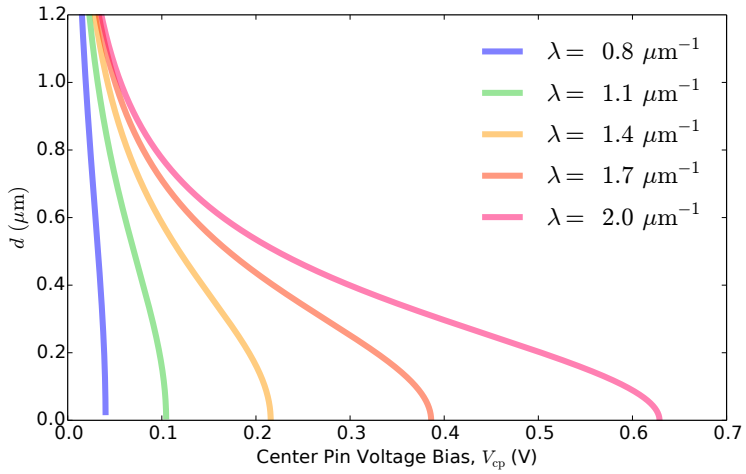

Figure 2.9: **Electron Ensemble Width vs $V_{coupler}$** Electron Ensemble Width Vs $V_{coupler}$ 2-row ensemble width as a function of trap bias voltage V_{cp} at various electron densities. An electron density of λ =0.8 (2.0) μm^{-1} corresponds to $N = 9.7 \times 10^3$ ($N = 2.4 \times 10^4$) electrons on the resonator.

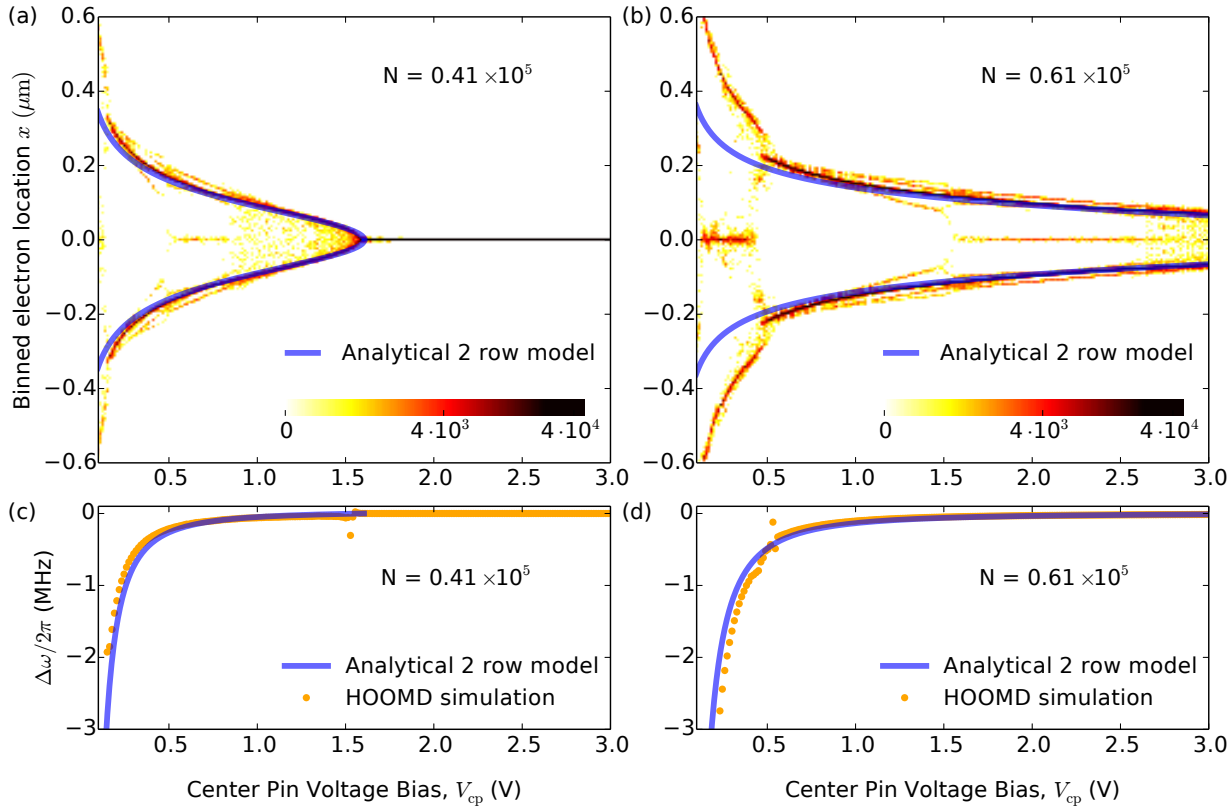

Figure 2.10: **Analytical Model vs Numerical Simulation** Comparison between the analytical model and the molecular dynamics simulation for two different numbers of trapped electrons: $N = 0.41 \cdot 10^5$ (left column) and $N = 0.61 \cdot 10^5$ (right column). Top: binned electron density (bin size = 6 nm) as a function of x via HOOMD simulation (color in the background) and calculated width of a two row electron configuration obtained from the analytic model (blue). Note that there is no free parameter. Bottom: Cavity frequency shift solved numerically (with HOOMD, orange dots) and analytically (blue). In the analytical solution, a simplified version of the equations of motion was used.

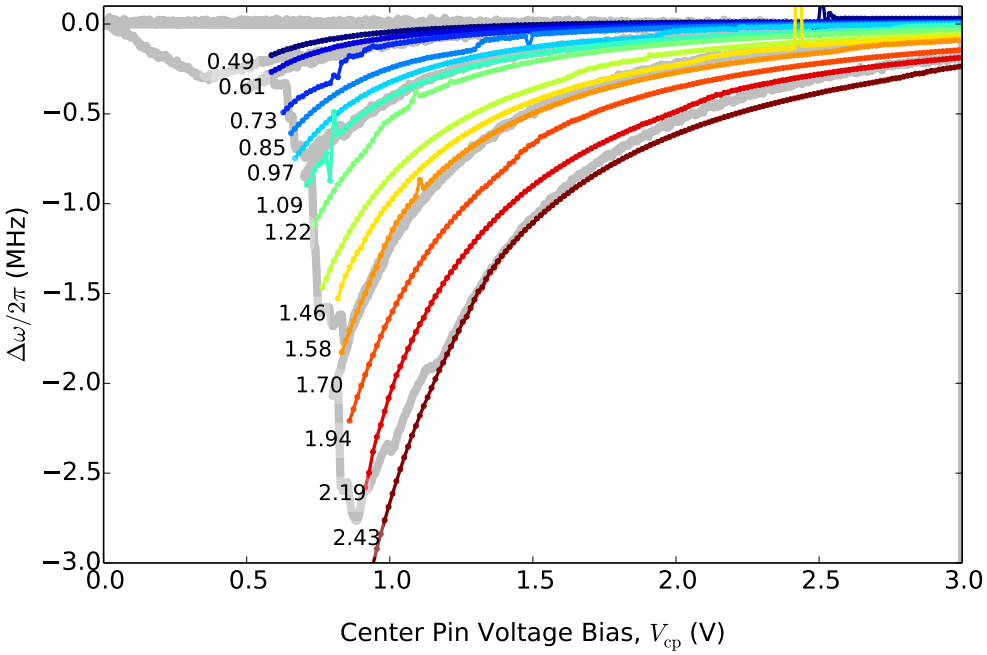

Figure 2.11: **Experiment with All Simulation** Comparison of the measured cavity shift (gray) to the simulated cavity shift (color). The number of electrons in the simulation was increased from $N = 0.49 \times 10^5$ (blue curve) to $N = 2.43 \times 10^5$. For the intermediate curves the number of electrons N (in units of 10^5) is depicted next to each curve.

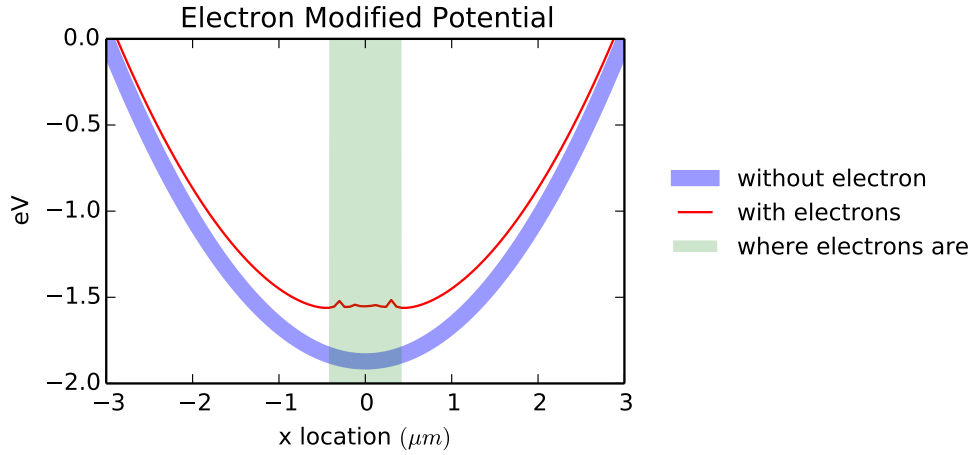

Figure 2.12: **Modified Trap Potential** Comparision between the trap potential (light blue) and the screened potential when electrons are present (red). A green rectangle in the middle shows where the electrons appear. The rugged shape of the screened potential is due to the discreteness of the electron configuration.

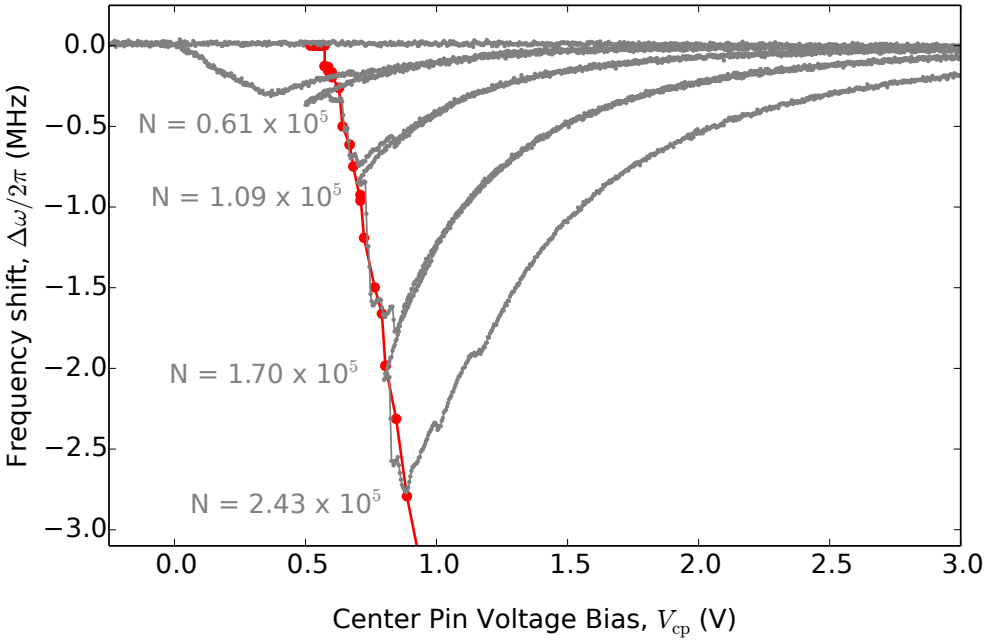

Figure 2.13: **Frequency Shift Hysteresis with Loss** Loss frontier calculated using $V_{\text{leak}} = 530$ mV. The model fits well with the hysteresis data until the electron ensemble is reduced down to mostly a single row in the trap.

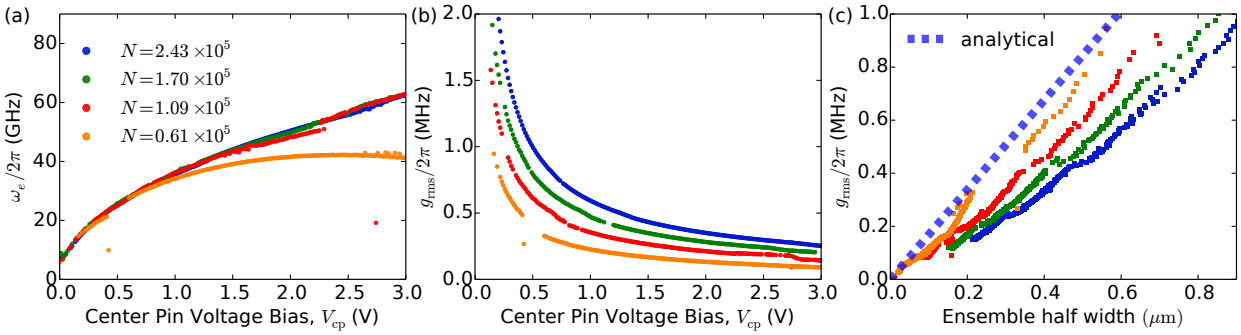

Figure 2.14: **Electron Normal Mode and Coupling** (a): Electron normal mode frequency for $N = 0.61\times10^5$ (orange), $N = 1.09\times10^5$ (red), $N = 1.70\times10^5$ (green) and $N = 2.43\times10^5$ (blue). (b): rms coupling per electron for different values of N. Same color coding as in (a). (c): rms coupling per electron plotted as a function of the electron configuration width. Same color coding as in (a). Small gaps in the solution appear for V_{cp} that correspond to row transitions. For these points the unstable equilibrium configuration results in solutions where a small fraction of the electrons has a disproportionate displacement.

CHAPTER 3

FROM MANY TO ONE

Experiments from the previous chapter (2) focused on the many-body physics involving a large ensemble of electrons coupled to a co-planar wave guide resonator. In this chapter, we introduce a new microwave resonator design with the Trident sample. The *tuning-fork resonator* opened the door to a much smaller quantum dot with just a handful of electrons.

This effort span the years from early 2013 when we started our first design and fabrication iteration on the "Trident" sample, till February 2019. The last part of this work (M018 Yggdrasil) is a collaboration with my lab mate Gerwin Koolstra, with him taking over the experimentation completely from late 2017 when my research focus shifted fully into machine learning. I first saw the sign of a small wigner crystal forming in the small trap on the Trident sample in the spring of 2014. It wasn't until two years later, that the ensemble result in the previous chapter appeared in PRX. The trident result never appeared in publication except a number of talks I gave at march meetings, and the material in this chapter are collection from these talks during this period.

The results on "Yggdrasil", which contains a much more sophisticated dot design, is now available as a report on ArXiv [17].

3.1 Moving Away From Symmetric Waveguide Resonators

the resonator design in M7 Constricted Happiness inherits the standard symmetric co-planner waveguide design that is in wide use with solid state qubits at that time. One of the key constraint with this design is that the DC bias pin for the center pin of the resonator has to be in the middle, where the node for the resonance mode is. When there is an offset between the DC bias pin's placement and the node, the coupling between the microwave photon and the lossy, 50-Ω impedance increases linearly. Unpublished data from [11] show that even

with extensive iterations and precise lithography, it is impractical to expect asymmetric co-planner waveguides to attain high quality factor. The resonator has to be either completely symmetric, or of a different design.

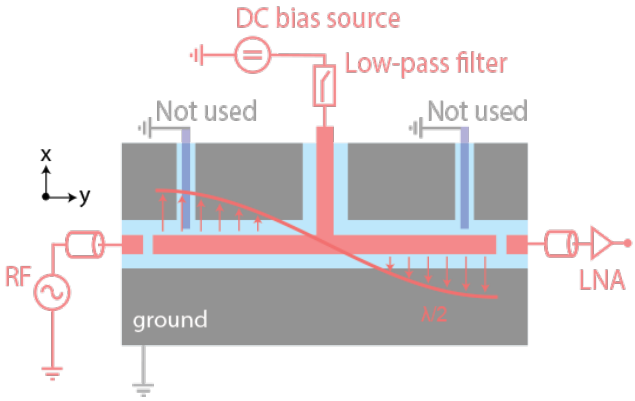

Figure 3.1: **Schematics of A Co-planar waveguide resonator.** M7 has traps on both sides of the resonator to maintain the symmetry. This makes it hard to scale up trap design to more complex electrostatic controls.

This symmetry constraint in the standard CPW (Co-Planar Waveguide) geometry makes it difficult to embed a single electron trap. In order to maintain the symmetry of the cavity, one has to place the same electron trap on both ends. For this reason, the first generation EonHe sample had two traps. To reduce the design and fabrication complexity, it had only one trap bias electrode for each.

This limit in the number of control electrodes for the trap, coupled with complex micro-fluid environment for the trap design, made it impossible to effectively experiment with electrons in this trap. We quickly gave up after the M7 sample went into the fridge. Instead, we decided to focus on the ensemble measurement, which is covered in detail by the previous chapter.

Much of the effort where spent on simulating the trap electrostatically, and making sure that the trap center pin is fabricated successfully in-between two thick niobium walls. Now with the benefit of hindsight, this is a poor design decision. For one the trap is placed at an awkward position at the interface between a thick ground plan and a micro-channel, making it hard to model the combined effect of image changes in the side wall and of the microfluid. In addition, the channel around the bias line is too narrow, making both the

second layer lithography and the lift-off difficult. Electrically it was also difficult to maintain good isolation. So not surprisingly the yield was poor. Only 3 samples came out with isolated trap pins out of 60 dies on a 2 inch wafer, and non of trap produced any result.

3.2 Introducing the Tuning-Fork Resonator Design

In this chapter, we introduce the tuning-fork resonator geometry. To reduce loss, we maintain the symmetry requirement on the placement of the DC electrode by bending resonator around the center point. The capacitive coupling between the two arms of the resonator now dominates, forming a strip-line waveguide. we refer to this strip-line, quarter wave resonator design the "tuning-fork".

This tuning-fork design is largely motivated by the desire to find a more accommodating design that would allow us to have more control during experiments on the electrostatic environment in the trap while also maximize the coupling between the electrons and the resonator.

In this design, the in-plane electric field of its primary EM mode is anti-symmetric with an anti-node placed along the center line (see Fig.3.4). In addition the electric field points parallel to the surface of the superfluid helium along the center line. These two factors combined maximizes the coupling between this TEM mode and the electron's in-plane motion.

The number of trap electrodes in the M7 mask is limited, because there were only 8 coaxial connectors available on the octo-box and we did not want to redesign the sample box at that time.

3.3 Sample Architecture

The tuning-fork resonator makes it very easy to integrate a single-electron on helium quantum dot. In the Trident sample, we designed a small electrostatic trap on the open end of the resonator by shaping it slightly wider than the rest of the strip-line. This way, the potential on the end has a natural tendency to be lower than the rest. The depth of the trap is controlled by a DC bias lead coming from the opposite side, protected by a narrow channel. The lead itself is about 125 nm wide, whereas the channel is about two times of

that. Depositing such a narrow wire in between walls that are 800 nm tall with lift-off and e-beam lithography was challenging. Details of the trap can be found in Fig.3.8.

Microwave-wise, we talk to the resonator by with two capacitive coupler near this open end, where the transverse electric field is strong. The overall architecture of the sample design can be found in Fig.3.6. The computer- assisted design (CAD) file can be found in Fig.3.7.

3.4 The Trident Sample

The Trident sample used an innovative hard mask patterning process for the thick niobium ground plane layer. We were able to achieve narrow, high-aspect ratio trenches around the trap and resonator bias line. One of the most challenging issue for the pattern was trying to avoid getting "black silicon", micro-pillars caused by redeposition of the mask material (aluminum) in the channels.

Hard-mask redeposition occurs, when the material used as the hard-mask, which is typically non-soluable in the reactive ion etch plasma environment, is sputtered up and redeposited due to the bombardment of the gas. Fig.3.9 shows the cheese-like surface texture of the ground-plane, which indicates that there were significant loss of the mask during the etch process.

What made debugging this issue particularly difficult is that the sputtering, and the redeposition is proportional to the surface area of the exposed hard-mask. So diagnostic etch runs using only a fraction of an entire wafer is ineffective. Both the etch time and the amount of redeposition with smaller sample sizes are not indicative of the result on full wafers with the same timing, stoichiomecal, and thermal settings. Figuring out that we needed to tweak the process directly on full wafers, and try to limit the sputtering by thickening the resist, were critical.

For details of the fabrication process, and how we solved the redeposition issue with both timing and cryogenic cooling during the etch, please refer to later chapters.

3.5 Loading Electrons

The two DC bias electrodes, together with the ground-planes constitute the electrostatic environment for the trap. The two degrees of freedom allows us to do three things: First, load electrons onto the sample as a whole. Second, transfer some of the electrons from the bulk of the resonator to the small trapping area controlled by the trap electrode. And finally, reduce the overall load of electrons trapped with the sample, to retain only the minimal density to maintain trapping.

3.6 Network Analyzer Setup

The microwave measurement setup of the Trident and Yggdrasil samples saw a few generations of upgrades. We started with a simple network analyzer setup (see 3.11). This turned out to be too slow because the network analyzer can only acquire one single datapoint every second.

Fig.3.12 shows an example of cavity frequency shift due to change in coupling with the electrons in the trap area. As we maintain the same voltage for the resonator, increasing the bias voltage on the trap electrode induces a decrease in the cavity resonance. This figure shows an isolated slice of this response.

To provide a more systematic understanding of the interplay between the two trapping biases for this sample geometry, we surveyed this 2-dimensional control space by plotting the transmission amplitude (and line-width) with respect to the two control biases.

As show in Fig. 3.12, there is a clear trend in the cavity response when the trap voltage crosses the resonator bias voltage minus an offset. This relationship can be described by a

linear model

$$V_{\text{trap}} - V_{\text{resonator}} = V_{\text{offset}}. \tag{3.1}$$

A fit to the diagonal line gives an offset $V_{\text{offset}} \sim -760mV$. On can consider the resonator bias as regulating the potential of electrons atop the reservoir. Then as we decrease the trap bias, the potential inside the small trap decreases, causing the electrons to move into this area. Because the trap area has a different geometry, there are various low frequency modes available to accommodate the electron(s)' lateral motion. The large cliff-like feature corresponds to the cross between these electron modes and the cavity.

Our control (see Fig.3.13a, trace in green) sweeping through the same voltage range without electrons loaded in the resonator shows that these crossings are indeed induced by electrons inside, or close to the trap electrode. The challenge however, is to show definitively that there are just one, or a few electrons inside the trap.

3.7 Fast Homodyne Setup

Fig.3.13 show the response of the cavity resonance shift w.r.t. trap and resonator bias. Because each datapoint is sampled independently, the denoising also need to be done per-datapoint.

With the fast homodyne setup (see Fig.3.14), we can quickly sweep one or both of the two axes. The datapoints that are sampled consecutively are correlated, making it possible to denoise the entire sweep together. In addition the digitization is done in the GHz regime, where the noise floor is lower.

These factors combined improves the signal to noise, and reduces the time it takes to sample.

Fig.3.15 shows the spectrum with a set of contours overlaid on the top. The left sub-figure shows the transmission amplitude and the right shows the phase. One can clearly see

features of a mode-crossing when the trap is bias at 2.3 V.

3.8 Signs of A Single Electron

A close look at such spectrum taken over different resonator voltage and trap voltage shows a trend (see Fig.3.16) where the crossings occur along diagonal lines in the V^2 space.

These spectral measurements can be summarized as a scatter plot. Each avoided crossing is a dot at $(V_{\text{trap}}, V_{\text{res}})$, where the size of the dot corresponds to the width of trap voltage range for the crossing (see Fig.3.17).

The avoided crossings arrange along diagonal lines. Features along the same diagonal line tend to have similar width. This is in agreement with our linear model of the trap.

3.8.1 Discrete Crossings With A Small Wigner Crystal

The slowest step in the full spectrum scan is updating the probing frequency of the generator. Now to go one step further to produce a finer map of the electrons inside the trap, we need to sweep over the entire V^2 space. We park the probing frequency to the side of the cavity resonance (as in Fig.3.12), and monitor the change in transmission amplitude and phase as a proxy for the change in resonance. Figure.3.18, 3.19, and **??** shows the cavity frequency response at increasing levels of zoom.

The foremost feature visible in this map is the zigzag in the middle. These large features are avalanches that occurs when the resonator trapping potential becomes too weak to retain the over-saturated electrons. The electron loss seem to occur catastrophically, with no way of recovering. After the avalanche the residual charges inside the reservoir is low enough that in-order to move electrons to the sensitive part of the trap, the required trap bias voltage is more shallow (smaller in amplitude).

Avalanche occurs a few times during the scan. Towards the end, fine filaments showing very discrete features appear. This occurs at the very lower range of the resonator bias, and

they resemble the mode hopping produced by a handful of electrons.

We can zoom into the map in Fig.3.19 (see Fig.**??**). Cross section of the finger-like features show discrete jumps. In Fig.3.20, the number of modes went from 7 (blue) to 3 (green), 2 (red), 1 (light blue) and a small blimp (purple). Later in [17] Gerwin was able to model these discrete change between electron configurations using a simple analytic model for the trap. The cross-section view shows the discrete rearrangements of the electron-configuration, suggesting there might be only a handful of electrons in the trap.

3.9 From Trident (via Fjolnir) to Yggdrasil

These discrete spectral features is indicative of having just a few electrons near the trap. However, we were not able to completely deplete the reservoir while maintaining trapping inside the trap. In addition, the trap bias is strangely offset from the reservoir by a -790 mV offset.

3.9.1 Improving the Isolation in Yggdrasil

Our design of the new trap in Yggdrasil was mostly concerned about the finite feature size the lithograph and lift-off process can offer. In the final design, the trap electrode is only separated from the resonator by 125 nm. With the benefit of hindsight therefore it is not surprising that we shorted our sample in our first cooldown, with a 12 volt differential between the trap and the resonator bias.

At room temperature, silicon's breakdown field is around $3.0 \times 10^5 V/cm$. In our case we are not sure the exact voltage the breakdown occurred, but 12 volts over $125nm$ is corresponds to a field strength of $10^6 V/cm$, far beyond the breakdown field of silicon at room temperature.

Our solution was to improve the isolation between the trap electrode and the resonator by adding a third etch step, and cut a 700 nm deep trentch in-between. This resulted into a beautiful sample that never had a short in this area. The cross-section of the 3-layer design can be found in Fig.3.24. For the scanning electron microscopy images please refer to the chapter on fabrication.

3.9.2 Future Directions

The electron mode cross-over is blurred by the surface fluctuations of the superfluid helium [17]. To resolve the avoided cross, we need to introduce active and passive damping.

Below are a few ways to accomplish this.

Resistive Damping is a scheme where we introduce loss to the otherwise high-Q acoustic environment by resistively slowing down the electrons' motion with a non-superconducting metal underneath the helium. The electron would induce a positive image charge inside the metal layer, and the resistivity experienced in the thin gold film by this image charge would slow down the electron itself. It is not clear how the superfluid coupled to the electron's thermal motion. In particular the fluctuations that are normal to the surface of the helium.

Active Acoustic Damping is a scheme where we use active piezoelectric elements to damp the vibrations. The challenge in this case is that the piezoelectric components require high voltage (30V)s down at the bottom stage of the dilution refridgerator.

Electrophoriesis Damping is a scheme where we control the amount of the superfluid helium inside the sample box, by applying large voltages across two near-by electrodes. Gerwin attempted this method briefly by integrating a coil capacitor into the pedestal of the sample box.

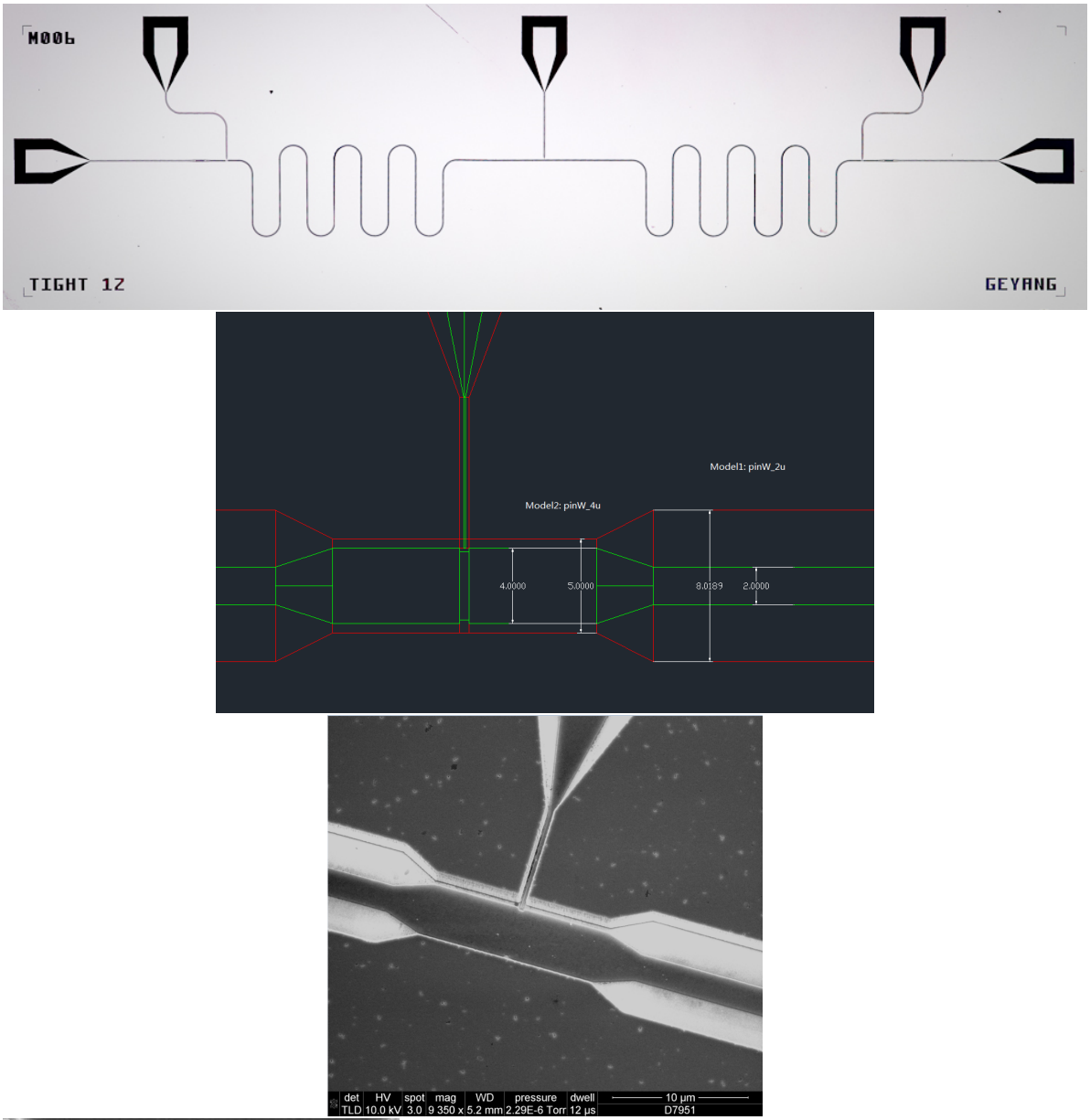

Figure 3.2: **Symmetric CPW Resonator Design. Top**: image of the die. **Mid-left**: design of the trap area. The mask is a two-layer process. Deep reactive-ion etch mask in red, lift-off mask in green. **Mid-right**: electron microscope image of the trap area. **Bottom**: zoomed-in image of the trap, showing details of the micro-channel and the center pin of the trap.

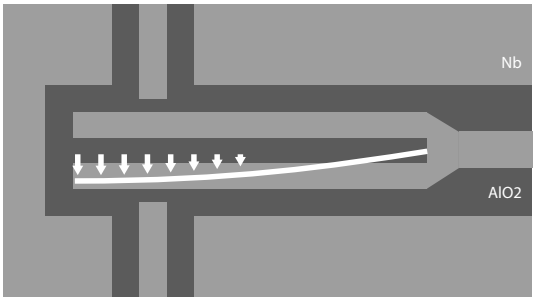

Figure 3.3: **Tuning-fork Resonator Design** showing the transverse microwave field having a larger amplitude on the open end. Two electrodes above and below couple capacitively to the resonator, enabling one to probe the transmission spectrum of the cavity.

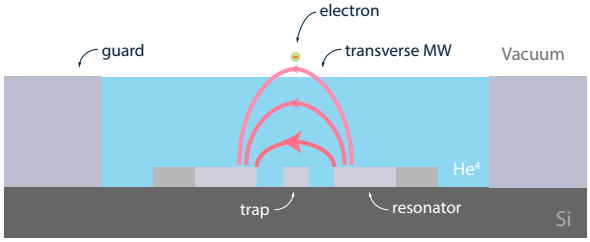

Figure 3.4: **Cross-section View of the Transverse Microwave Field.** between the two pins of the resonator. Along the center line the electric field is parallel to the surface of the super-fluid helium. Depending on the thickness of the helium in the micro-channel, the field decreases in strength.

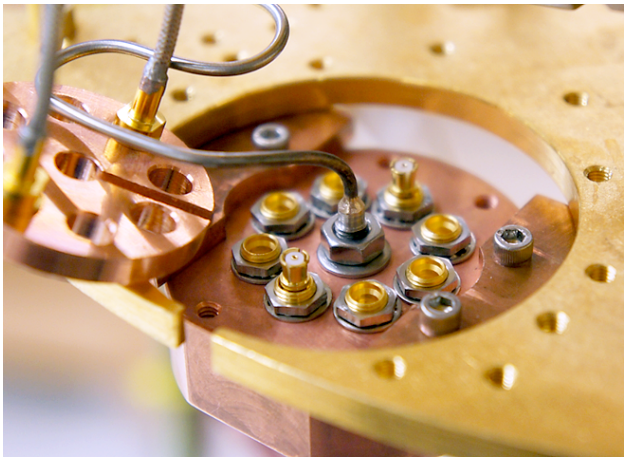

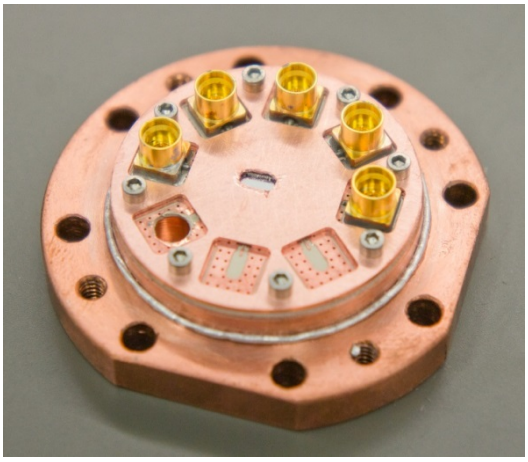

Figure 3.5: **The Octo-box** had only 8 connectors. this limited number of connections was the reason behind our design decision to keep the DC electrode count low in the Trident. In later samples, Gerwin Koolstra's effort in redesigning the sample box with more connectors allowed us to expand the number of controls in M016 Yggdrasil. For the improved design, see Chapter 6.

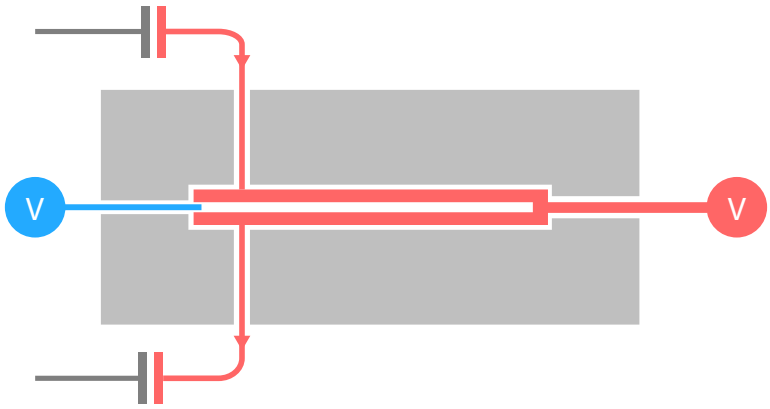

Figure 3.6: **Schematics of the M7 Trident Sample.** The tuning-fork resonator is in red. The main resonator is a quarter-wavelength differential strip-line resonator between thick ground planes that forms the micro-channel for the helium. A small electron trap is integrated to the open end of the resonator, while the shunted end of the resonator is connected to DC bias lead.

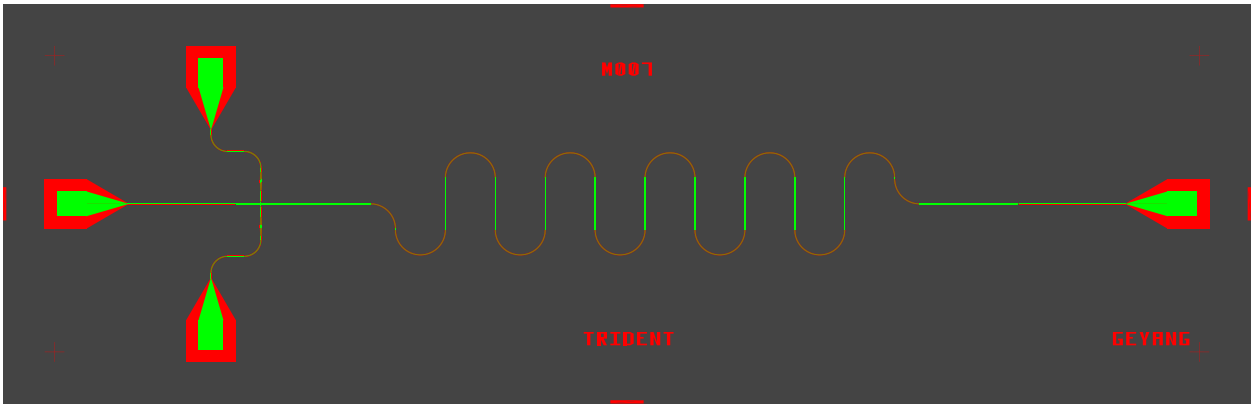

Figure 3.7: **M7 Trident Sample** Two microwave couplers (top and bottom), and two static electrodes: trap electrode on the left, and resonator electrode on the right.

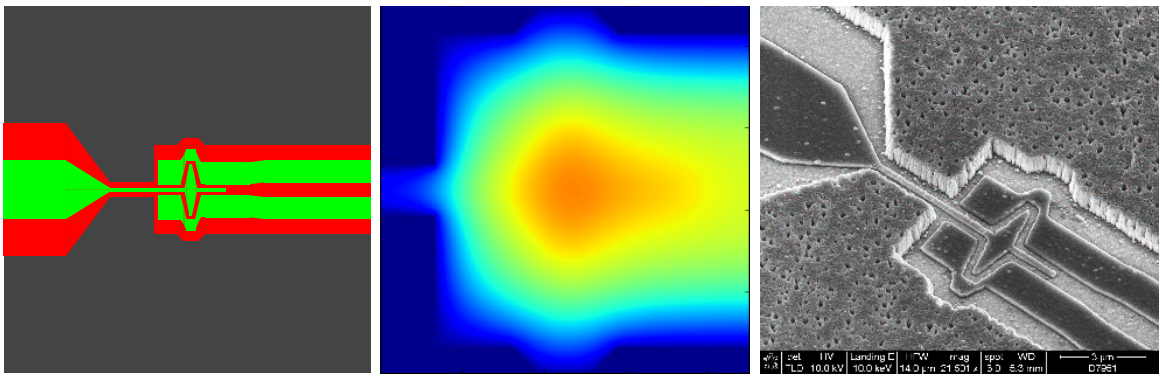

Figure 3.8: **The Trident Sample. Left**: Trident trap design **Middle**: The simulated trap electrostatic potential **Right**: Scanning Electron Microscope image of the trap. The colorbar from red to blue is normalized, with blue color correspond to 0V, and red to 1V.

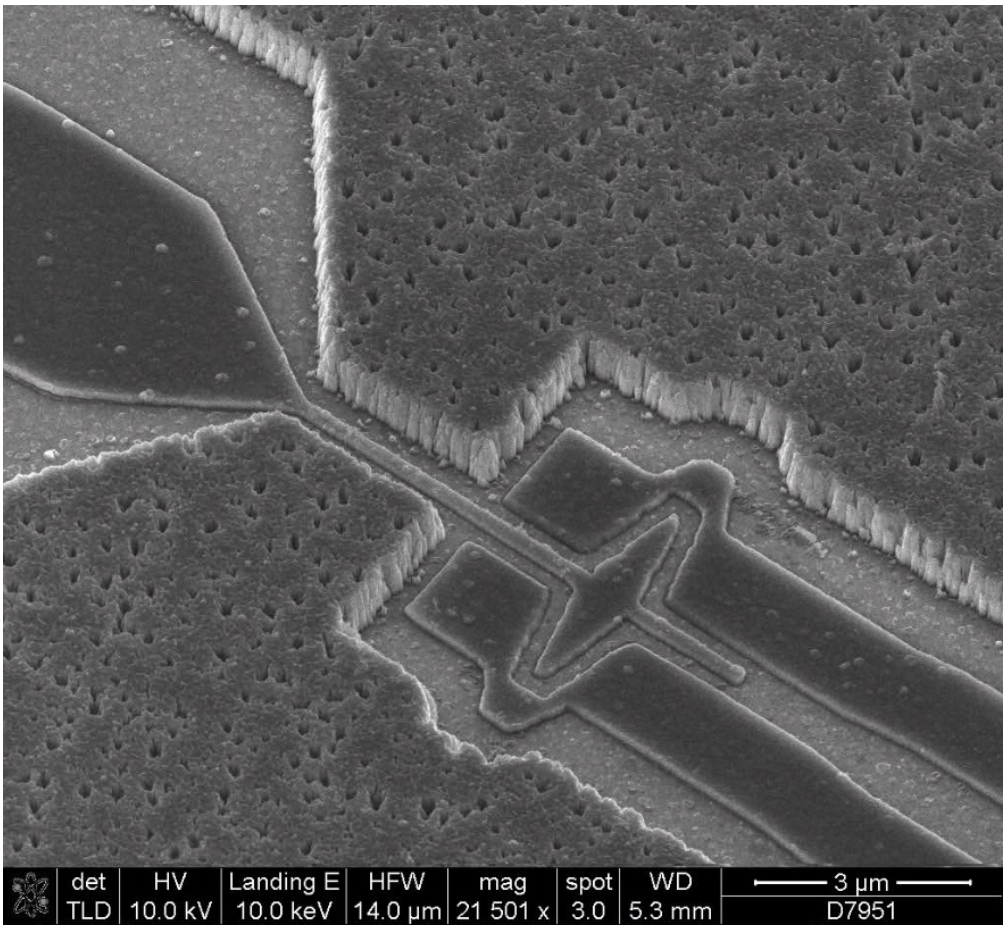

Figure 3.9: **Scanning Electron Microscopy image of the trap on Trident** showing the result of the deep-niobium-etch process. The micro-channel in between the ground planes is etched via deep RIE etch through the 1 um thick niobium ground plane. Cheese like surface texture occurs because the aluminum hard mask end up getting punctured at weaker points, exposing the underlying niobium as well as redepositing into the gap in-between the ground plane. The former results in cheese-like surface on the niobium. The latter results in small but densely-packed pillars, also called "black silicon" due to the low reflectivity for visible light.

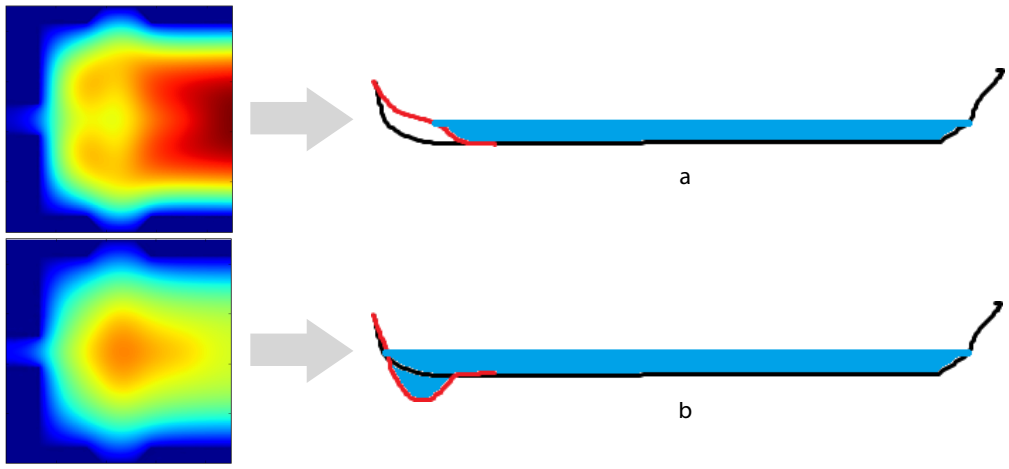

Figure 3.10: **Diagram of the electron occupation over the trap and the reservoir. (a)** shows the electron distribution when the reservoir is more positive than the trap electrode. Electrons prefer to stay over the resonator (reservoir). **(b)** shows the electron distribution over both the trap and the reservoir, when the trap is more positive than the resonator. We hope to reach a regime where the electrons are **only** inside the trap, but due to the limited control in the Trident sample, it is not obvious we could deplete the reservoir while maintaining electrons in the trap.

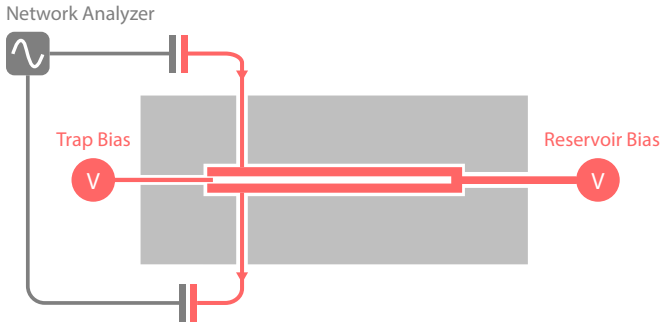

Figure 3.11: **Probing setup with a network analyzer** We record the transmission amplitude and relative phase as the network sweeps across the spectral window. This measurement scheme is slow, allowing us to get a spectral (as in Fig.3.12) every other second. As a result to acquire the bias map in Fig.3.13, took hours.

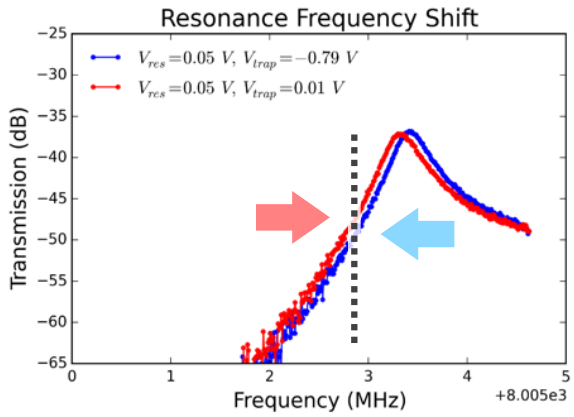

Figure 3.12: Schematics of how transmission amplitude and phase reflect a dispersive shift in the cavity mode. Black dashed line indicates the probing frequency, in this case slightly offset from the peak of the line. When the cavity frequency move due to changes in the coupling, or the number of electrons in the trap, the phase and amplitude of of the transmitted signal also changes.

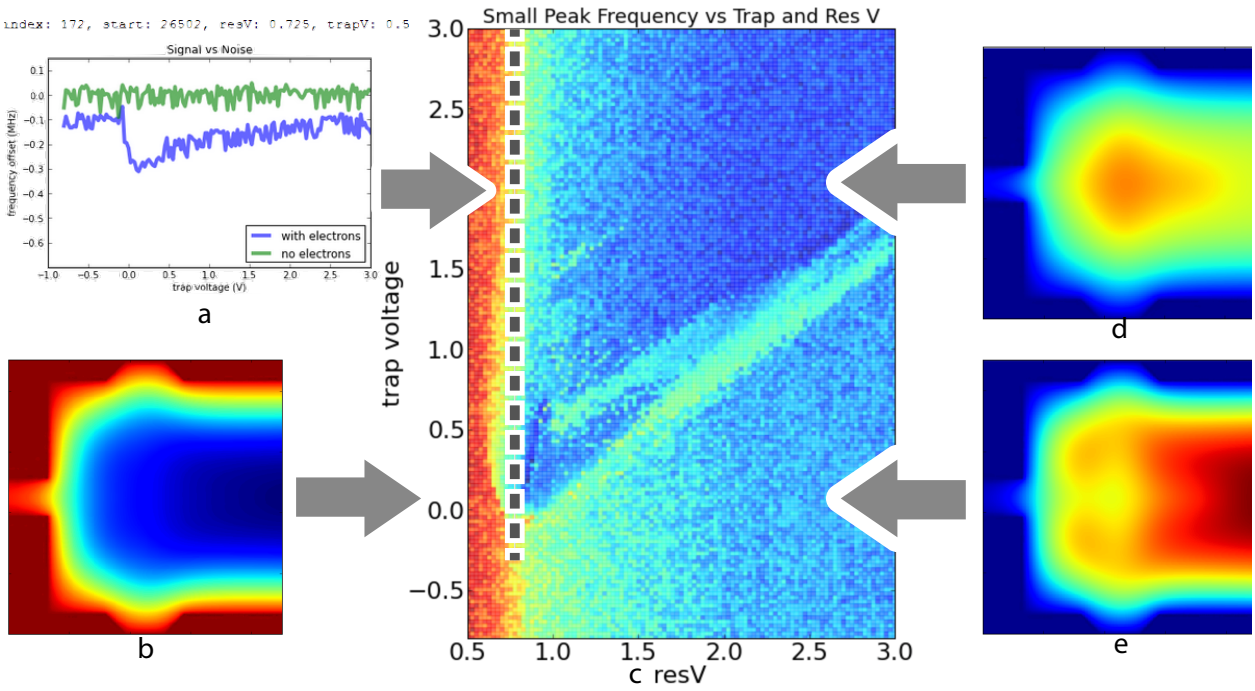

Figure 3.13: **Measurement Result.** **(a)** Cavity resonance frequency shift versus trap voltage at a fixed resonator voltage. Green trace is the control where no electrons are loaded. Blue trace shows the cavity response to unloading of the trap, where the DC bias on the trap electrode is swept down linearly from +3V to -1V. **(b)** showing the simulated trap potential when the reservoir is negative bias, so no electron can be trapped on the sample. **colorbar**: red is 0V, blue is normalized positive potential. **(c)** cavity resonance shift versus trap and reservoir bias voltage. Diagonal features in this dispersion map shows the linear relationship between the trap potential and that of the reservoir. **(d)** simulated trap potential, showing a positive dimple over the trap. This is the region where electrons can be detected inside the trap, potentially forming a small Wigner crystal. **(e)** simulated trap potential, where the reservoir bias is larger than that of the trap, causing the electrons to drain from the trap into the reservoir. (e) and (d) are the regions where we hope to go between loading and unloading the trap, whereas (b) is used as a place to reset the experiment.

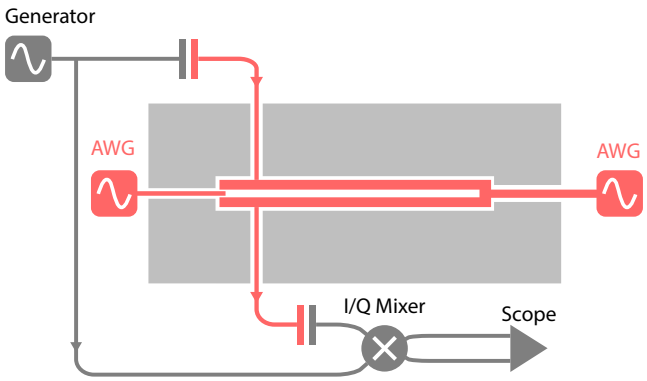

Figure 3.14: **Homodyne Setup for Trident.** The resonator is probed on one side with a generator. The transmitted signal is mixed down with the probing tone, and we digitize the in-phase and quadrature signal with a fast two-channel scope. The homodyne setup allows the cavity frequency-shift to be digitized at a higher rate, where the noise floor is much lower. This improves the signal to noise as well as the sampling rate. Dithering the trap and resonator electrodes at the same time, also using signal generators allows us to measure the cavity/trap quickly.

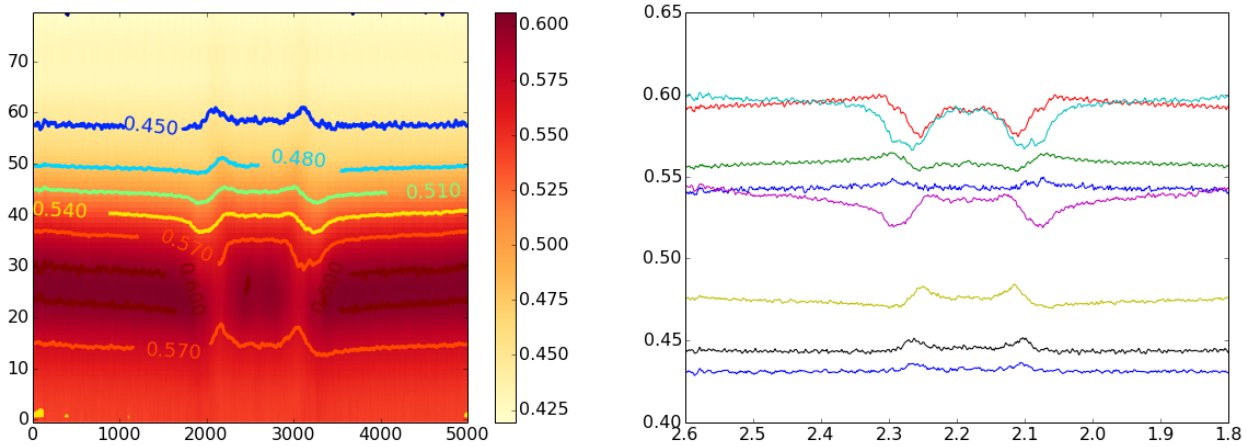

Figure 3.15: **Transmission Amplitude and Q vs V_{trap}.** Horizontal axis for both figures are the trap bias voltage being swept. The trap voltage sweeps down from 2.6 V and reflects at 2.2 V. The left figure shows the transmission amplitude. The right shows the phase. TODO: fix the x-axis

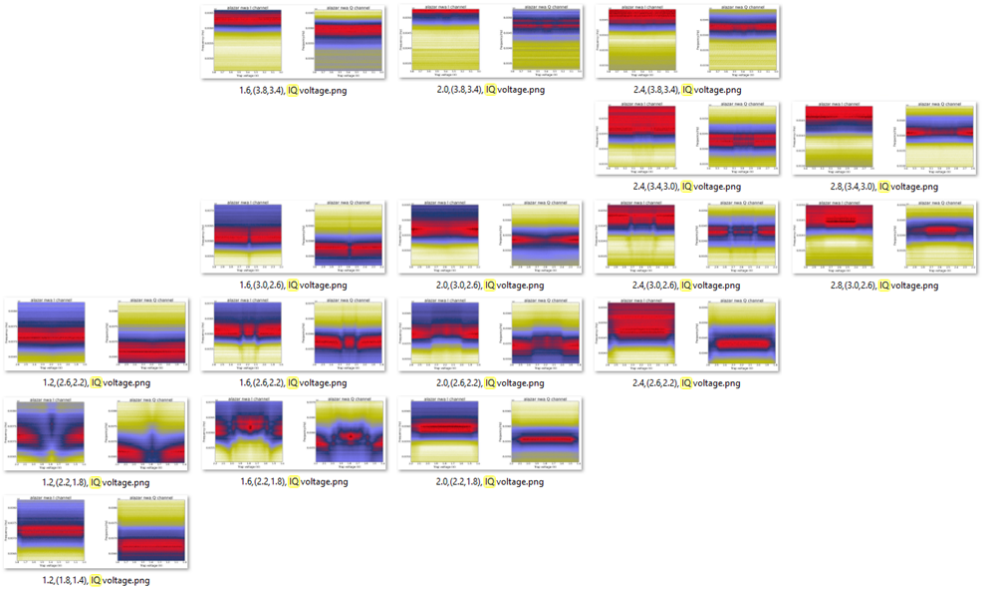

Figure 3.16: **Trend In The Avoided Crossings.** Each figure contain a sub-figure for the transmission amplitude, and one for the phase. Each row correspond to the same resonator bias voltage. Whereas each column corresponds to a different consecutive segment of the trap bias voltage.

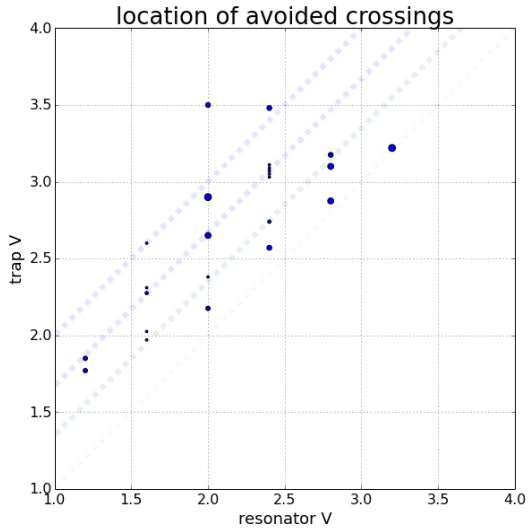

Figure 3.17: **Trident Avoided Crossing Summary.** The size of the dot indicate the width of the crossing. The location indicate the trap-vs-resonator configuration. There are clearly trends for a linear relationship between the two electrodes. And it shows multiple crossing evens as we sweep down the trap bias voltage.

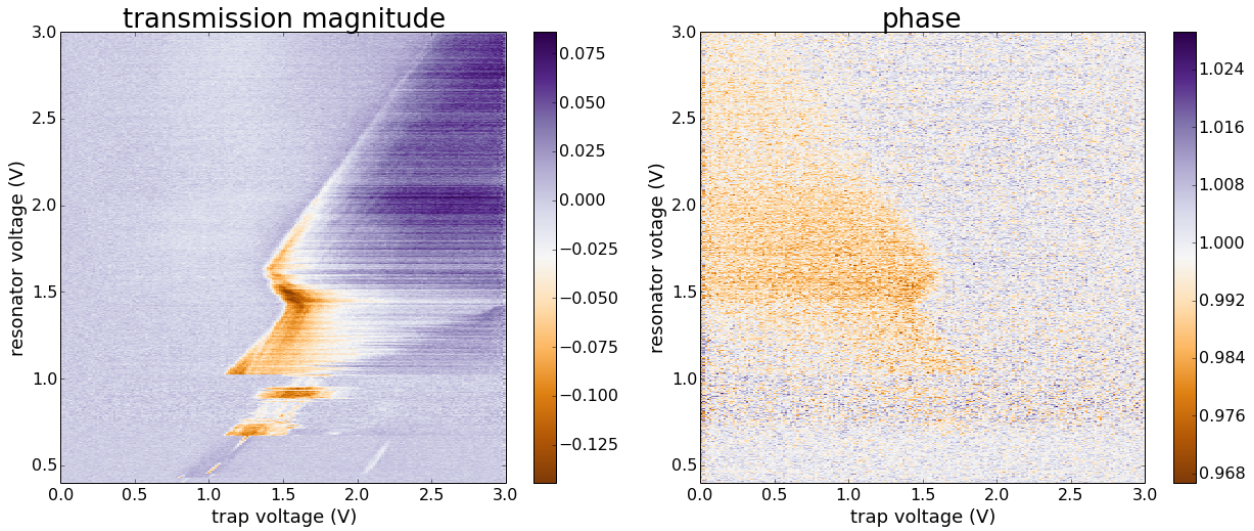

Figure 3.18: **Measuring A Small Wigner Crystal on Yggdrasil**. The data is post-processed by reducing an averaged baseline for each row. This allowed us to produce a much cleaner set of results. The phase plot is reflected by mistake. The original data is gone due to server mishandling.

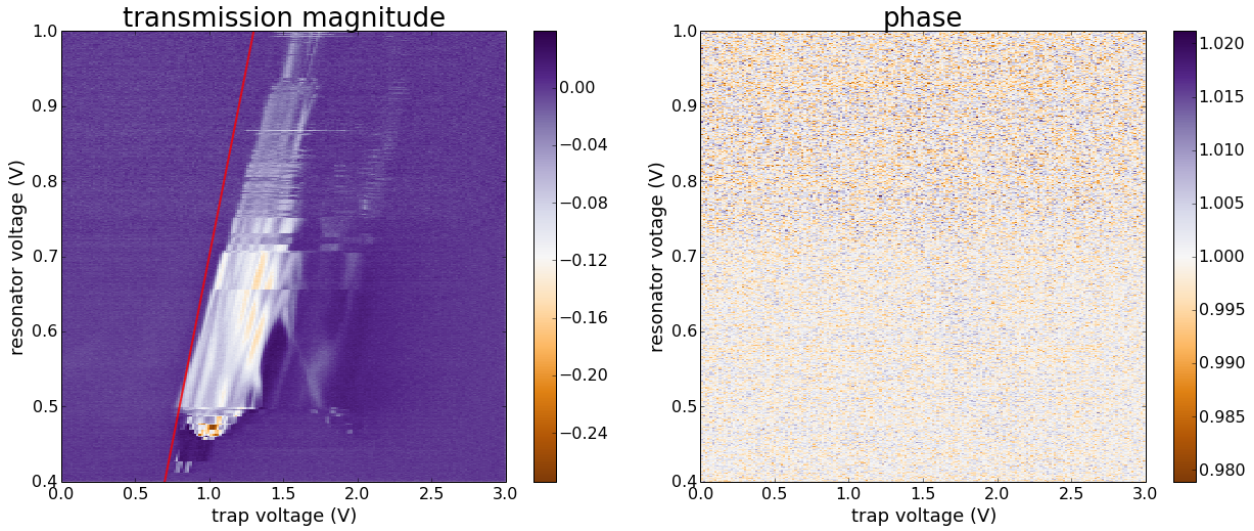

Figure 3.19: **Zoomed-in Map of the Yggdrasil Trap Response**. One can see **1**: various modes are crossing each other. There is a small, discrete number of modes. and the number of modes goes down as the electrons in the resonator is depleted.

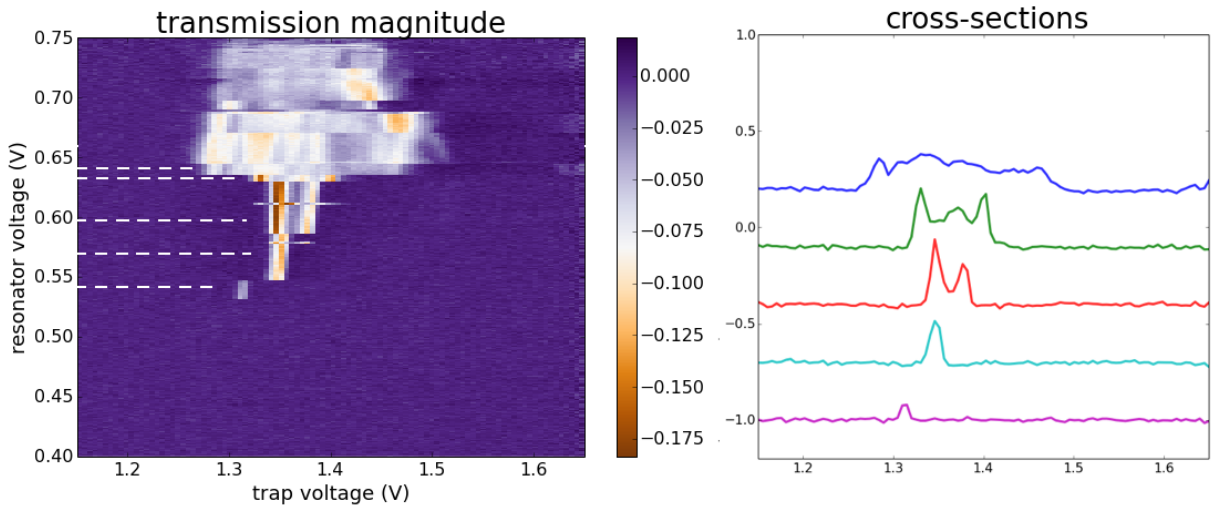

Figure 3.20: **Finger Spectrum and Cross-section Left**: Zoomed-in view of the homodyne resonance map; **Right**: Cross-section of The Finger-like features, showing discrete re-arrangements of the electron configuration.

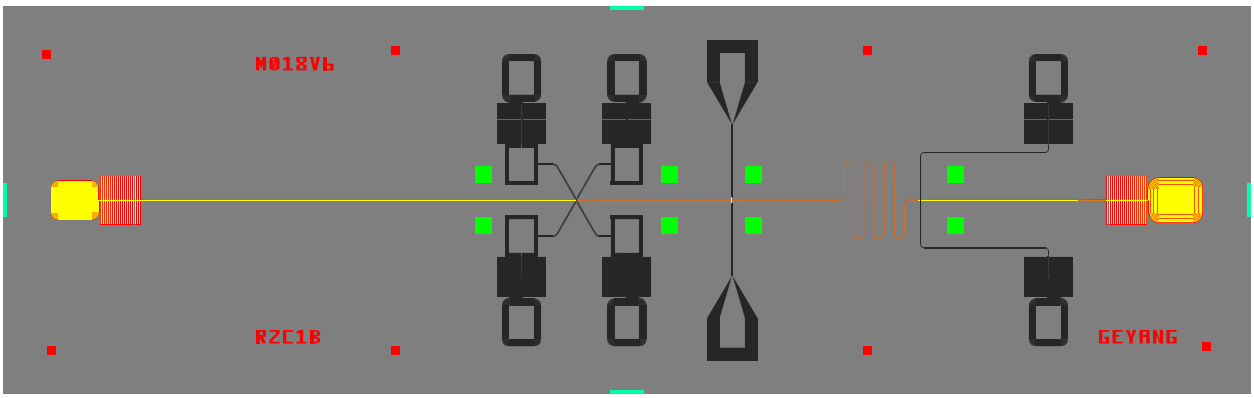

Figure 3.21: CAD design of M018 Yggdrasil V6B. The B-variant has the "bubble-gum" inductors at the end of the center-pin launcher.

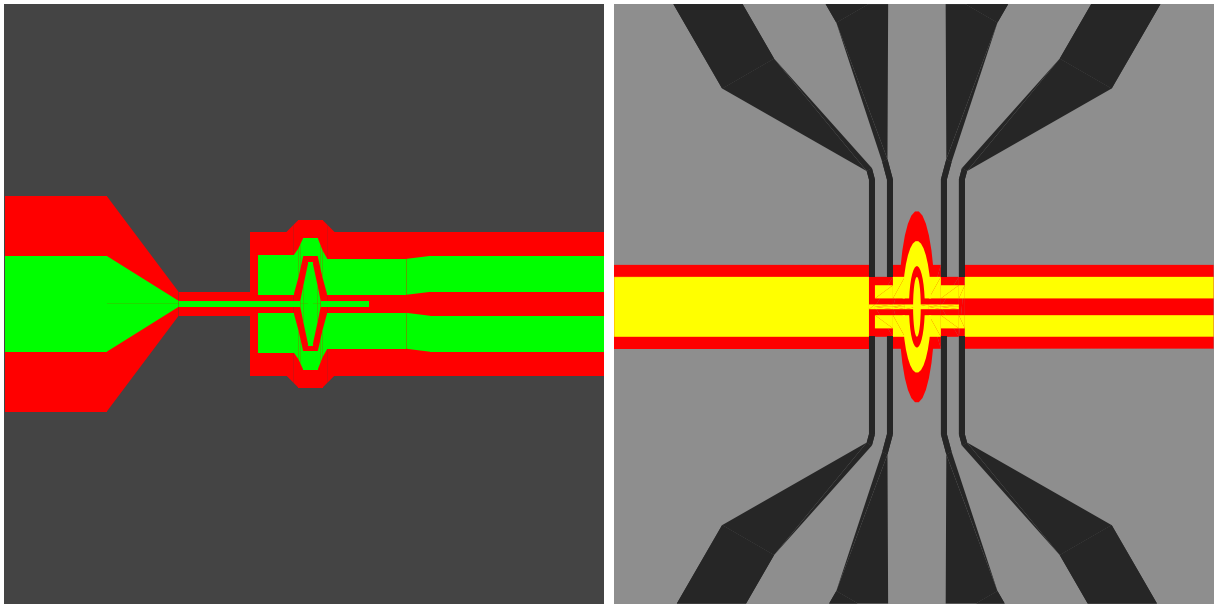

Figure 3.22: **Trident and Yggdrasil Trap design**. **Left**: trap design of M007v5 Trident, the first tuning-fork resonator design. **Right**: trap design of M018V6b Yggdrasil, showing improved electrostatic control of the quantum dot. Both boxes are 25 um in width. The B-variant has the "bubble-gum" inductor at the end of the center-pin launcher.

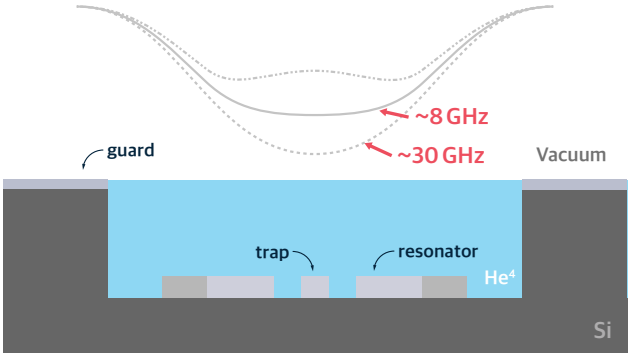

Figure 3.23: **Microwave Mode Cross-section, Yggdrasil.**

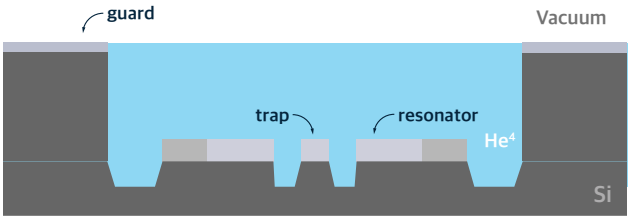

Figure 3.24: **Tri-layer Cross-section Geometry, Yggdrasil.** Showing improved isolation for the lift-off layer due to trench etched in-between the trap and resonator electrodes.

CHAPTER 4

EXPERIMENTAL SETUP

This chapter covers details of the experimental setup for the electron on helium quantum dot experiment. An overview of the cryogenics and helium setup can be seen in figure 4.1. A detailed set of schematics of the helium feeding system and the microwave setup could be found in figure 4.2 and 4.8.

The experiment is done inside an Oxford Triton-200 cryogen-free(dry) dilution refrigerator. The sample is mounted on the bottom stage of this fridge. A helium gas manifold(Heman) controlls the amount of helium fed into the sample box by letting in a number of puffs of helium gas of the same pressure and volume (at uncalibrated room temperature). Heman is controlled by an AtmelMega 8-bit micro-controller relay box, and is connected to the lab instrumentation infrastructure via the local ethernet. Details of this subsystem is covered in section 4.1.

The OFHC sample box is hermetically sealed with indium wire to prevent leakage. Inside the sample box, an electron field emitter is made with toy light-bulbs that are cracked open. Redundancy is built-in by having two of these filaments placed in parallel. A small fiberglass PCB board is mounted to the lid via two corning GPO quick connectors, allowing the filament assembly to be popped on and off without soldering. Details of this assembly could be found in section 4.2. This section also includes details on the PCB assembly, the cover-plate, and the lower-half of the box (the pedestal).

During the design and fabrication of the third-generation EonHe sample, we executed a series of fast cool-downs to test and verify our design. This set of experiment and measurements was crucial, and was enabled by a small experimental fridge in our lab called Breton. This is covered in section 4.3.

The Microwave measurement setup is detained in section 4.4. This involve both the wiring of the microwave cables inside the fridge, as well as the various microwave components such

as regulators and directional couplers. This setup went though cycles of update during the span of this experiment, and the most recent version includes a parametric amplifier.

As a quantum dot sample, quite a few DC control channels are required to shape the microscopic electro-static environment for the electron quantum dot. Details of the DC wiring and considerations can be found in section **??**.

The experimental setup extends beyond physicality. The data collection and monitoring are described in section **??**. Effort were spent on writing and maintaining a collection of python drivers for various instruments, and for making dxf design files for the samples.

4.1 Helium Feeding Subsystem

At the begining of each experiment after cool-down, we need to load helium into the sample box. Helium enters the feed tubes in gas form at room temperature. The cooling power of the cryostat decreases stage by stage. So to avoid overloading the still stage with hot, room-temperature helium gas, one wants to termalize the helium at each stage. This is done by wrapping stainless steel capillary tubes around copper cylinders and solder them together, afixed to each stage of the fridge. To prevent plug, it is necessary to use 0.085" ID (1/8" OD) tubes above 4K. These thicker tubes act as cold-traps to capture humidity and gas with high melting point that would other-wise block the narrow capillary tube. Below 4K the capillary tube had an ID of 0.022" (1/32" OD). Inserting this thicker segment at the top was experimentally necessary. Without it, plugs was frequent. This has been shown with both me and Gerwin Koolstra on separate setups.

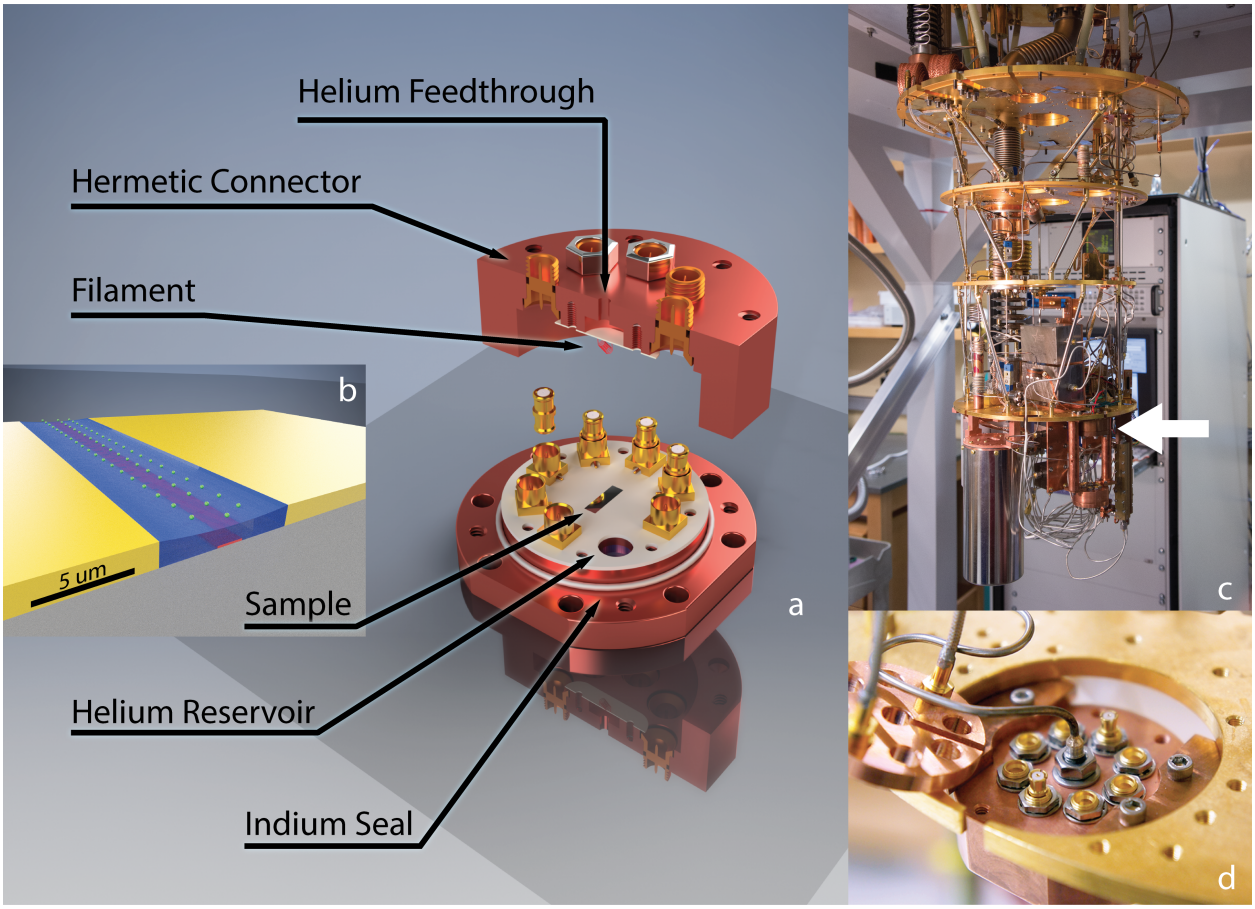

Figure 4.1: **Overview of the experimental setup** Showing the overview of the second generation setup that is used in the experiment for the PRX paper. Fig a: 3D rendering of the system, showing the cutaway view of the sample box, with the sample mounted in the Arlon breakout board. Fig b: 3D rendering of the geometry of the channels, filled with liquid helium with electrons trapped on the surface. Fig c: a photo of the setup inside the dilution refrigerator. The sample box is located next to the white arrow. Fig d: a close-up of the sample box mounted at the base-stage of the dilution fridge. The helium line is hermetically sealed to the lid of the box with indium seal from the inside, behind the filament PCB assembly.

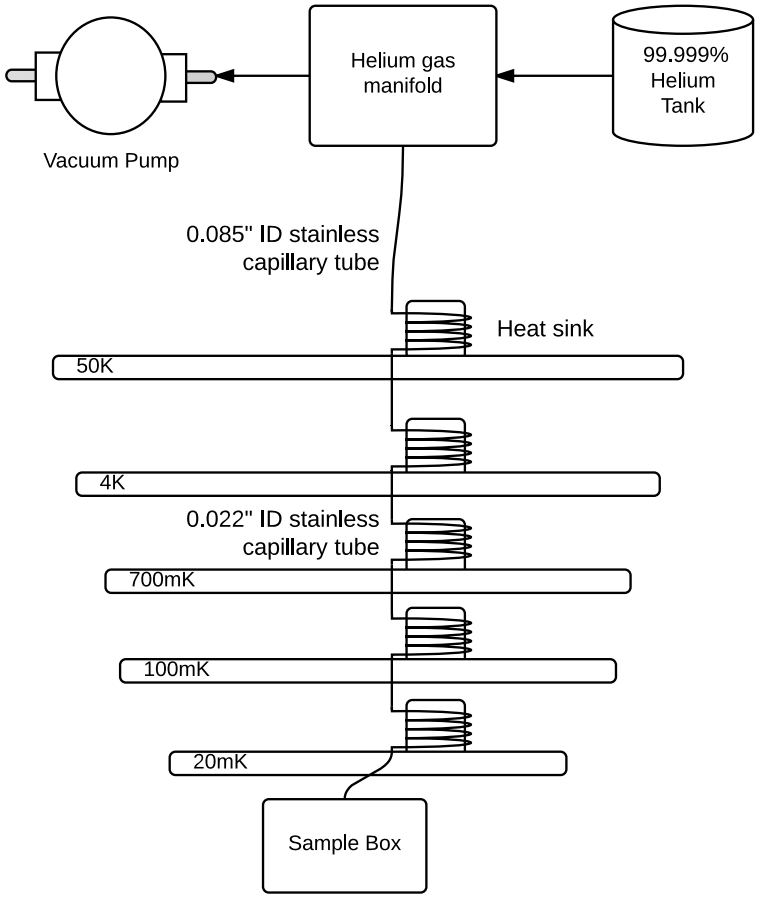

Figure 4.2: **Schematics of the Gas Handling System.** The helium gas manifold (heman) has three ports: 1. vacuum, 2. helium, 3. cryostat. The manifold regulates the amount of helium gas put into the helium feeding subsystem. Each horizontal bar represents a stage in the cryostat. Copper pole is affixed to each stage, with the helium feeding line soldered around to termalize the helium gas. This way, warmer stages take a larger heat load from the warm room-temperature helium.

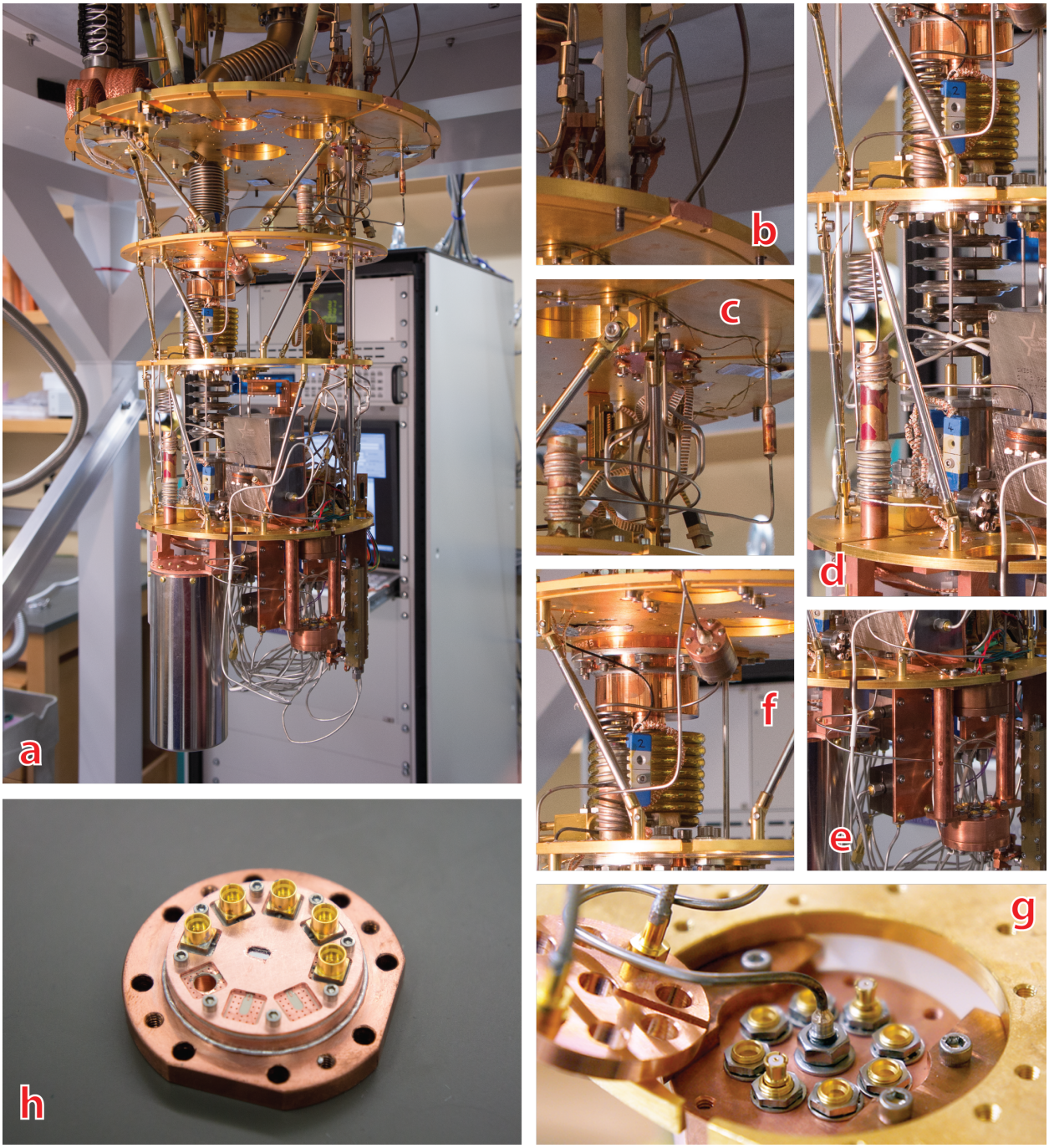

Figure 4.3: **Helium Setup, Overview**

4.1.1 Cutting capillary tubes

Before soldering, the capillary tubes are scribed with razor blades. Despite of unhelpful language used in the Rosenbaum Lab, one does not "cut" the capillary tubes with razor blades. Instead, the razor blades are used to scribe the surface of the tube. Once deep enough, the tube is bent back and forth to induce metal fatigue, which eventually yields a clean cut. A brand new razor blade is usually good for one or two of these cuts when different parts of the cutting-edge is used.

To cut the larger OD (1/8") tubes, dremel tools are used. After cutting, the cut-end is deburred with a drill. We try to make sure that the tubes don't have any metal shrapnel inside, but experiments have show that there is substantial amount of debris inside the helium tubes, either introduced during soldering and cooling, or during the manufacture process for the tubes.

The 1/8" OD tubes are joined together with the 1/32" tubes via a particularly beautiful piece of copper sleeve (shown in figure 4.3c).

4.1.2 Hard Soldering with Silver-based Solder

Because of the low working temperature and the ability for super-fluid helium to leak through molecular sized cracks, all plumbing inside the cryostat are done with hard soldering using silver-based solder. The silver solder melts at around 1000 degrees. Because the work pieces are large pieces of copper cylinder, the high thermal conductivity means the entire piece need to be heated to red-hot.

Before the soldering begins, first preform the coil shape on a fixture, leaving enough length in the loose end for connections. Strings are used to measure the proper length. The coiling fixture is constructed by hastly screwing a copper column scrap on a piece of scrap wood left by construction workers. Despite the make-shift nature of the construction, this setup was extremely effective. The scrap copper column has a smaller outer diameter,

allowing the pre-formed helical coil forms a tight fit to the copper heat sink. Then a few pre-solder simulated assemblies are conducted to make sure that all parts fit together.

standard hard-soldering procedures involve first covering work pieces with hard-solder flux. Use a few blowtorch to heat the copper till red-hot, then quickly apply a scientifically profusely amount of silver solder to the gap between the tube and the copper pole. Care need to be taken to avoid sealing the mounting screw hole on the bottom. It is a good idea to avoid getting any solder onto the mounting surface, and any excess solder is sanded off. During heating, sometimes the copper surface in contact with the firebrick end up lower in temperature. Rotate the piece to heat evenly. [1]

Since the soldering heats up the work pieces to above a thousand degrees, substantial oxidation is produced. Some of these oxydation is removed by dipping the workpieces into copper and stainless steel flux. As described before, this might also be the step where the particulates are instroduced inside the helium feeding tubes.

4.1.3 Hermetic Connectors

Segments of the capilary tubes are joined together via stainless steel connectors that are sealed with indium[2]. During our cooldowns, no leak ever occured with this setup. Both copper and stainless steel connector pieces are used and sometimes used together. Due to the small dimensions, copper male connectors tend to deform. For this reason most but not all male pieces are made of stainless steel.

During later experiments, segments of cylinders with narrow inner diameter are added to these connectors, to create impedance mismatch, with the hope that it could damp the accoustic resonance in the helium thin-film on the inner wall of the capillary tube. Because

[1] The blowtorch is also a good device for reheating left-over pizzar. When used as such, it is advised to attach a large defuser so that the cheese doesn't quickly catch fire, resulting in an unpalatable taste and a carcinogenic composition.

[2] *On usage of quick connectors:* I personally did not have good experience with quick connectors. All of the first three cooldowns ended up having leaks.

second sound is the primary way for superfluid helium to transduce heat, it was thought that this is a good way to prevent heating and improve the Q of the sample. The effect of this extra segment is not obvious.

4.1.4 On Particulate Pollutants inside the Helium Feeding Subsystem

For over a year, the sample Q would degrade after each cooldown, going from 16k to just a few hundred after three cooldowns. Visual inspection shows that the area of the sample right below the opening of the helium capillary tube inside the sample box is covered with fine particulates that can not be removed with blows of compressed air. We never managed to clean the capillary tube, so to prevent this from happening, we added a piece of fabreglass shim that is 40 mil thick on the backside of the filament PCB assembly. This shim blocks the openning of the helium capillary tube inside the sample box. We probably should have cleaned this assembly of particulates after each cool-down, but we never did because there was no noticeable Q-factor degredate afterward. This shim eliminated the Q-degredation problem.

4.2 Sample Box

In this section we go into details of the construction and design of the hermetic sample box, and subsystems inside.

The quantum dot sample is encapsulated inside a OFHC copper box that is sealed hermetically to prevent any superfluid helium from leaking out. As shown in figure 4.1, this sample box comes in two parts: the lid, and a pedestal on which the sample/PCB assembly is mounted. On the under-side of the lid, the filament assembly is mounted. This filament assembly acts as a field emission source to spray electrons onto the sample. The details of this is covered in section 4.2.1.

The microwave and DC signals feed through 16 corning PPO feedthrougs that are

mounted on the lid. These connectors are sealed with indium wire to prevent any superfluid leak. The socket is machined according to the spec of the PPO connectors, which could be found on corning's website.

4.2.1 filament assembly

The filement assembly is mounted inside a recess in the center of the lid. Two PPO connectors anchors the assembly in-place, while also providing two floating DC connections to the filaments. These two filaments are connected in parallel, so that in the case when one of them burns out during an experiment, there is still a backup one in-place.

Details of the filament PCB assembly can be seen in figure 4.4. These field emitters are made by carefully cracking open toy train light-bubs, leaving the tungsten filaments intact. The glass bottom that is left from the broken light bulb, together with the electrodes and the filament is then carefully soldered to the PCB board. Tar insulation is removed carefully with a pair of tweezers.

Note that the two leads connecting to the two light bulbs are floating. This allows us to apply a bias voltage to the field emitters, to encourage electrons towards the sample. The typical bias voltage we use is around $400mV$. In comparison, the peak-to-peak amplitude of the sinusoidal signal we apply across the filaments is around $1.5V$.

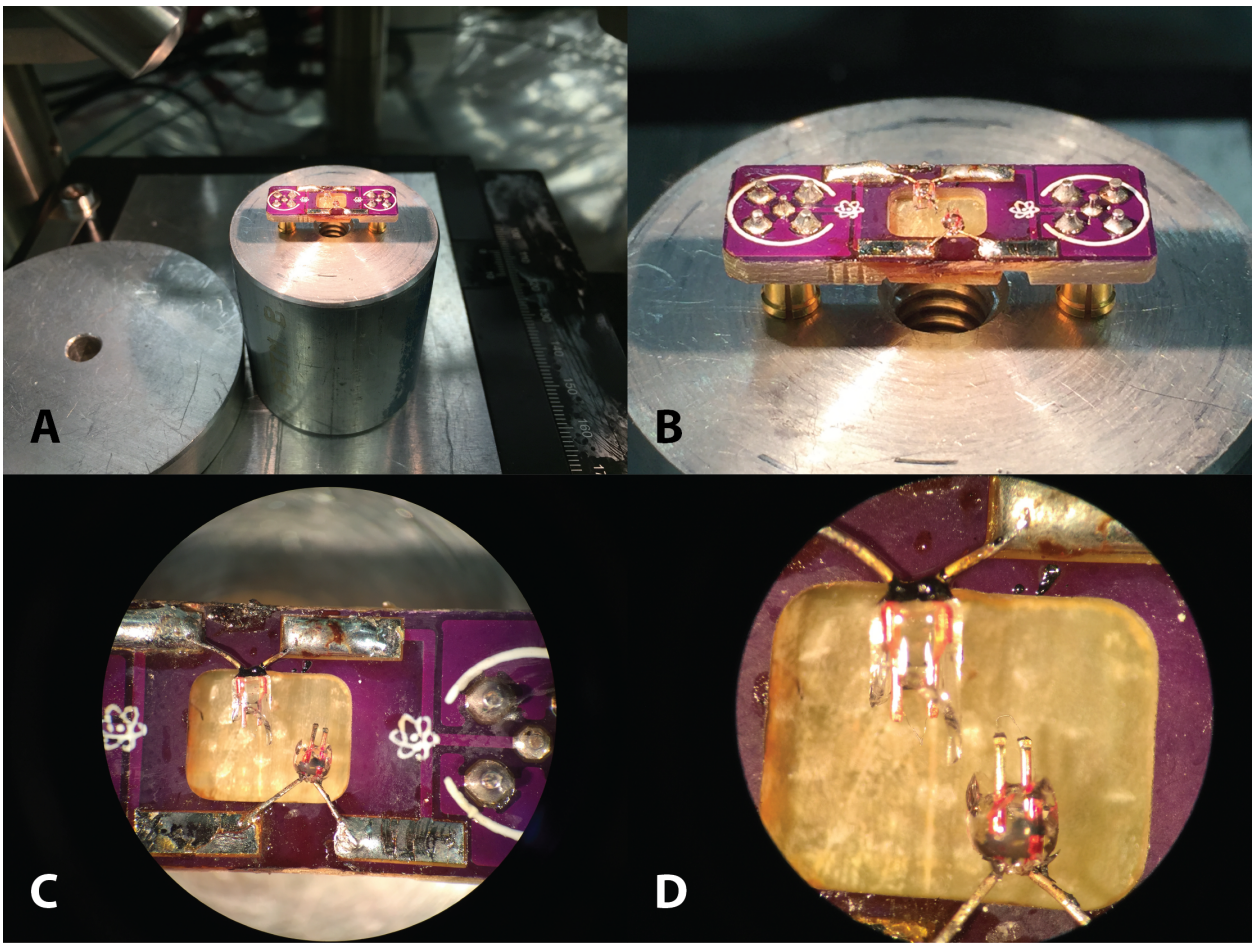

Figure 4.4: **Details of The Electron Field-emitter**. Showing the toy light bulb filament.

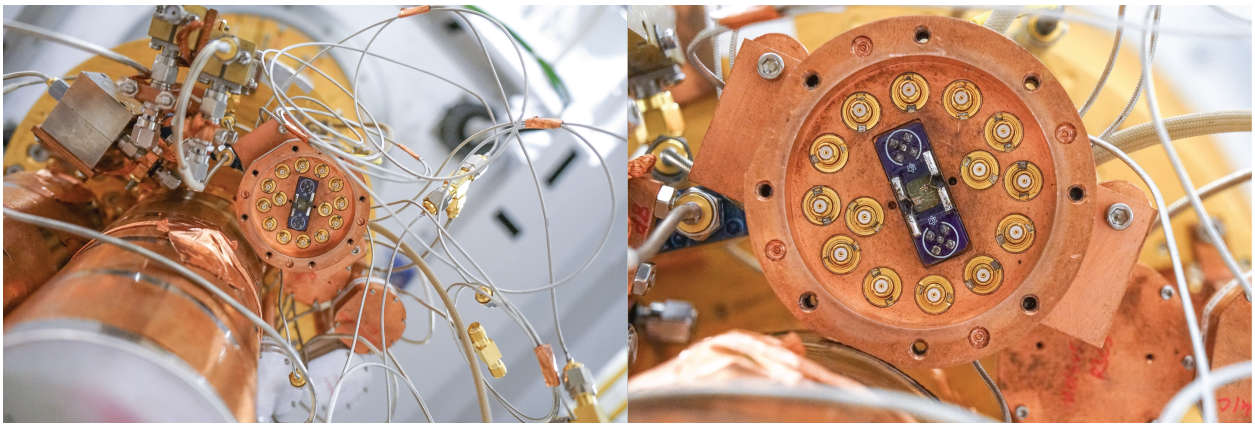

Figure 4.5: **Sample Box Lid**, underside

We refer to the bottom-half of the sample box as the "pedestal". This piece contains a small reservoire. As mentioned in the helium chapter, this reservoir is used as a potential energy ballast to control the helium surface energy, which in-turn determines the superfliud helium filling level inside the channels.

4.2.2 Mounting the Sample

The sample is mounted inside a small recess at the very center of the printed circuit board (PCB). The most consistent way to mount the sample onto the PCB, is to use a tooth pick to pick up minimal amount of silver paint, and mark the center of the recess with it. This gives just the right amount of paint. Too much paint lead to overflow to the copper surface bordering the recess, interfering with both the electric signal and contaiminating the surface for Wire-bonding. In the past, GE varnish was used to serve the same purpose. With GE varnish, care need to be taken because the varnish tend to form long strands of thread when pulled from a bottom. These thin strands tend to land on the PCB, also contaminating it, making it impossible to wirebond.

Typically, excess silver paint or GE varnish contaimination ruins the sample. It is usually a bad idea to do this on a Friday night after happy hour.

From time to time, I mount the sample without using glue or paste. This is done by surgically removing just the right anout of excess Arlon from the recess, to create a tight fit for the sample inside. I ended up prefering the silver paste despite of the messiness involved, because in this "paste-less" procedure, the sample tend to stand-up during Wire-bonding.

To prevent this, the sample is glued to the PCB, and then the entire assembly is placed on a hot plate to harden the glue. Now with the sample mounted, one can wirebond it. For Wire-bonding procedure, please refer to user's manuals for your choice wirebonder. We used a westbond with 0.01 mil aluminum wire with 1% silicon. This is a standard choice of wires for this type of task. According to wikipedia, "alloyed aluminum wires are generally

preferred to pure aluminum wire except in high-current devices because of greater drawing ease to fine sizes and higher pull-test strengths in finished devices".

4.2.3 PCB assembly

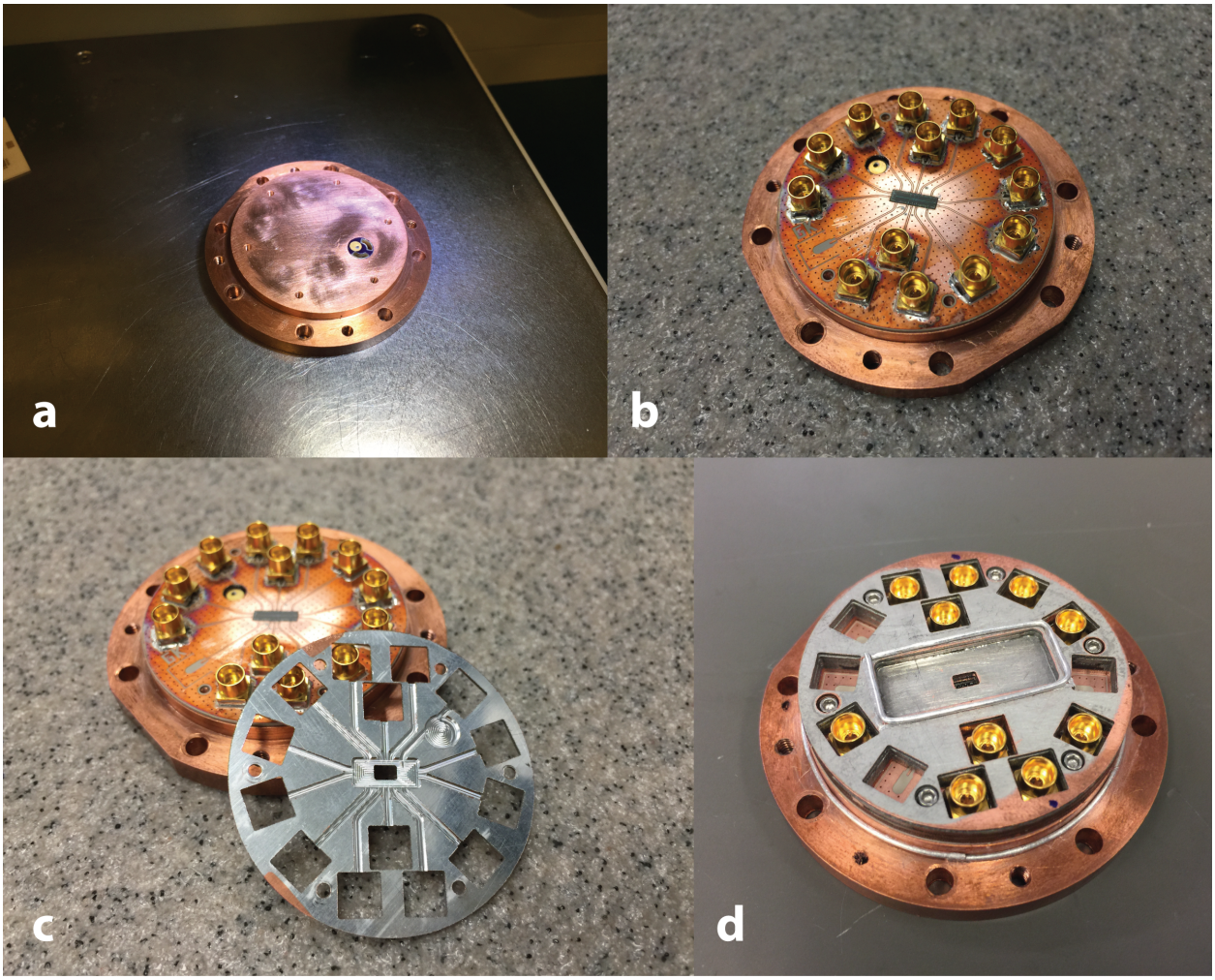

Figure 4.6: Details of The PCB Assembly

Before mounting the sample, we first need to solder the surface-mount PPO male connectors to the PCB board. This is done as the following:

1. clean the PCB by dipping it into copper flux and sonicate. Repeat three times with fresh flux each time.

2. now apply solder paste (lead-based taste the best with lower melting point) from a syringe (that the solder paste hopefully came with in the first place) carefully. Use the surface tension and the consistency of the paste to guide it, and make a U shaped pattern on the footprint of each of the sockets. Not all connectors are populated in each experiment, so only the ones needed needs to be soldered.

3. Now carefully place connectors onto these footprints, one by one with a tweezer. Do NOT press down on the solder paste. Let the surface tension of the molten solder do the work instead.

4. preheat hot-plate to 400. This is well-above the melting point of solder ($\sim$ 245). Experience show that this is a good temperature to use with an open-air lab hot-plate. First because an open hot-plate tend to have a slightly lower surface temperature than its reading. Secondly, it reduces the time it takes to reach reflow down to ten seconds. Short reflow time prevents thick oxide from forming on the surface of the copper and deformation of the arlon substrate.

4.2.4 Sample Cover and Microwave Environment

Now with the sample mounted on the populated PCB, we assemble the lower assembly of the sample. As shown in figure 4.6c and d, a metalic "cover" is put on top of the PCB to create a shielded microwave environment. Through out the span of this experiment, a few different cover plate designs took place. 4.6c shows a thin cover plate design, where a 1/64" copper plate is water-jet cut and then had it's underside machined, to accommodate waveguides and wirebonds on the PCB. Later in the quest to improve sample resonator Q, and to eliminate parasitic modes in the sample box, the excess space above the think cover plate is also filled with additional plates, leaving only a small coffin area for the filament assembly.

Note that in the center of the cover plate(s), a small rectangular hole is made to allow the electrons to reach the sample. The relative position of the hole is not very sensitive.

The coffin area is made in-contact with the lid via a piece of indium wire. The compression of this wire is much less compared with those used in hermetic sealing, but is noticeable when inspected after each cool-down. The PCB-facing side of the cover plate is plated with aluminum via e-beam evaporation deposition. The rest of the surfaces are covered with solder.

The cover plates are held together by infused solder. This is done by first pre-heating the cover plate sandwidtch on a hot plate, and then reflow solder in between.

A few counter-sunk screws holds the cover plate assembly in-place.

4.3 Fast Cool-down Setup

During the design phase of the third-generation sample Yggdrasil, as the sample design becomes more sophisticated, some of the additional DC control lines caused the resonator Q to go down. Unsure whether this is a design issue, fabrication issue, MW environment issue or something else, it became obvious that we need to iteratively validate/reject these ideas quickly.

So we ended up running fast cooldowns inside Breton. Figure **??** shows the line-up of samples packaged inside octo-boxes ready to be installed inside Breton. The smaller octo-boxes only have the microwave wiring's connected. Samples inside has variations include different fab variations, with or without wire-bonds, and so on.

This series of quick validation experiments allowed us to improve the resonator Q quickly. It turned out that added DC electrodes introduced parasitic models along the edge of long flaps of ground plane, and is solvable by adding wire-bonds across the resonator.

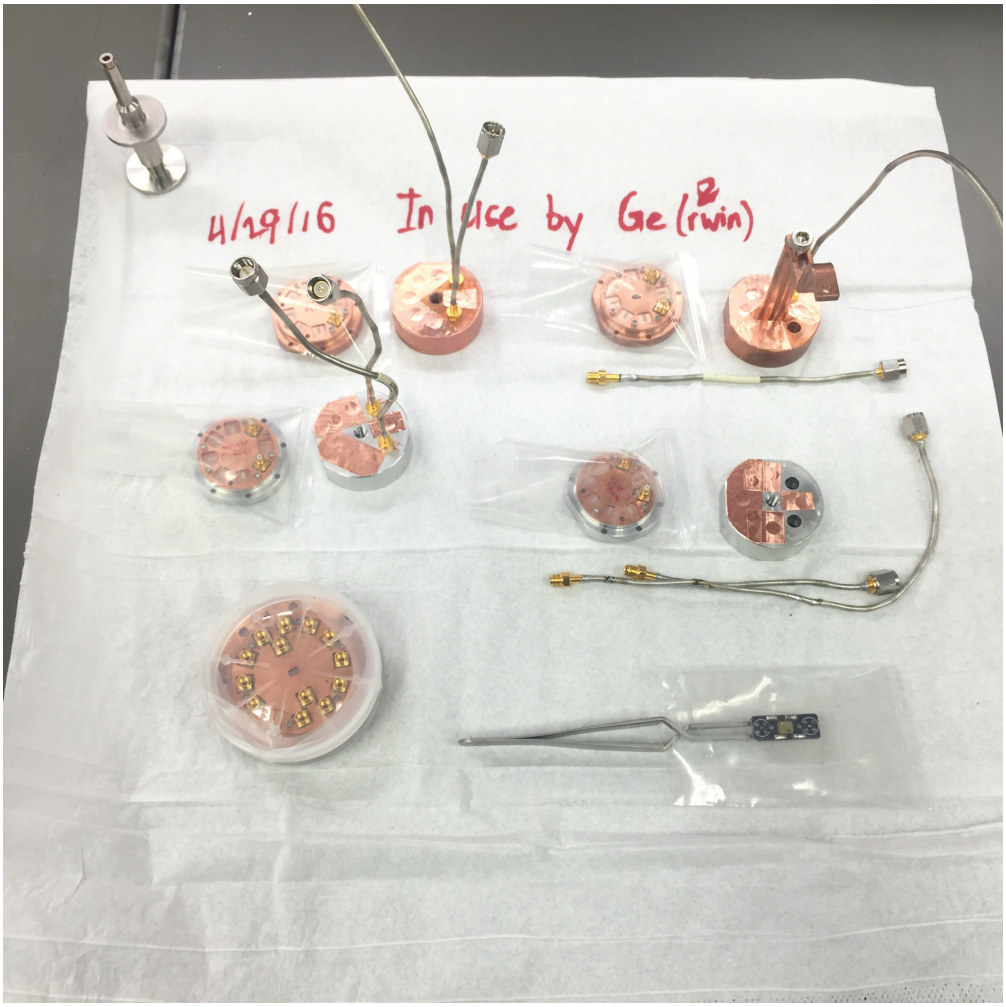

Figure 4.7: **Sample Box Assemblies, Ready to Be Mounted.** Smaller octo-boxes contains the fast-cool-down samples. Bigger 16-connector sample box goes into the Oxford. The filament PCB assembly is show on the bottom right, clamped between a pair of tweezers, inside a plastic bag to keep it clean.

4.4 Microwave Setups

The measurements are done dispersively by measuring the shift in the cavity resonance frequency. An Angilent network analyzer is connected to the input and output ports of the cavity with attenuation along the input line for photon thermalization and amplification on the output. Low-pass filters filled with the Eccosorb epoxy are used to filter out thermal photons that would otherwise enter the sample box and affect the cavity Q.

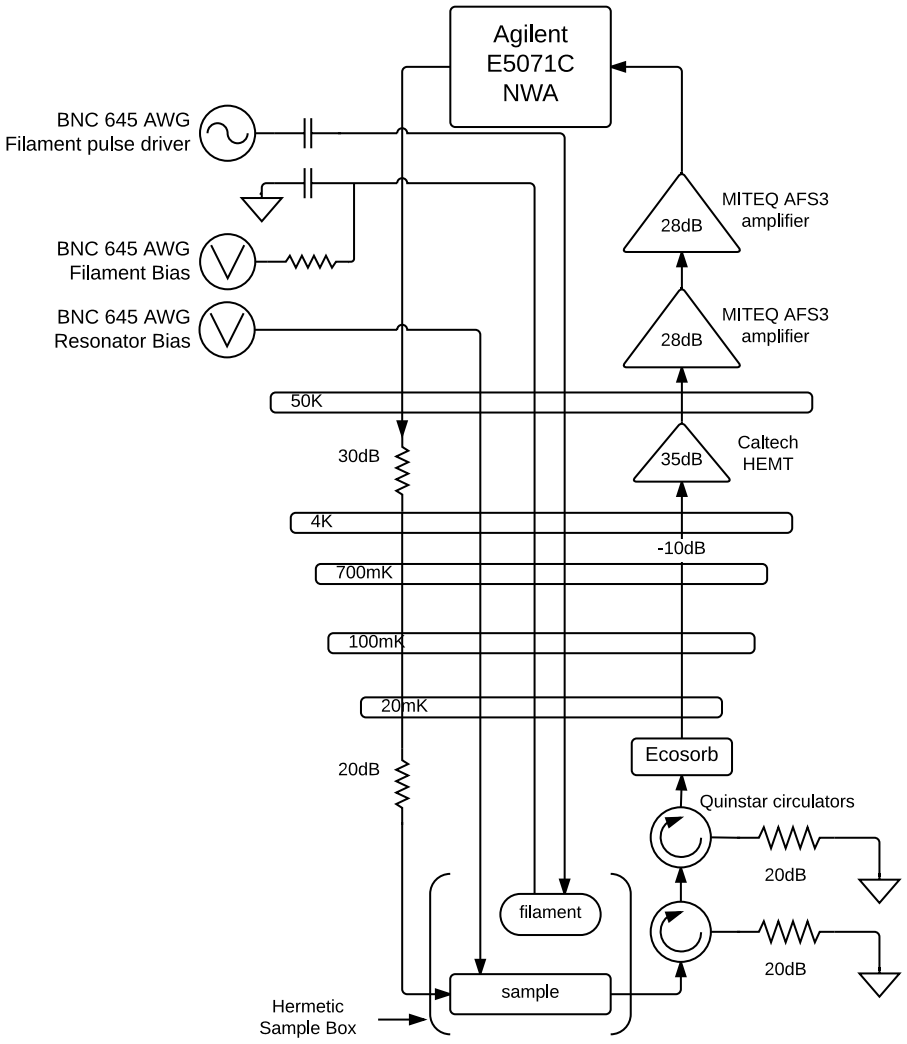

Figure 4.8: **Schematics of The Microwave Measurement Setup**

CHAPTER 5

DEVICE FABRICATION

A completed project usually involves the following steps:

1. Design and Simulation of the sample
2. Development of Fabrication Processes
3. Measure, experiment and verification of sample properties
4. Theoretical explanation for the experimental result
5. writing up our findings

In this chapter, we will document the work that went into step 2, and the tightly coupled step 1. Iterating through the entire loop makes it easy to maintain momentum. With this in mind, we list some lessons learned during this project, both on fabrication and beyond.

5.1 Prelude: Chitty Chitty Bang Bang[2]

Over the course of this project, four major process development efforts were undertaken on the Electrons on Helium project. From the year 2011 to 2012, I worked locally at the University of Chicago to develop superconducting junction based qubit sample. At the beginning, we used an old Hitachi SEM for the patterning. Being the first student and have never seen a good e-beam patening result, it took us 8 month and a few calls to Joe Nabity to find out that the distortion the Hitachi produces is due to the slow ramp time of its optics. We then decided to persuade the fascility manager to add patterning capability to the FEI SEM system. To our surprise the FEI system already had NPGS and the DAC card installed. The reason why it wasn't being used for pattern was mainly due to existing

[2]special thanks to Srivatsan Chakram

user's fear of having the aperture contaiminated due to the high writing current patterning requires. Another reason is that before our group's arrival, there hasn't been a need for good e-beam patterning. As the vanguard, I started to working with the FEI.

Dave and I waged a bet to see whether I could get the FEI NPGS system to work in a week. To our surprise, the system was so out of shape that surface-mount integrated circuits fell off the main DAC card due to stress (and probably bad reflow). In addition, the optically isolated beam shutter controller was also broken. I negotiated cheap quotes from the companies responsible and sent out both of these two devices to be fixed. A close inspection of the FEI optics also showed that the main column is out of alignment. The management philosophy of the facility at that time was to limit the access users have. Under the encouragement of the manager, I obtained the maintenance password for the FEI from the service engineer. According to the calibration protocol in the manual, I calibrated the main column. During this period, I learned a great deal from Joe Nabity over the phone. He was always patient and knows all of the failure modes of the system.

This setup was done over the period of two weeks. Motivated by the challenge, I stepped on the toes of the facility manager and eventually got banned from the facility while I was vacationing in China. The FEI NPGS system that I set up ended up producing many samples for the solid-state qubit experiments in our lab. To avoid more drama, I began working at the Argonne National Lab's Center for Nano Materials (CNM). I had a wonderful time there and learned a great deal from the scientists in the clean room[3].

The process during this phase was mostly Aluminum-on-sapphire lift-off process with double-angle evaporation.

[3]Thanks to Leo Ocola, David Czaplewski, Ralu Divan, Valentina Kotepova, Sussanne, and many others.

5.2 Argonne CNM, JEOL, Trident and Fjolnir

The first process developed at Argonne went into mask M4, M005 and M006. This is a thick-niobium-on-sapphire process. The Niobium layer is about 800 nm thick. To make the micro-channels, we etch through the deep niobium. The thick niobium then forms the side-wall of the channel.

A second-layer thin niobium pattern is then deposited and lifted-off. This layer defines the submersive center pin of the resonator. This is the sample that is used in the PRX paper.

A great deal of effort were spent on the two few-electron traps on each arm of the resonator. The small gap between the center island and the ground plane, coupled with the large change in height, caused an awkward resist profile for the second layer. Most of the samples are shorted. In the end we found two samples that did not have a short, and used those for the experiment. Despite of these extra effort, the traps were never used.

With the benefit of hindsight, we would've just made a very simple resonator sample without the extra electron traps. In the end the main contribution from this work was the development of the numerical simulation model that accurately predicted the dispersive shift due to electron coupling. How to define clear objectives for a publication, and iterate efficiently toward this goal, is something that I learned much later when I started working on machine learning research full time.

The former resulted in the sample that was used for the PRX paper (M006). The latter resulted in a sample called Trident which implemented the first tuning-fork resonator design. Data from Trident was very suggestive of trapping of a small number of electrons. During the same period of time, most of the numerical effort for the PRX paper were specifically targeting electron-resonator interaction. After a few month working with Trident, including a short visit from David Rees, we decided to iterate with a newer design called Fjolnir. The rationale at that time was the data from Trident "was not good enough", without much further explanation. Personally I was hoping that by designing a new sample I would be

able to achieve single electron on helium strong coupling, and resolve an avoided crossing. But this never happened. Even as Gerwin tolled away with the Yggdrasil sample (a single sample we make togehter) for another year (from late 2017 to mid 2918!!). With the benefit of hindsight, I should have spent time on numerical simulations of a small Wigner crystall inside the trap and try to understand the features numerically–just like how my numerical simulation was the key to the PRX publication. But instead, we decided to iterate quickly on a new sample design.

In late 2015 (November), Gerwin and I started working together on designing a new, improved Trident with more DC control lines in the trap. This sample called Fjolnir was the last sample I made at Argonne. It resulted in two samples (out of 40 wafers) from the M016v5 design before I left for a summer internship at Uber on June 9th.

Gerwin spend the summer working with the Fjolnir sample but it became quite obvious that loading would be difficult. Our design (Fjolnir) made the trapping area narrower than the rest of the resonator out of considerations of the microwave constrains that we wanted to hit. However this made it impossible to load electrons into the trap, because the ground plane that forms most of the electrostatic landscape forms a barrier. As a result Fjolnir never produced comparable data (of few electrons) to those obtained with Trident. The insight of this grave design mistake came one day when I was chatting with Gerwin while staring at the poster of Trident on the wall. That the trap should instead be wider, so that it could have lower potential energy than the resonator was a shocking realization–we have made a mistake, and need to re-iterate.

Because I was responsible for the fabrication work at Argonne, and I had to leave for the Uber internship, the team decided to start iterating again only after I came back from Uber. Right around this time the new Prizker NanoFab (PNF) fascillity entered full-operation. So starting from November of 2016 Gerwin and I began our fab process development solely at the PNF facility. We built one of our first samples before March Meeting. For the next

month or so, we significantly improved the Q-factor of the on-chip resonator. By May, we had a working sample with high-Q, reliably showing preliminary signs of trapping a small number of electrons in the trap.

5.2.1 Black Forrest and Micro Masking

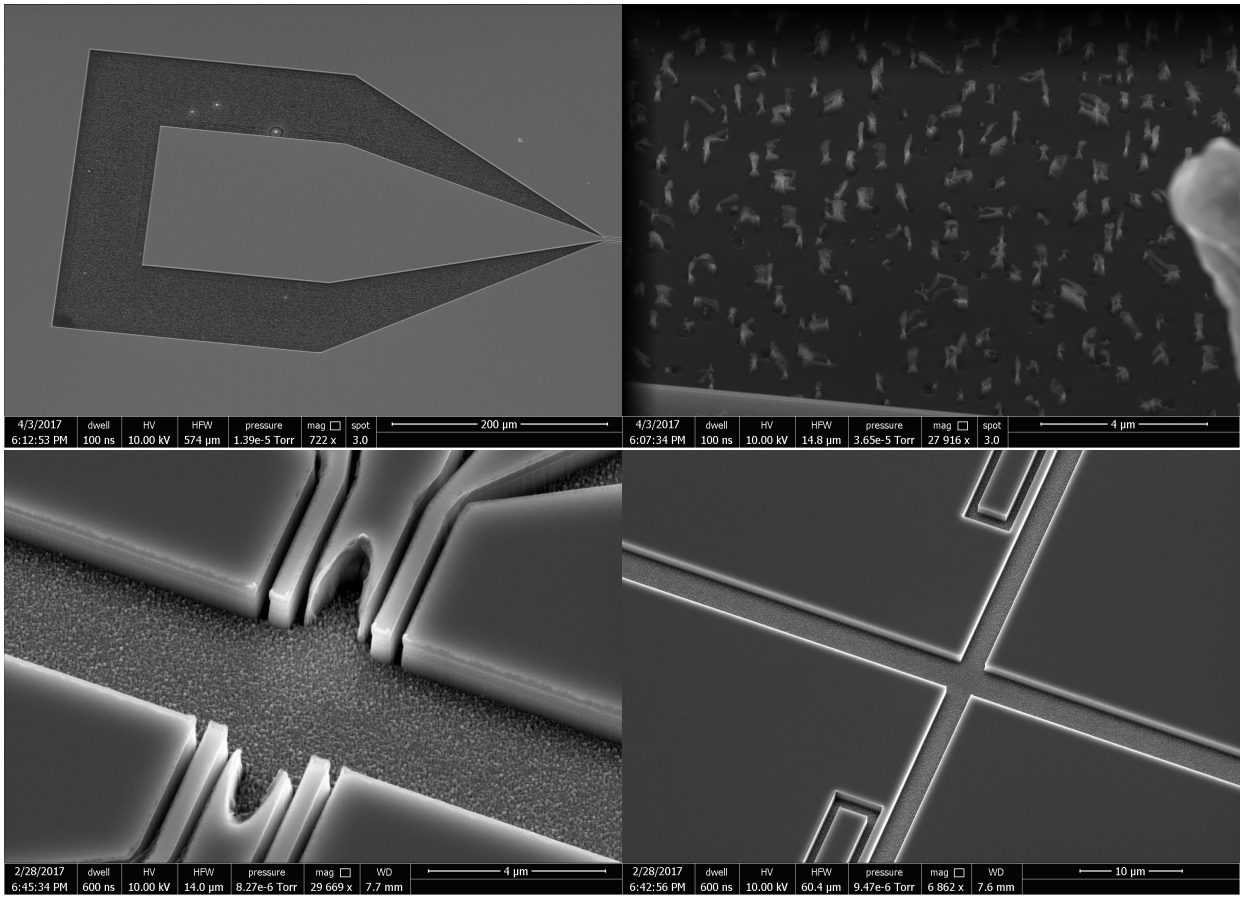

Figure 5.1: Showing details of the micro-masked sample. Upper-left: zoomed-out image of a typical CPW launcher. Micro-pillars are visible in the exposed area between the center pin and ground. Upper-right: shows details of the pillars. These are particularly malformed. Others look like poles taht are quite nice. Usually quick look by the naked eye is enough to determine whether micro-masking has happened. Bottom-left: more severe case of micro-masking, in the trap area. Bottom-right: The same sample around the couplers.

A recurring theme in the process of deep reactive ion etching (RIE) is the formation of

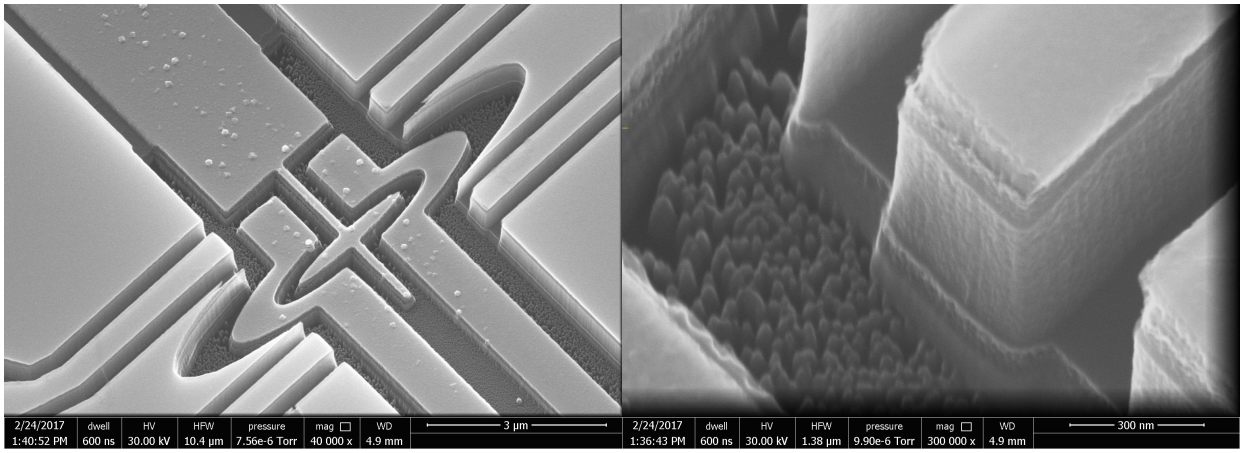

Figure 5.2: Micro-masking can also happen in the third-layer. Left: micro-pillars in the third-layer in the trap. Right: Zoomed in version, showing details of the high aspect-ratio of the pillars.

micro-pillars[4] due to micro-masking. Micro-masking happens when a hard-mask material is used during the RIE process, and due to the bombardment of the reactive gas, in particular heavier elements such as Br^{-1}, some of these hard-mask material gets sputtered off the surface of the wafer and lands back into the exposed areas of the pattern.

Appearance

Micro-masking usually appears as pitch-black areas where the substrate is exposed, regardless of the original color of the substrate material. This is because the fine, nano-meter scale pillars absorb visible light by increasing the number of reflection between the pillars, similar to the conically shaped tiles in an anechoic chamber. The produced surface texture can turn both silicon (naturally gray), and fused sapphire (naturally transparent) into a pitch-dark color.

Figure 5.1 shows the sample under the SEM. Density and shape of these pillars vary. increasing density and reduced pillar girth corresponds to darker color.

[4]during the frustrating process of trying to eliminate this particularly difficult process issue, Gerwin and I half-joking called the pillars "micro-penises" because of their phallic shape. Over time, they were also called "Charittos" when they seeming grown out of the interface on the edge of resist coverage, curled up like Charittos

Conditions, Theory and Solution

So when and why does micro-masking happen?

Micro-masking happens when you use a hard-mask material and there is sputtering during RIE. In other words, it happens when there is insoluable population inside the RIE chamber during etching. These insoluable radicals redeposite on the exposed areas of the pattern, and cause pillar like masked structure.

Micro-masking tend to happen when either 1. a large surface area is covered by such material, or 2. the etchant involve heavy radicals like Br^- that tends to sputter more. In our process, we used Aluminum as a hard-mask against Nb substrate in Trident. With Yggdrassil, we used SiO_2 as a hard mask against Si etchant with Bromide. In both these two cases, we fabbed with 2 inch wafers inside 4 inch RIE process machines. The carrier wafers were randomly picked between silicon and silicon-oxide.

In the Trident process, I eliminated the sputtering and re-demopsition of the Al hard-mask by cooling the sample down to - 20 . The theory was that by cooling the sample down, the sputtering could be reduced and micro-masking will happen less.

During the Yggdrasil process, we solved the micro-masking problem definitively by re-placed the SiO_2 carreir wafer with a silicon one. We theorized that this could greatly reduced the SiO_2 population inside the chamber during the etching by limiting the surface area of exposed SiO_2. And the difference was quite obvious within the first experiment.

The 2 inch sample wafer is covered by resist during RIE. Therefore using a 4 inch SiO_2 wafer as the carrier increases the sputtering infinitly. By replacing the SiO_2 wafer with a sillicon one, there is virtually no SiO_2 exposed to the etching chemistry. As a result, no redeposition was seen after this change.

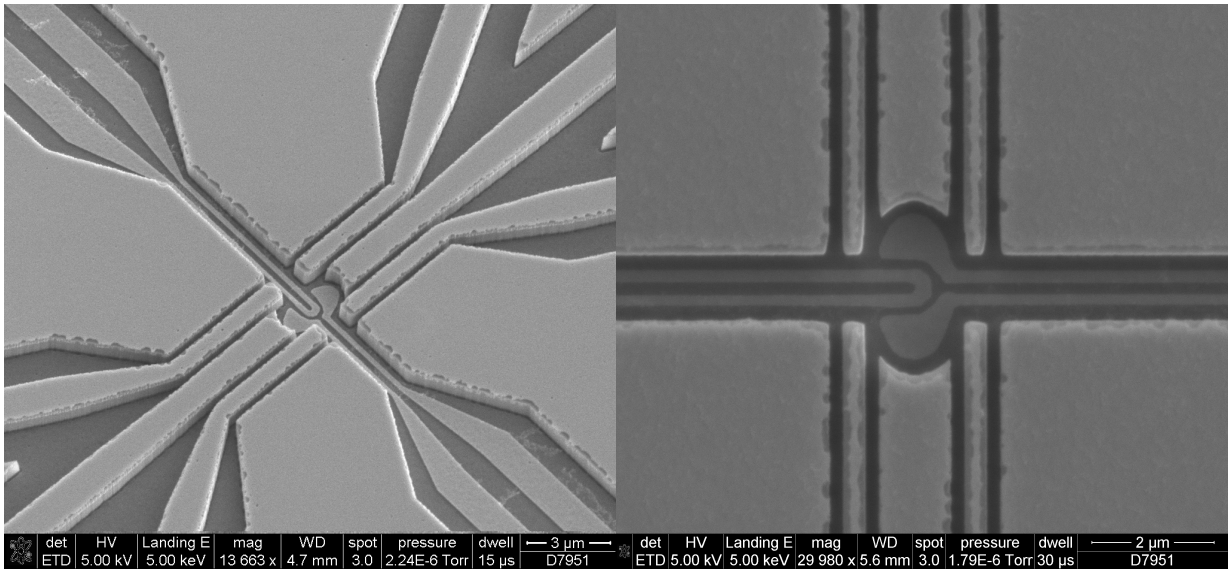

Figure 5.3: chipping that has occurred in previous samples, showing similar pattern. Sample images *after stripping off the* SiO_2 *hardmask after L2 lift-off.*

5.2.2 Side-etch and RIE Under-cuts

We were surprised to see chipping of the niobium on otherwise well-defined silicon support (Fig.5.3). While the chipping is minor, it became an issue when it affected the narrow trap electrodes that is only 125 nm wide. At first we suspected that the layer of SiO_2 thta is being used as a hard mask had built-in stress and cracked. A close inspection of the sample after the penetration and before the actual silicon etch showed that this is not the case (Fig.5.4), that the resist and mask are most likely intact.

This observation lead us to play with all of the etching parameters. Considering that the penetration step is a less anisotropic, we tried to reduce the span of this step to keep the side-etching underneath the SiO_2 mask into the niobium metal layer to a minimum.

5.2.3 Resist Profile in Micro-channels with Tri-layer process

During our first experiment on Yggdrasil, the sample shorted between the trap and the center pin at 12 volts (pin-to-pin). The resistance between these two electrodes went down to a

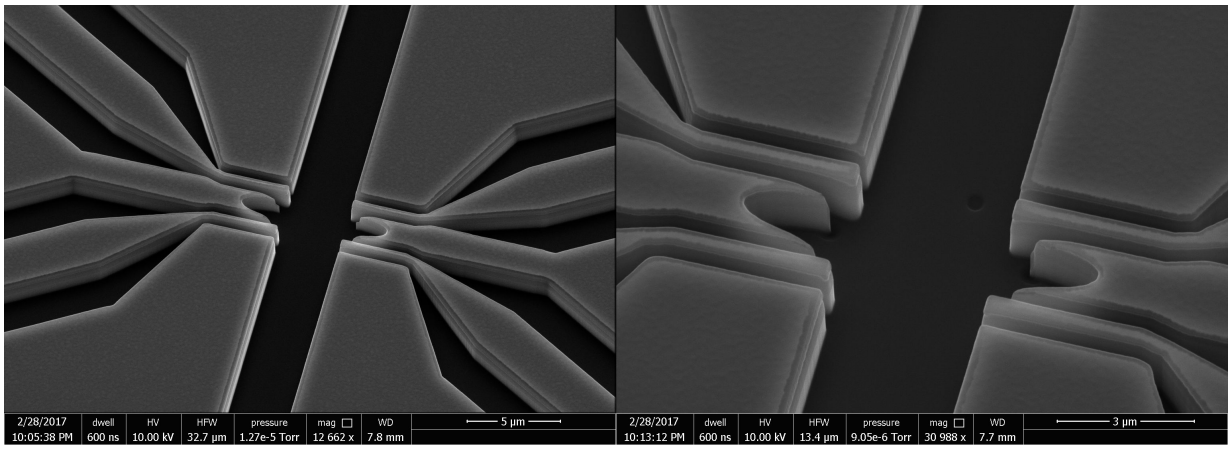

Figure 5.4: Upper left and right: undercut visible underneath intact SiO_2 hardmask.

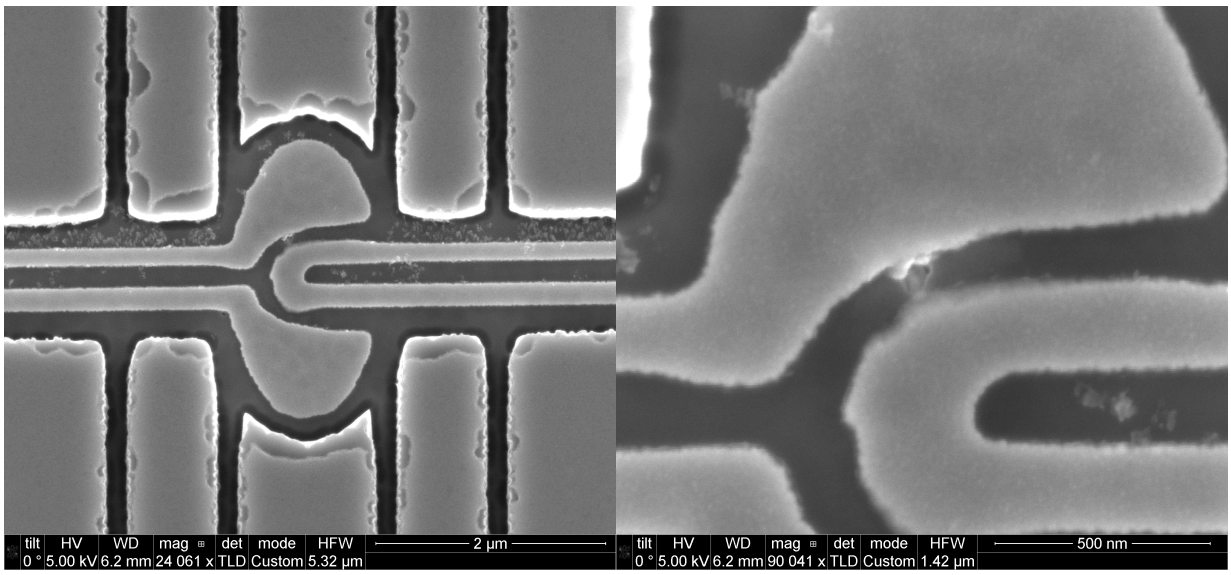

Figure 5.5: Left: zoomed-out SEM image of the trap, showing the tight tolerances between the trap electrode and the center pin electrode. A small short mark is visible between these two, showing the silicon substrate being damaged by the arc. Right: Zoomed SEM of the left figure, showing details of the arc mark in the substrate. This mark is visible after the sample has shorted. A sudden change in resistance was witnessed.

few ohm suddenly and remained so. Warm-ups did not remove the short. Close inspection of the sample shows that there is significant damage to the substrate between the two trap electrodes Fig.5.5

This shorting never occurred with other pairs of electrodes. Given the center pin and the trap are both on the L2 lift-off layer, we theorized that the small distance (around 125nm)

created a very low breakdown votage for the silicon substrate. This is consistent with the break-down electric field of silicon.

To solve this problem and being quite confident in our fabrication skills, we decided to experiment with a third RIE step. We refer to this step as the `L3 RIE`. Out goal was to **"hit" the third layer exactly where the L2 lift-off pattern is**. We want to etch a 125 nm wide channel 400 nm deep, in-between walls of a 1 micron-deep channel.

This is difficult lithographically because the resist profile is uneven. The thickness of the resist is jointly determined during the spin-coating process, by the centripital force, the viscosity of the resist, and the 3D geometry of the sample. The resulting thickness affects the amount of e-beam dosage. Large latitudes in thickness variation in small areas could prevent clearance of the exposed area.

In addition, the height-to-width ratio of the resist after development is larger than 1 in the area that defines the center pin (5.6). This makes the plastic resist susceptible to built-in stress, and tearing by the large surface tension of the developer during development.

Over-etch of L1 Metal layer

Another complication that occured during this step is the loss of the L1 metal layer near the trap during the L3 etch. During spin-coating, the resist inside the micron-deep channel pulls the resist on top of the L1 metal layer near the edge. This causes the resist to be much thinner in those areas. During the etch process, the resist from these thin areas gets consumed first. Leaving the metal underneath unprotected from the Bromide chemistry.

To fix this issue, we chose a slighly denser resist solution (ARP 6200.13), and spun at 2000 rpm (slower). This resulted in around 800 nm thick resist inside the channels. The increased resist thickness completely eliminated the L1 metal consumption in this step.

5.2.4 Sonication Damage to Thin Silicon Ridges.

Because of some of the electrodes in the L1 etch layer is quite narrow, we observed chipping happing to the trap electrodes during sonication. The thin silicon slabs supporting trap electrodes that are pattened by L1 etch cracks and chipped off.

5.2.5 Final L3 Etch Recipe and Results

The resulted sample is shown in Fig.5.8.

The final recipe is the following:

1. adjust the beam dosage to account for the increased resist thickness
2. Use a slightly thicker version of the resist during spinning, to prevent the L1 metal from getting consumed by RIE.
3. Quickly dry wafer using blow-gun, at 6.0 . This reduces the pull from the surface tension during drying.
4. for the SiO2 mask penetration, reduce the penetration step (O2) to 5 sec. This prevents consumption of the narrow resist patterns.
5. sonicate for 10 min. Longer sonication could break the thin L2 electrode definition.

5.2.6 Miscellaneous

- Nb side etch increases when the punch-through step is longer. To reduce `side-etch`, reduce punch-through.
- Micro-pillars are mostly a result of SiO2 hard-mask `re-deposition`. This is because HBr particularly the Br^- radicals are very heavy, and it sputters even more effectively than Argonne. As a result, large coverage of hard-mask material (in this case SiO_2)

in the etching chamber will lead to large quantities of involatile species from the sputtering. To avoid this problem Use Sillicon carrier wafer, and run the HBr process for $10 \sim 15$ minutes to clean the carrier wafer before the etch.

- Aggressive Fluorine etch of the Nb and the SiO2 hard mask **does not** cause the Nb `side-etch` problem. The Punch-through does.
- Increase `punch-through` time when sporatic micro-pillars show. Balance the parameter by avoinding the 'side-etch'.
- Etch rate is **faster** on a Silicon carrier wafer without re-deposition, than on a thermal SiO2 wafer. Rate is around 3 x.

5.3 UChicago PNF, Yggdrasil

The final process development I was involved with was Yggdrasil.

- 2011 - 2012, Hitachi, FEI and NPGS
  - Hitachi NPGS system, significant distorsion for patten ¿ 20 um. Manual zoom
  - Setup NPGS writing system on an FEI from scratch
  - got banned from the fascillity, and start working at Argonne
- 2012 - 2013, Argonne CNM and PRX Sample
  - 20120624 M004 start at Argonne
  - 20120803 M005 Constricted Happiness
  - 20121100 M006 PRX paper sample
- 2013 - 2015
  - 20130730 M007v1 Trident

- 2015 - 2016, last sample at Argonne
  - 20151102 M016v2 Fjolnir spin coupler
- 2016 - 2017, UChicago PNF
  - 20161127 M017v1
  - 20161130 M018v1 Yggdrasil no trap pinch
  - 20170226 M018v5 bubble gum launcher
  - 20170403 M018v6 integrated low-pass filter launcher

Three generations of samples and fabrication processes. Continuous upgrade on fabrication process with each sample.

The coplanar waveguide resonator chip is fabricated via a two-step e-beam lithography process. The ground plane is made of 800 nm thick niobium, whereas the center pin of the waveguide is made of 80 nm aluminum. All patterning is done on a JOEL 100 keV e-beam writer.

Due to the thickness of the niobium layer (800 nm), an aluminum hard mask is required for the etching. Re-depositioning of aluminum (micro-masking) occurred during the RIE process, which is mitigated by over-etching at the end.

Below we list all the fabrication steps:

1. First Layer
   (a) Nb deposition and wafer preparation
      i. Coat 2-inch sapphire wafer with 800 nm Nb
      ii. Coat wafer with aluminum as the dry etch stopper layer
   (b) E-beam lithography
      i. Spin coat ZEP 520 at 3000 rpm for 45 sec

ii. Pattern with a JEOL JBX9300FS tool; area dose 1600 C/cm^2.

iii. Develop ZEP in xylene at 0, rinse with DI water.

iv. OPT (oxygen plasma clean) 10 min

(c) Dry etch (reactive ion etching)

i. Prepare the chamber by running the Al etch recipe for 10 min.

ii. To pattern the aluminum hard mask use BCl_3(3.0 sccm) and Cl_2(24.0 sccm) at 20°C, for 1:45 min.

iii. Prepare the chamber by running the Nb etch recipe for 10 min.

iv. Then with SF_6(25 sccm) + Ar (5 sccm) at 20°C, for 15 min until etched through.

2. Second layer:

(a) E-beam lithography

i. Spin coat ZEP 530 at 4000 rpm for 45 s.

ii. Pattern with JOEL tool at area dose of 1600 C/cm^2.

iii. Develop ZEP at 0, rinse with IPA and DI water.

iv. OPT 10 min

(b) Aluminum lift-off

i. Evaporate 80 nm of aluminum

ii. Dip wafer in n-methylpyrrolidone (NMP) heated to 60,

iii. As the resist dissolves away, gently blow away the aluminum and dip into acetone heated to 60

iv. take out and blow dry.

3. Dicing and sample mounting:

(a) sample is diced and mounted to a FR-4 break-out board via wire bonds.

5.4 Detailed Process Note

The fabrication process for the M018 Yggdrasil sample was developed with three e-beam lithography patterning steps, two RIE etch and one lift-off. The patterning and etching uses SiO_2 as a hard mask. The detailed process note follows:

5.4.1 Preparation and First Layer E-beam

This layer is an etch process using SiO_2 as a hard mask, so make sure you deposite the oxide layer first. I can't tell you how many times I have prepared wafers forgetting to add the oxide.

1. First deposite the wafer with 80 nm of niobium at about 0.9 nm/s. After, coat the wafer with SiO_2 in a HPCVD machine. Use a calibrated process to achieve 80 nm (for us it is about 4 minutes). Make sure you clean the instrument before hand, or every couple of humdred nanometers. Otherwise excessive debris will form. Run a dry deposition run after the clean to condition the chamber.

2. To coat the sample with resist, spin ARP 6200.13 at

   (a) 500 rpm at 250 rpm/s for 5 seconds to spread the resist

   (b) at 2000 rpm 2 1000 rpm/s for 60 seconds. this gives about 800 nm thick resist on the wafer.

3. block the air hole on the lid of the cleanroom spinner to reduce evaporation induced thickness variation.

4. pre-spin the spinner before the sample, to reduce the speed variation for the first sample. This is, really really important and most people don't notice this even though the color of the wafer is quite different.

5. to avoid having streaks in the resist:

   (a) siphone resist off the top 1/3 of the bottle. There are usually solids on the bottom. These debris cause streak marks to form on the spun wafer.

   (b) never, never ever blow the pipet inside the bottle. People who do this need to be fired. Alternatively they can be assigned to cleanroom work for life.

   (c) clean the pipet by siphoning a bit extra and eject a small amount before applying the resist on the wafer.

   (d) if the pipets are clean, can use the side of the plastic pipets to spread the resist.

   (e) suck away air bubbles that forms on the surface if seen.

   (f) leave a little resist inside the pipets at the end of the application, to avoid making bubbles on the surface.

6. measure the resist thickness to keep track of variations and to adjust dosage.

7. before baking, use acetone wipes to clean the backside. Make sure the acetone does not get onto the resist side of the wafer.

8. or to forgo the previous cleaning step by first making sure that the wafer holder on the spiner is complete clean by cleaning it with an acetone wipe between wafers. This way the only resist on the back side of the wafer would only come from the beading on the side of the wafer that formed due to surface tension of the resist. These beads are kind hard to clean because they are on the edge. Cleaning efforts tend to mess up the resist.

9. transfer the wafer to the hot plate. Bake for 3 minutes at 150 . Take the sample off quickly. Much longer baking time may change the sensitivity of the resist.

5.4.2 First Layer Dry-etching

The RIE (reative ion etching) process is usually the step that takes the most effort to debug. Details of the etching process is covered in previous sections. The process described here uses 4" silicon carrier wafers **without** the thermally grown SiO_2. Excessive sputtering from the oxide causes micro-masking.

1. Using the PlasmaTherm ICP Flourine Etcher, etch through the niobium and the oxide hard-mask. The etch time is around 9:30 min.

2. Now to etch into the silicon, switch to the Chlorine etcher. It takes about 6:30 minutes to etch 800 nm. Again, use a silicon wafer.

3. reduce the penetration step size if the niobium on the edge of the exposed area show chipping. This is because the penetration step in the flourine process is isotropic (non-directional), whereas the chlorine process is not.

4. There is typically a little bit of resist left. This is helpful towards preventing micro-masking, because the overall exposure of SiO_2 is limited. However it is not crucial to have resist left.

5. now to strip and clean the sample before the lift-off L2 process, one can directly dip the wafer into buffered HF without cleaning the resist off first in heated NMP. There is visible lamination as soon as the wafer is dipped in HF, showing signs of the left-over resist. Leave the wafer in HF for about 2:30 minutes. Time is not sensitive in this step, and have some fun taking pictures.

   (a) when dipping into HF, make sure the wafer cross the air/HF boundary as quickly as possible. Reaction happens at the interface that creates dry marks that is not possible to remove afterward.

(b) same applies to the drying after taking the wafer out of the buffered HF: Use running water in an acid hood to clean the wafer of any left-over HF, then use the surface tension of water (which is large) and blow dry. Never rely on evaporation of solvents. In fact, cold water doesn't evaporate quickly at all.

5.4.3 Second Layer E-beam and Lift-off

This is a lift-off step, so no hard-mask is needed.

1. First spin ARP 6200.13 at 4000 rpm and bake at 150 for 60 s. Use the standard recipie in 2 for the resist (5-10 sec to spread, 500 - 1000 acceleration etc.).

2. Mount on e-beam writer holder, align the wafer, and do chip-level alignment to get good layer-to-layer alignment. A good writing system should have sub 5 nanometer alignment accuracy.

3. Develop with n-amylacetate on a cold development stage, at 6 , for 60 to 90 seconds. The cold development stage should have a cover for good temperature consistency. Taking a few more minutes shouldn't hurt. If there were left-over resist, or failure for the deposited niobium to stay attached, increase the dose.

4. Evaporate 80 nm niobium in a plassys at normal angle.

5. To lift-off, let the wafer stay emmerged in NMP for could of hours. Be patient, don't mess with it. Ideally the resist side of the wafer should face opposite to the direction of gravity. If you are working on a space station in artificial gravity, ask your lab mate for the direction of "down".

6. Sonicate the NPM solution with the wafer inside. After the beautiful metal membrane is turned into gazillion pieces, transfer the wafer to running IPA from a squirt bottle. Blow dry on a piece of cleanroom cloth with one corner of the wafer touching. This

single-point contact makes it easy for the IPA to quickly train by surface tension. Never dry by evaporation.

5.4.4 Third Layer E-beam and Etching

1. With a clean wafer froms step5.4.3, first deposite 80 nm of SiO_2. Use the same process as in step5.4.1

2. Spin ARP 6200.13 at 2000 rpm. Bake for 60 sec on a hot plate at 150 .

3. Before writing, align to the chip-alignment marks. Then write. Pattern exposes between the center pin and the ground planes.

4. After writing, develop at 6 for 60 - 90 s. The development time is not sensitive, but make sure that the sample is well developed. If there is left-over resist in the exposed area, increase exposure. That is typically due to dramatic changes in the resist thickness due to the irregular surface profile of the sample after previous etching steps.

5. Even thick resists with high-aspect ration should not experience structural movements. Structural movement is usually indicative of weak attachment of the resist copared with the built-in stress. Solution is either go with thinner resist, surface treatment, or go with a different polymer.

6. Now to pattern the SiO_2 hard-mask, use the Fluorine etcher for 3-4 minutes. One can use the same carrier wafer for the next step.

7. Now to pattern the silicon substrate underneath, *make sure you use a silicon wafer instead of those SiO_2 ones because otherwise micro-masking would occur.* make the penetration step only 5 seconds long to reduce excessive side-etch. Use the clorine etcher for this.

8. To strip the sample clean, first dip it in hot NMP and sonicate for 10 minutes. Power, frequency and temperature is not terribly important. Clean with IPA and make sure the sample is dry. Use surface tension of the solvents to dry the surface. Do not use evaporation since it leaves residue.

9. To strip the SiO_2 from the sample, dip the sample in buffered HF quickly, make sure the entire wafer surface enter the etchant in one quick motion. Failure to do so leaves edge-marks that occurs at the interface between air, the sample and the etchant. Those marks can not be cleaned afterward.

10. wait until all of the remaining organic membrane lift-off the surface of the wafer, then take out the sample from the HF and quickly transfer to running water. This way the non-soluable gunk can not attach to the sample.

5.4.5 Dicing, Mounting, and Wire-bonding

refer to earlier pictures, and have fun. Samples can not be salvaged if anything contaiminates the surface. So be careful, but don't feel bad about mistakes.

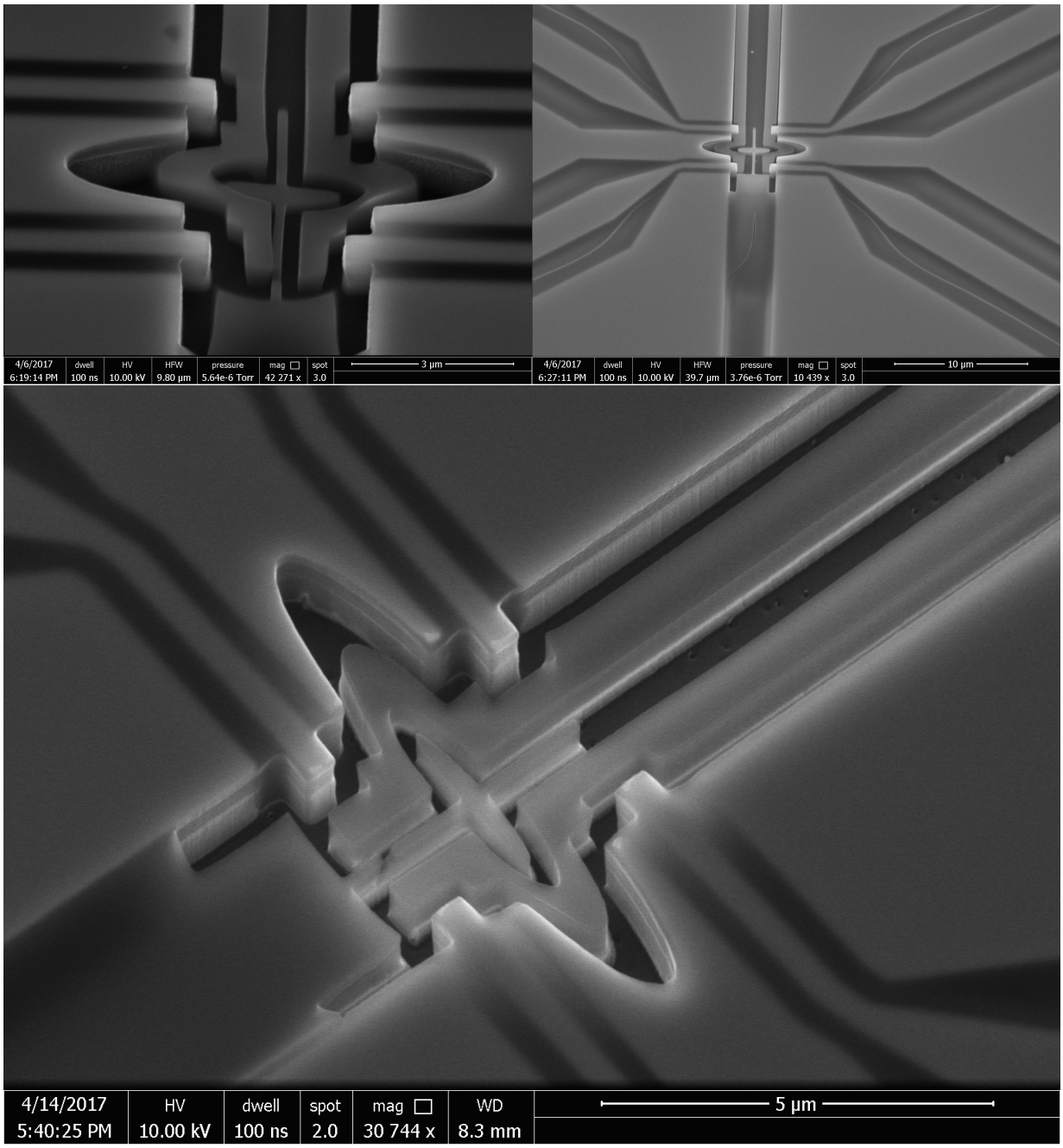

Figure 5.6: left figure showing details of the resist profile for the third etch layer *before* the RIE etch. **Note** that the warping of the resist is due to the charge from the e-beam of the SEM during imaging. A zoomed out version of the same sample shows the resist in-tact in a smaller zoom. Figure c shows the resist profile from a test sample (ruined toss-away wafers). It shows 1. tear of resist covering the center pin and 2. the uneven thickness of the resit. The exposed areas show perfect clearance. Also notice the much thinner resist on the L1 metal surface. This is due to the surface tension of the resist inside the channel pulling. To compensate for this thinning, we use a slightly thicker resist for the L3 process. Without this practice, metal on the L1 layer will be consumed during the L3 RIE.

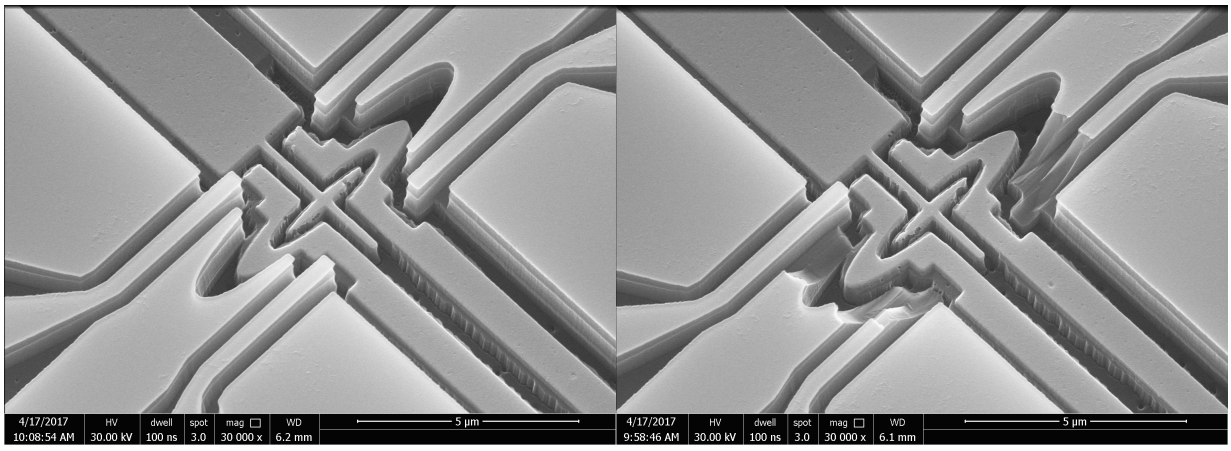

Figure 5.7: Chipped L1 Pattern Due to Sonication Damage Left: intact L1 pattern. Right: chipped pattern after sonication (same wafer, different die).

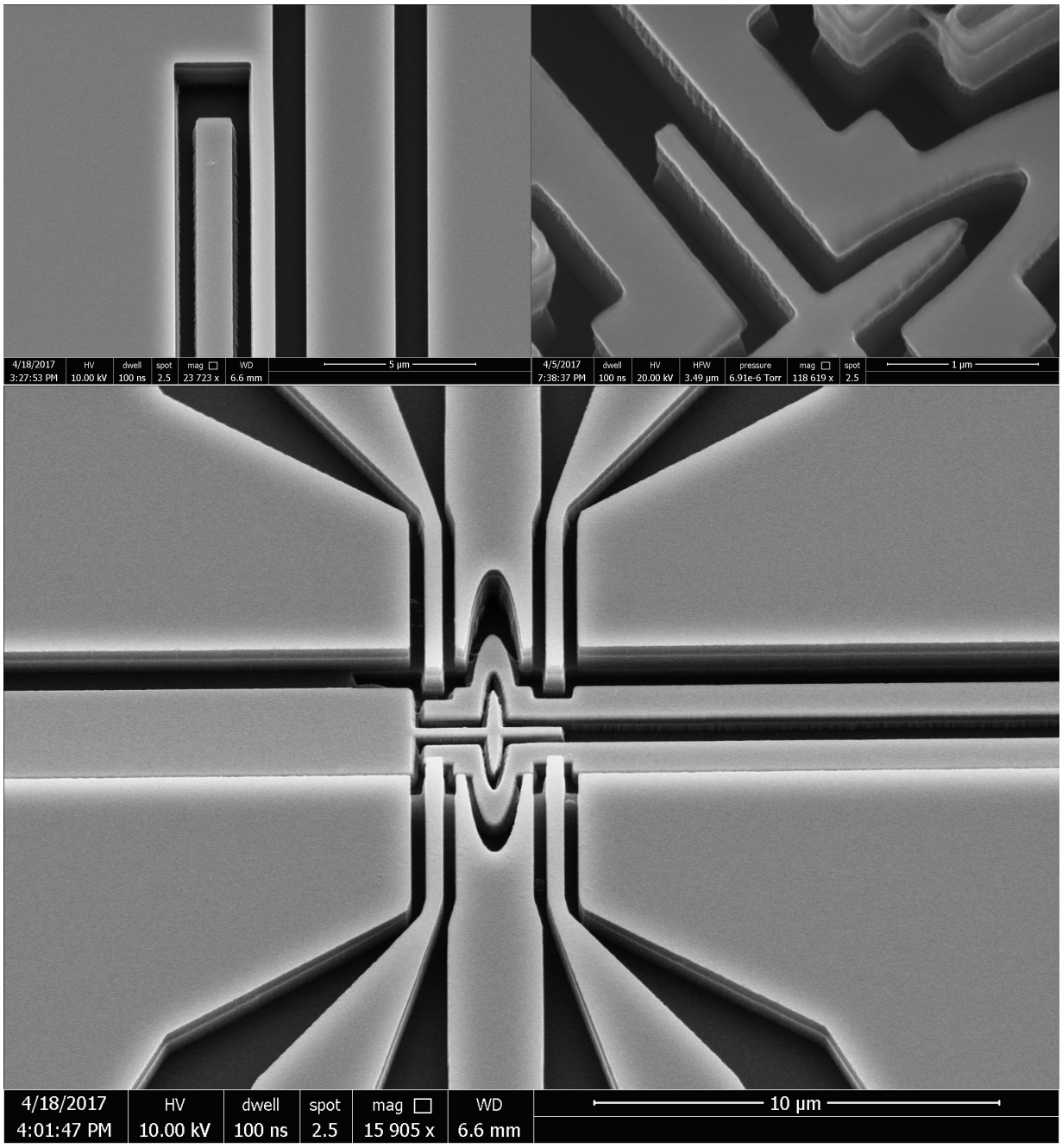

Figure 5.8: Upper-left: Zoomed out version of the trap area. Upper-right: details of the coupler with L3 etch. Bottom: details of the L3 etch in-between the resonator and trap electrode.

REFERENCES

[1] HOOMD.

[2] J. a. Anderson, C. D. Lorenz, and A. Travesset. General purpose molecular dynamics simulations fully implemented on graphics processing units. *Journal of Computational Physics*, 227(10):5342–5359, May 2008.

[3] Andrei. *Two-Dimensional Electron Systems*, volume 19. 1997.

[4] a. D. Armour, M. P. Blencowe, E. Brahimi, and a. J. Rimberg. Universal Quantum Fluctuations of a Cavity Mode Driven by a Josephson Junction. *Phys. Rev. Lett.*, 111(24):247001, Dec. 2013.

[5] A. Blais, R.-S. Huang, A. Wallraff, S. M. Girvin, and R. J. Schoelkopf. Cavity quantum electrodynamics for superconducting electrical circuits: An architecture for quantum computation. *Phys. Rev. A*, 69:062320, Jun 2004.

[6] F. R. Bradbury, M. Takita, T. M. Gurrieri, K. J. Wilkel, K. Eng, M. S. Carroll, and S. a. Lyon. Efficient Clocked Electron Transfer on Superfluid Helium. *Phys. Rev. Lett.*, 107(26):266803, Dec. 2011.

[7] A. D. Chepelianskii, M. Watanabe, K. Nasyedkin, K. Kono, and D. Konstantinov. An incompressible state of a photo-excited electron gas. *Nat. Comm.*, 6(May):7210, 2015.

[8] M. H. Devoret and R. J. Schoelkopf. Superconducting circuits for quantum information: An outlook. *Science*, 339(6124):1169–1174, 2013.

[9] M. I. Dykman, P. M. Platzman, and P. Seddighrad. Qubits with electrons on liquid helium. *Physical Review B*, 67(15):155402, Apr. 2003.

[10] V. S. Edel'man. Levitated electrons. *Soviet Physics Uspekhi*, 23(4):227–244, Apr. 1980.

[11] A. A. Fragner. *Circuit Quantum Electrodynamics with Electrons on Helium*. Yale University, 2013.

[12] T. Frey, P. J. Leek, M. Beck, A. Blais, T. Ihn, K. Ensslin, and A. Wallraff. Dipole coupling of a double quantum dot to a microwave resonator. *Phys. Rev. Lett.*, 108:046807, Jan 2012.

[13] L. Gor'kov and D. Chernikova. Concerning the structure of a charged surface of liquid helium. *Soviet Journal of Experimental ...*, 1973.

[14] C. C. Grimes and G. Adams. Evidence for a Liquid-to-Crystal Phase Transition in a Classical, Two-Dimensional Sheet of Electrons. *Phys. Rev. Lett.*, 42(12):795–798, Mar. 1979.

[15] H. Ikegami, Y. Tsutsumi, and K. Kono. Chiral Symmetry Breaking in Superfluid 3He-A. *Science*, 341(6141):59–62, July 2013.

[16] K. Kono. Electrons on the Surface of Superfluid 3He. *Journal of Low Temperature Physics*, 158(1-2):288–300, Jan. 2010.

[17] G. Koolstra, G. Yang, and D. I. Schuster. Spectroscopy of wigner molecules on superfluid helium using a superconducting resonator. *arXiv preprint arXiv:1902.04190*, 2019.

[18] Y. Kubo, F. R. Ong, P. Bertet, D. Vion, V. Jacques, D. Zheng, A. Dréau, J.-F. Roch, A. Auffeves, F. Jelezko, J. Wrachtrup, M. F. Barthe, P. Bergonzo, and D. Esteve. Strong coupling of a spin ensemble to a superconducting resonator. *Phys. Rev. Lett.*, 105:140502, Sep 2010.

[19] S. A. Lyon. Spin-based quantum computing using electrons on liquid helium. *Physical Review A*, 74(5):1–6, Nov. 2006.

[20] H. Malissa, D. I. Schuster, A. M. Tyryshkin, A. A. Houck, and S. A. Lyon. Superconducting coplanar waveguide resonators for low temperature pulsed electron spin resonance spectroscopy. *Rev. Sci. Instrum.*, 84(2):–, 2013.

[21] D. Marty. Stability of two-dimensional electrons on a fractionated helium surface. *Journal of Physics C: Solid State Physics*, 19(30):6097–6104, Oct. 1986.

[22] Y. Monarkha and K. Kono. *Two-Dimensional Coulomb Liquids and Solids*. Springer, Berlin, 2004.

[23] G. Papageorgiou, P. Glasson, K. Harrabi, V. Antonov, E. Collin, P. Fozooni, P. G. Frayne, M. J. Lea, D. G. Rees, and Y. Mukharsky. Counting individual trapped electrons on liquid helium. *Applied Physics Letters*, 86(15):1–3, 2005.

[24] K. D. Petersson, L. W. McFaul, M. D. Schroer, M. Jung, J. M. Taylor, A. A. Houck, and J. R. Petta. Circuit quantum electrodynamics with a spin qubit. *Nature*, 490(7420):380–383, 2012.

[25] J. R. Petta, A. C. Johnson, J. M. Taylor, Laird, E. A., A. Yacoby, M. D. Lukin, C. M. Marcus, M. P. Hanson, and A. C. Gossard. Coherent Manipulation of Coupled Electron Spins in Semiconductor Quantum Dots. *Science*, 309(5744):2180–2184, Sept. 2005.

[26] P. M. Platzman and M. I. Dykman. Quantum Computing with Electrons Floating on Liquid Helium. *Science*, 284(5422):1967–1969, June 1999.

[27] S. Probst, H. Rotzinger, S. Wünsch, P. Jung, M. Jerger, M. Siegel, A. V. Ustinov, and P. A. Bushev. Anisotropic rare-earth spin ensemble strongly coupled to a superconducting resonator. *Phys. Rev. Lett.*, 110:157001, Apr 2013.

[28] M. J. Reagor. *Superconducting Cavities forCircuit Quantum Electrodynamics*. Yale University, 2016.

[29] D. Rees, I. Kuroda, C. Marrache-Kikuchi, M. Höfer, P. Leiderer, and K. Kono. Point-Contact Transport Properties of Strongly Correlated Electrons on Liquid Helium. *Phys. Rev. Lett.*, 106(2):1–4, Jan. 2011.

[30] E. Rousseau, D. Ponarin, L. Hristakos, O. Avenel, E. Varoquaux, and Y. Mukharsky. Addition spectra of Wigner islands of electrons on superfluid helium. *Physical Review B*, 79(4):045406, Jan. 2009.

[31] R. J. Schoelkopf and S. M. Girvin. Wiring up quantum systems. *Nature*, 451(7179):664–669, Feb. 2008.

[32] D. I. Schuster, A. Fragner, M. I. Dykman, S. A. Lyon, and R. J. Schoelkopf. Proposal for Manipulating and Detecting Spin and Orbital States of Trapped Electrons on Helium Using Cavity Quantum Electrodynamics. *Phys. Rev. Lett.*, 105(4):1–4, July 2010.

[33] D. I. Schuster, a. P. Sears, E. Ginossar, L. DiCarlo, L. Frunzio, J. J. L. Morton, H. Wu, G. A. D. Briggs, B. B. Buckley, D. D. Awschalom, and R. J. Schoelkopf. High-Cooperativity Coupling of Electron-Spin Ensembles to Superconducting Cavities. *Phys. Rev. Lett.*, 105(14):140501—-, Sept. 2010.

[34] K. Shirahama, S. Ito, H. Suto, and K. Kono. Surface study of liquid3He using surface state electrons. *Journal of Low Temperature Physics*, 101(3-4):439–444, Nov. 1995.

[35] K. Shirahama and K. Kono. Dynamical Transition in the Wigner Solid on a Liquid Helium Surface. *Phys. Rev. Lett.*, 74(5):781–784, Jan. 1995.

[36] W. Sommer and D. Tanner. Mobility of Electrons on the Surface of Liquid ˆ{4}He. *Phys. Rev. Lett.*, 27(20):1345–1349, Nov. 1971.

[37] M. Takita and S. a. Lyon. Isolating electrons on superfluid helium. *Journal of Physics: Conference Series*, 568(5):052034, Dec. 2014.

[38] J. J. Viennot, M. C. Dartiailh, A. Cottet, and T. Kontos. Coherent coupling of a single spin to microwave cavity photons. *Science*, 349(6246):408–411, 2015.

[39] A. Wallraff, D. I. Schuster, A. Blais, L. Frunzio, R. S. Huang, J. Majer, S. Kumar, S. M. Girvin, and R. J. Schoelkopf. Strong coupling of a single photon to a superconducting qubit using circuit quantum electrodynamics. *Nature*, 431(7005):162–167, 2004.

[40] R. Williams, R. Crandall, and A. Willis. Surface states of electrons on liquid helium. *Phys. Rev. Lett.*, 1971.

[41] G. Yang, A. Fragner, G. Koolstra, L. Ocola, D. Czaplewski, R. Schoelkopf, and D. Schuster. Coupling an ensemble of electrons on superfluid helium to a superconducting circuit. *Physical Review X*, 6(1):011031, 2016.